Semiconductor Nanowire Based Piezoelectric Energy Harvesters: Modeling, Fabrication, and Characterization

by

Guocheng Liu

A thesis
presented to the University of Waterloo
in fulfillment of the
thesis requirement for the degree of
Doctoral of Philosophy
in
Electrical and Computer Engineering

Waterloo, Ontario, Canada, 2015

AUTHOR'S DECLARATION

I hereby declare that I am the sole author of this thesis. This is a true copy of the thesis, including any required final revisions, as accepted by my examiners.

Guocheng Liu

I understand that my thesis may be made electronically available to the public.

Guocheng Liu

Abstract

Semiconductor nanowire (NW) arrays' unique advantages over bulk forms, including enhanced surface area, high mechanical flexibility, high sensitivity to small forces, better charge collection, and enhanced light absorption through trapping, make them ideal templates on which to build other structures. This research on the piezoelectric behavior of NWs used in high-performance energy harvesters is based on device modeling, fabrication, and characterization. These activities optimize the electrical properties of a NW device in response to a compression/release force applied to the NWs.

The dissertation first discusses the piezoelectric and semiconductor properties of wurtzite compound nanomaterials, emphasizing III-nitride semiconducting InN and GaN NWs. Static analysis identifies the role of carrier density, temperature, force, length/diameter ratio, and Schottky barrier height. Piezoelectric nanogenerators (NGs) based on vertically aligned InN nanowires (NWs) are fabricated, characterized, and evaluated. In these NGs, arrays of exclusively either *p*-type or intrinsic InN NWs prepared by plasma-assisted molecular beam epitaxy (MBE) demonstrate similar average piezoelectric properties. The *p*-type NGs show 160% more output current and 70% more output power product than the intrinsic NGs. The features driving performance enhancement are reduced electrostatic losses due to a higher NW areal density and longer NWs, and improved electromechanical energy conversion efficiency due to smaller NW diameters. These findings highlight the potential of InN based NGs as a power source for self-powered systems and the importance of NW morphology in overall NG performance.

The second part is devoted to demonstrate a series of flexible transparent ZnO *p*-*n* homojunction nanowire (NW)-based piezoelectric nanogenerators (NGs) with different *p*-doping concentrations. The lithium-doped segments are grown directly and consecutively on top of intrinsic nanowires (*n*-type). When characterized under cyclic compressive strains, the overall NG performance is enhanced by up to eleven-fold if the doping concentration is properly controlled. This improvement is attributable to reduction in the mobile charge screening effect and optimization of the NGs' internal electrical characteristics. Experimental results also show that an interfacial MoO_3 barrier layer, at an optimized thickness of 5-10 nm, reduces leakage current and substantially improves piezoelectric NG performance.

The third part presents the first cascade-type compact hybrid energy cell (CHEC) that is capable of simultaneously or individually harvesting solar and strain energies. It is made of an *n*-*p* junction NW-based piezoelectric nanogenerator to harvest strain energy and an nc/a-Si:H single junction cell to

harvest solar energy. The CHECs ability to harvest energy effectively simultaneously, and complementary is demonstrated by deploying six CHECs to power LEDs and a wireless strain gauge sensor node. Under ~10 mW/cm^2 illumination and vibrations of 3 m/s^2 at 3 Hz frequency, the output current and voltage from a single 1.0 cm^2 CHEC are 280 μA and 3.0 V, respectively; enough to drive many low power commercial electronics.

This dissertation aims to deepen understanding of the piezoelectric behavior of semiconductor NWs on hard and flexible substrates. Thus, this research in the field of nanopiezoelectrics could have a substantial impact on many areas, ranging from the fundamental study of new nanomaterial properties and mechanical effects in nanostructures to diverse applications like aerospace.

Acknowledgements

I would like to express my deepest love, respect, and admiration to my entire family for their unconditional support, understanding, and dedication throughout these years.

I would like to acknowledge my supervisor Professor Dayan Ban for his invaluable support. During the Ph.D period, I experienced numerous difficulties. I felt frustrated, and depressed. Without Professor Ban's help, I would not have been able to come to this moment. I would also like to thank all my committee members for their time, interest and suggestions: Professor Siva Sivoththaman, Professor Bo Cui, Professor John Yeow and Professor Andy (Xueliang) Sun (the University of Western Ontario). I want to thank the National Research Council Canada, Defence Research and Development of Canada, the University of Waterloo, Waterloo Institute of Nanotechnology and Ontario Graduate Scholarship of Canada for their financial support.

There are lots of collaborators who have contributed to my dissertation. I would like to express my appreciation to Dr. George Xiao and Dr. Nezih Mrad for discussion and collaboration at the National Research Council Canada, Defence Research and Development of Canada. I would like to thank Professor Zetian Mi and Dr. Songrui Zhao at McGill University. I would like to thank Professor Chuan-Pu Liu and Dr. Nai-Jen Ku at National Cheng Kung University. I would like to thank Professor Jun Yang and Dr. Qiuquan Guo at the University of Western Ontario. I also would like to express appreciation to Professor Eihab Abdel-Rahman, Professor Zoya Leonenko, Professor Zbig Wasilewski, Dr. Karim EI-Rayes, Dr. Robert Henderson, and Dr. Man Chun Tam for collaboration.

Furthermore, I am thankful to the Giga to Nano (G2N) lab manager, Richard Barber, not only for his invaluable technical assistance but also for creating a friendly and welcoming environment. I am also grateful to all my colleagues. Special thanks are due to Dr. Bin Sun, Dr. Bright Iheanacho, Dr. Alireza Khosropour, and Dr. Minoli Pathirane for their valuable discussions.

Also, I would like to thank Ms. Janet Mary McPherson at the University of Waterloo Writing Centre. She has been always there to lend me a helping hand.

Last but not least, I would like to thank all of my present and former colleagues in Professor Dayan Ban's group. In particular, I would like to send well deserved thanks to Dr. Jun Chen, Dr. Ghasem Razavi, Mr. Mark Ferguson and Mr. Zhenzhong Li. They have been always friendly and helpful.

Table of Contents

List of Figures

List of Tables

List of Abbreviations

AZO	aluminum-doped ZnO
C-AFM	conductive atomic force microscopy
ED	electrochemical deposition
FEM	finite element method
FE-SEM	field-emission scanning electron microscope
FWHM	full width at half-maximum
HIM	helium ion microscope
HMTA	hexamethylenetetramine
J-V	current density-voltage
KPFM	Kelvin probe force microscopy
MBE	molecular beam epitaxy
MEMS/NEMS	micro/nano-electromechanical system
M_oO_3	molybdenum oxide
NBE	near-band edge
NG	nanogenerator
NIR	near-infrared range
NW	nanowire
PDMS	polydimethylsiloxane
PEI	polyethylenemine
PEN	polyethylene naphthalate
PL	photoluminescence
PMMA	polymethyl methacrylate
RMS	root-mean-square
SHM	structural health monitoring
SIMS	second-ion mass spectroscopy
SiN	silicon nitride
SPR	surface plasmon resonances
TED	thermionic-emission-diffusion
WSNs	wireless sensor networks
XRD	X-ray diffraction

Chapter 1
Problem Overview and Energy Harvesting

1.1 Research Motivation: Alternative-Energy-Powered Wireless Sensors

Aircraft structural health monitoring (SHM) is the assessment of an aircraft's structural condition using advanced sensor technologies. Data is periodically collected from sensors and used to assess the structural integrity of air vehicles [1]. SHM benefits include (i) enhancement of crew safety by providing the real time health status of aircraft structures and alerts about necessary actions; (ii) reduction of life-cycle cost by avoiding unnecessary maintenance, improving maintenance using the automatic SHM system, thus extending the life of the structures; and (iii) promotion of novel structural design by optimizing structural efficiency.

Aircraft SHM has two critical aspects: load monitoring and damage assessment. Load monitoring is performed by the combination of two methods, namely, using a limited number of strain sensors mounted at critical points for direct measurement, and monitoring flying parameters for the estimation of loads in other locations. Those flying parameters include flight time, flight cycle, number of landings, temperature, air pressure/density, air speed, acceleration, rotational rate, vibration, and natural frequency. Damage assessment covers the detection/evaluation/monitoring of damage induced by accidents such as those arising from bird strikes, foreign objects, and maintenance, and damage caused by the environment, such as corrosion of metallic structures, delamination of composite structures, and degradation of nonmetallic structures due to thermal and fluid exposure.

SHM systems can be grouped into two categories – wired and wireless – based on whether or not wire is used. Both systems have advantages and disadvantages. The wired systems offer advantages such as (i) design freedom and versatile SHM capabilities; and (ii) the possibility of immunity to electromagnetic interference. Some wired sensors, including electrical strain gauges, accelerometers, fiber optic sensors, piezoelectric sensors, thermocouples, comparative vacuum monitoring (CVM), microwave sensors, and carbon nanotubes have been demonstrated as potentially useful for aircraft SHM. Nevertheless, the wires tend to cause problems for manufacturers and maintenance crews. The addition of wiring weight increases aircraft fuel consumption, and the installation of complex harnesses within the fuselage can be an error-prone process requiring a significant number of workers, thus increasing cost. Additionally, some spots are not accessible by wires, making maintenance difficult because reaching the wiring harness often requires dismantling of an aircraft's external structures.

Alternatively, wireless sensor systems can effectively eliminate these wiring problems, but their performance is generally inferior to that of wired sensor systems and prone to electromagnetic interference, although tremendous progress has been made in recent years. References [2, 3] present some applications of wireless sensor systems used in the SHM of civil structures and aircraft structures. A classic wireless SHM system is illustrated in **Figure 1.1**. The sensor module mainly consists of three or four subsystems: sensing, data processing, communicating, and power supply (if applicable). The major challenges for the application of wireless sensors to aircraft SHM are in the sensor's capabilities, the power supply, and the suitability of SHM, plus its long-term reliability. If the only way to supply power is by means of a cable, then the rationale for wireless protocols is eliminated because the power cable can also be used for communication. Nevertheless, if a wireless sensor approach is being adopted, the power supply will be a key factor for success in the wireless sensor network.

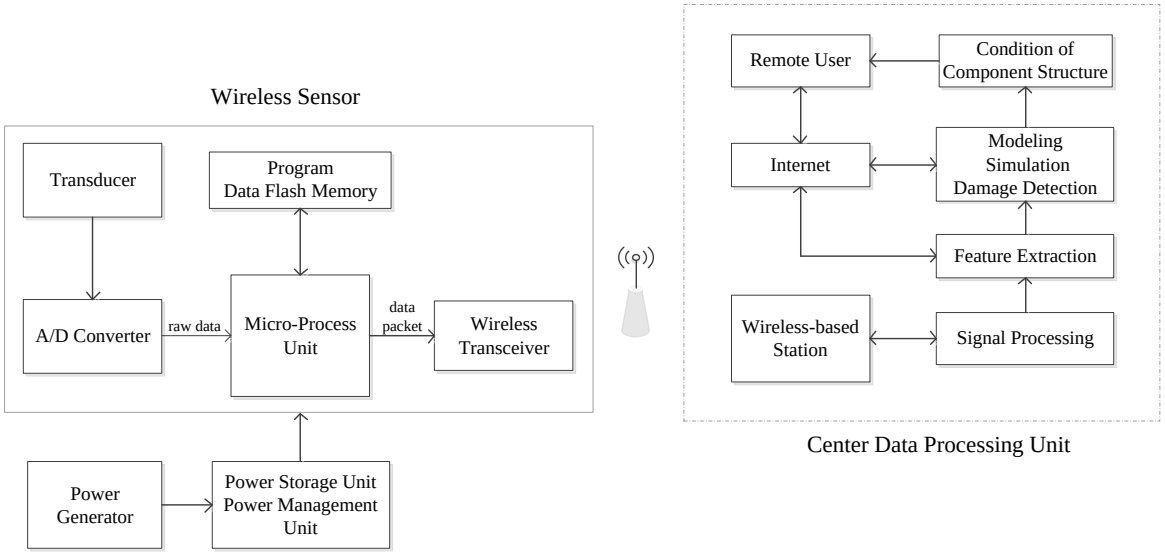

FIGURE 1.1 Block diagram of a typical wireless SHM system

A power supply is generally attached by wireless sensors to fulfill the tasks such as sensing, signal conditioning and processing, data storage, and communication. Using a battery is currently the only viable option, but using one for aircraft SHM applications is impractical in most circumstances due to its limited life span. In recent years, energy harvesting technology has emerged as an attractive option. The energy harvested is either from ambient sources (solar, vibration, thermal) or from a remote source of power (a radio-frequency or acoustic beacon).

1.2 Literature Review of Semiconductor Nanowires for Energy Harvesting

In an aircraft operation environment, sources such as solar, wind, vibration, temperature differentials, electromagnetic, and acoustic can potentially be used to supply energy for sensor applications. Three common energy-scavenging devices are piezoelectric vibration harvesters, thermoelectric power generators, and photovoltaic (PV) cells. Piezoelectric harvesters can be attached to a vibrating mechanical source, such as an airframe or wing, and thermoelectric generators can be attached to a heat-generating source such as an engine.

1.2.1 Piezoelectric Nanogenerators

Of the three different vibration-to-electrical conversion approaches (piezoelectric, electrostatic, and electromagnetic), the piezoelectric method has received most attention, due to its main advantages, such as large power density, easy application of piezoelectric devices in both macro and micro scale based on well-developed production techniques, the direct output voltage, and no need for an external voltage input [4]. When an external force is applied, variations during the dipolar moment induces the energy conversion in piezoelectric materials, forming a potential difference to power devices. In an aircraft environment, piezoelectric vibration harvesters are favored for their high electro-mechanical coupling coefficient, miniaturized dimensions, and their potential deposition on substrates for micro/nano-electromechanical system (MEMS/NEMS) applications. MEMS/NEMS integrates mechanical elements, sensors, actuators, and electronics with a common silicon-based substrate through microfabrication processes. MEMS/NEMS characteristics include miniaturization, low cost, relative low power consumption, and multifunction integration. Currently, most available piezoelectric vibration harvesters intended for use in air vehicles are too large for the applications considered in this research, so interest has grown in miniaturizing them. Miniaturization has multiple advantages; for example, reduced size and weight are critical for the use of SHM systems in lightweight structures such as aerospace structural systems (e.g., aircraft and rockets). Smaller energy harvesters are easier to install, particularly if embedded within structural elements. In addition, MEMS/NEMS-based energy harvesters are more power efficient than their macroscale counterparts.

For a piezoelectric material, the linear constitutive law of the relation between the stress and strain components, σ and ε, and the electric field and electrical displacement component, E and D, is given as:

$$\sigma_i = \sum_j c_{ij}\varepsilon_j - \sum_j e_{ji}E_j \qquad D_i = \sum_j e_{ij}\varepsilon_j + \sum_j \kappa_0\kappa_{ij}E_j \tag{1.1}$$

where c_{ij}, e_{ij}, and κ_{ij} are the mechanical stiffness tensor, piezoelectric coefficient, and relative dielectric constant, respectively, and e_{ij} is the transpose of e_{ji}.

A typical piezoelectric-based energy harvesting configuration consists of three components: a piezoelectric energy converter, an energy harvesting circuit, and an energy storage device. The energy harvesting circuit converts the energy produced by the piezoelectric converter from AC to DC and/or from low voltage to high voltage. Energy harvested from vibrations varies according to the frequency and amplitude of the vibrations, whose source must be characterized to optimize the piezoelectric converter. An analytical model of the energy source is essential, not only for estimating the amount of power available for harvesting, but also for indicating explicit relationships that may enable system designers to maximize the harvested power. Various mathematical models are used for performance optimizations, including an electro-mechanical coupled model that considers specific design parameters critical to the development of an actual piezoelectric converter. These parameters include the electromechanical coupling coefficient, mechanical quality factor, resonant frequency, and transmission coefficient.

High piezoelectric harvester efficiency and reliability depends on meeting three challenges: wide bandwidth operation, self-tuning capability under various conditions, and multimodal energy harvesting capability. In a real aircraft environment, a vibration energy harvesting technique can be considered for several structures. For example, a typical aircraft wing panel has vibration amplitudes to a maximum of $\pm$0.2 mm and a frequency of 300 Hz; an aircraft engine has a maximum vibration mode of 1.0 m/s^2 during take-off (50 Hz, 10 m from the engine), and this number drops to 0.1 m/s^2 in cruise mode. Using wireless sensors in aircraft involves several inherent constraints, such as less than 0.5 m/s^2 vibration amplitudes, geometric limitations (e.g., thicknesses less than 5 mm) due to aircraft aerodynamics, and extreme operation conditions (e.g., typical aircraft engine temperatures can vary from 373 K to 2273 K). Although piezoelectric vibration harvester development is currently at the initial stage, research has demonstrated its great potential in aircraft SHM, such as the SHM of main gear boxes, panels, blades, engines, and empennages. In addition, multivariable design optimization for various performance metrics, including power output (μW), operating and static power densities (μW/cm^3), specific power (W/kg), voltage (V) and efficiency (P_{out}/P_{in}), could assist the realization of an embeddable SHM sensor.

Materials [5] showing piezoelectricity are widely available, including single crystals (e.g., quartz SiO_2, cane sugar, and Rochelle salt), piezoceramic materials (e.g., Lead Zirconate Titanate (PZT), $PbTiO_3$, $BaTiO_3$ composites), thin films (e.g., sputtered zinc oxide), screen printable thick-films based upon

piezoceramic powers, and polymers (e.g., polyvinylidenefluoride (PVDF)). Insulator piezoelectric materials have long been used in piezoelectric energy-harvester and sensor devices. However, the large unit size, large triggering force, and specific high resonance frequency of the traditional cantilever-based energy harvester limit their applicability and adaptability in nanoscale devices and systems. Using nano-to-micro-sized (normally single) crystals of piezoelectric material deposited or grown across a substrate material [6-8] permits device designs that are alternatives to the ceramic or polymer piezoelectric ones. Materails with wurtzite structures that have non-central symmetry, such as ZnO, GaN, and InN have the ability to develop piezoelectric potential (piezopotential) once they are strained. These devices are being explored as a means to access the advantages of flexible piezoelectrics such as PVDF or ceramic-polymer composites with the high coupling of single-crystal piezoelectrics. Typically, semiconductor nanowires have nanoscale cross sectional dimensions, with lengths spanning from hundreds of nanometers to millimeters. Mostly, the nanostructured material is ZnO nanorods or nanowires, but PZT [9], $BaTiO_3$ [10], and $ZnSnO_3$ [11] nanostructures have also been chosen. When hard substrates are vibrated or compressed, or flexible substrates are bent, the piezoelectric elements are strained, generating external voltage. Devices using flexible substrates can be bent to harvest energy from a wide range of sources, even low-frequency but high-displacement movements such as daily human motion [12]. The first and most widely studied device designs encapsulated the nanowires in an insulator (typically PMMA) with a deposited top electrode. This design leads to a large potential difference but a relatively low current output because of the insulating layer [7]. The second, more recently reported structures, used a p-n junction between the as grown n-type ZnO and a variety of p-type materials [13, 14]. However, these structures are less well-studied than the insulator-type devices and need significant performance improvement.

TABLE 1.1 Piezoelectric NGs Properties of Some Typical Nanowires

Nanowires attributes	NG type and dimensions (cm^2)	Force/stress/ strain	Frequency (Hz)	V_{oc} (mV)	I_{sc} (nA)	Power Density (uW/cm^2)	Description
CuO/ZnO by solution growth	n/a	0.012%	0.4, 0.8	738	n/a	n/a	Core-shell p-n junction [15]
CdS	n/a	34N	0.45	440	n/a	n/a	H_2S gas sensor [16]
ZnO	n/a	8.87 uN/cm^2	23.7 k	103	1117	0.115	Contact influence [17]
ZnO/CuSCN	$AC\ Type$ 2.0×1.0	50 g	40-110M	1.07 V	1.88 mA/cm^2	434	p-n junction [18]
ZnO	$AC\ Type$ 0.5×0.5	0.9kPa	1-15	n/a	10.98	n/a	Vibration sensor [19]
ZnO	$AC\ Type$ 0.3×0.3	Eye movement	0.4, 1.6	2	5	n/a	16 um thickness [11]
PZT by HT process	$AC\ Type$ 15×0.8	n/a	n/a	6V	45	200	UV sensor [20]
ZnO	n/a	n/a	n/a	19	0.3 pA/cm^2	n/a	Hybrid device [21]
ZnO, P3HT:PCBM	n/a	n/a	n/a	150	Hundreds	n/a	Hybrid device [22]
PMN-PT	1.0×0.5	0.2%	5	7.8V	2.29 uA	35.7	Mixed with PDMS [23]
ZnO	1.0	0.1% Rate of 5% S^{-1}	0.33	2.03 V	107	~11mW/cm^2	Lateral, NW density 1.1×10^6 cm^{-2} [24]
ZnO	n/a	n/a	n/a	284	10.6	n/a	p-n homojunction [25]

1.2.2 Thermoelectric Cells

The development of thermoelectric cells (TECs) for aircraft SHM applications is in its initial phase, with only a few examples in the literature, all based on laboratory work. The temperature of the air at the boundary of an aircraft's surface is different from the ambient air due to the air dynamics. Depending on the air flow route, average temperatures range from 241 K to 320 K; the temperature difference can reach a maximum of 30 K between the fuel at the base of the tank and the air; the temperature of a fuselage can vary between 253 K and 295 K. Therefore, a real aircraft environment is suitable for TEC devices.

Integration of TECs into a power system has not been adequately addressed for ambient temperature systems because of the challenges: (i) fluctuations in the ambient temperature leading to the unstable output voltage of TECs; (ii) the load needing to handle such fluctuations or be supplied with a regulated voltage output; and (iii) low ambient temperature differences not capable of producing sufficient electric energy to recharge a battery or power a device [26].

A TEC converts temperature differences into electric energy mainly through the Seebeck effect, which exploits a temperature difference between two ends of the device that drives the diffusion of charge carriers. A figure of merit for the energy conversion performance of a thermoelectric material is determined by the dimensionless coefficient, $ZT = S^2\sigma T/k$, where S, σ, T, k are the Seebeck coefficient, electrical conductivity, absolute temperature, and thermal conductivity, respectively. ZT values should be at least in the 3~4 range if thermoelectrics is to compete with other electricity producing methods; larger ZT values represent higher efficiency [27]. The quantity of $S^2\sigma$ is defined as the power factor (PF). The larger its value, the greater the output voltage and current. Such a material has greater potential when it does not require a temperature much above environmental temperature. Relative to reducing the thermal conductivity of bulk thermoelectric material, research to date has focused on utilizing nanostructured material such as nanowires, superlattices, and composite matrices [28]. According to the definition of the ZT coefficient, thermoelectric performance should be improved with the electrical properties that are not negatively affected. Phonon scattering may be increased by a nanoscale structure with at least one dimension of the order of the phonon mean free path, because phonon transport is expected to be greatly impeded in thin 1D nanostructures, leading to increased boundary scattering and reduced phonon group velocities due to phonon confinement. Thermal conductivity is thus largely reduced. TEC performance could be significantly improved by reducing dimensions to the nanoscale [29-31].

Some studies have focused on using NWs for TECs. For example, compared to a ZT of 0.01 for bulk Si, Si NWs have the same Seebeck coefficient and electrical resistivity values as doped bulk Si, while

nanowires with diameters of ~50 nm shows 100-fold reduction in thermal conductivity, and yield a *ZT* of 0.6 at room temperature [32-34]. For such NWs, the lattice contribution to thermal conductivity approaches the amorphous limit for Si. Although bulk Si may not be a good thermoelectric material, nanostructuring it may be a cheaper and simper strategy for fabricating thermoelectric devices. The *ZT* figure of merit could be improved further with the use of core-shell-type structures. In theory, when Si NWs are coated with 1~2 unit cell thick Ge, the NW conductivity will significantly decrease, by 75%, due to the depression and localization of long-wavelength phonon modes at the Si/Ge interface [27, 35, 36].

The ZT thermoelectric figure of merit and maximum properties of III-V semiconductor NWs such as InSb, InAs, GaAs, and InP have been theoretically calculated by Mingo, from whose results, InSb NWs are considered the most promising thermoelectric material of the four compounds [37]. To date, the VLS method has been used to grow InSb NWs, the thermoelectric properties of which have been characterized [38-41]. According to Zhou *et al.*'s findings about the effect of growth base pressure on the thermoelectric properties of InSb NWs, *ZT* values were about ten times lower than the reported bulk values due to a reduced Seebeck coefficient and mobility, and high *ZT* can be achieved by carefully controlling impurity doping and the surface of NWs [38, 41]. Based on theoretical calculations for InN NWs, *ZT* could reach around 1.6 at 1000 K and 0.256 at room temperature, which indicates that the InN NWs could potentially be used in thermoelectric devices [42]. In the investigation of the thermoelectric ZnO NWs, it has been theoretically calculated that *ZT* increases 30 times more than the bulk when ZnO NWs diameter is decreased to 8 Å [43]. According to the results of two terminal *I-V* measurements on individual ZnO NWs suspended in a vacuum, the thermal conductivity was much smaller than that of the bulk, and *ZT* reached 0.11 at around 1000 K [44]. Doped ZnO ceramics, using elements (Al, Ga, Mn) as dopants, appears a promising candidate for improving electrical conductivity and reducing thermal conductivity. The *ZT* of Al and Ga dually doped ZnO ceramics could approach 0.65 at 1247 K, about twice the *ZT* of pure ZnO [45]. A single Sb-doped ZnO microbelt has a Seebeck coefficient of about -350 μV/K and a power factor of about 3.2×10^{-4} W/mK^2 [46].

However, based on the spontaneous polarization in certain anisotropic solids caused by a time-dependent temperature variation, the pyroelectric effect has to be chosen when it is in an environment with a spatially uniform temperature without a gradient [47, 48]. In pyroelectric theory, the pyroelectric current I_p can be presented as $I_\mathrm{P} = pA\frac{\mathrm{d}T}{\mathrm{d}t}$, where p is the pyroelectric coefficient, A is the electrode area, and $\mathrm{d}T/\mathrm{d}t$ is the temperature changing rate. The pyroelectric voltage V_p can be calculated by $V_\mathrm{p} = pd\frac{\Delta T}{(\varepsilon_\mathrm{r}-1)\varepsilon_0}$, where d is the film's thickness, ΔT is the temperature change, ε_r is the sample's relative

dielectric constant, and ε_0 is the free space permittivity. For the ZnO NWs with the average diameters of 200 nm, the pyroelectric current and voltage coefficient are ~1.2-1.5 nC/cm^{2}K and ~2.5-4.0×10^4 V/mK, respectively [47].

TABLE 1.2 Thermoelectric Cells of Some Typical Nanowires

Nanowires	*ZT*	Area	V_{oc} (mV)	I_{sc}	Description
PZT	n/a	n/a	60	0.6 nA	Single NW, 296 K-333K [49]
Si NW	0.6	n/a	n/a	n/a	Room temperature [32]
Si NW	~1	10 nm×20 nm	n/a	n/a	200 K [33]
InSb NW	~3	n/a	n/a	n/a	30 nm thickness [37]
InN NW	~1.6	n/a	n/a	n/a	1000 K [42]
ZnO NW	0.05	n/a	n/a	n/a	10 Å [43]
ZnO NW	0.1	n/a	n/a	n/a	970 K [44]
ZnO NW	n/a	~15 mm^2	~5.8	108.5 pA	pyroelectric effect [47]

1.2.3 Photovoltaic Cells

Photovoltaic (PV) cells are solar in nature, which suggests that the sun could be a promising power source for aircraft embeddable SHM sensors. Firstly, solar power density is higher in the upper atmosphere, since it increases regularly as altitude rises ─ from 80 mW/cm^2 (AM1.5) on the ground to 136.7 mW/cm^2 in space (AM0). Secondly, a solar powered aircraft produces no exhaust, and so unlike an O_2-consuming one, neither contaminates the atmosphere nor interferes with any delicate air measuring sensors on the aircraft. Thirdly, the production of solar power is independent of the atmosphere. Even if solar power is not available 24-hours a day, flight times may be extended by using battery or fuel cell power.

PV cells can generally be classified into two categories: more traditional free-carrier solar cells and excitonic solar cells. To transform photons of light into electrical energy, a large portion of the electromagnetic radiation is absorbbed from the sun to produce excited charge carriers that are diffused to an interface and separated before recombination losses occur. The semiconductor material used for a PV cell determines the mechanism of charge separation and transport. For solar cells made with more traditional inorganic semiconductors such as Si, GaAs, charge separation occurs spontaneously and transport relies on the field at the junction of two doped semiconductor materials. However, in excitonic solar cells, bound electron-hole pairs named "excitons" are formed upon light absorption by the active light absorption materials such as molecules, polymers, quantum dots, or nanowires, all of which separate into discrete carriers only at the junction of another material when energy levels are suitable for charge dissociation [34, 50, 51].

To efficiently convert solar energy into electricity or stored energy in chemical bonds, a PV cell should be thick enough to sufficiently absorb the light, but thin enough to efficiently collect the carrier before

losses are caused by heat dissipation. To alleviate the trade-off between light absorption and carrier collection, one approach is to employ an extremely thin absorption layer (ETA) on a structured substrate. Doing so allows significant optical absorption yet reduces charge carrier recombination greatly [52, 53]. Another solution is to enhance light trapping by using a surface texture such as that made by hydrochloric acid etching of ZnO:Al for a superstrate p-i-n structure [54], or that made by Ag back electrodes in a substrate n-i-p structure . In both, the incident light is scattered into off-normal angles, resulting in an increased optical path length in the absorber layer and enhanced light-absorption.

Recently, many studies have focused on the applications of nanostructures such as nanoforests, nanotubes, nanocoaxes, nanocones, nanodomes, nanopillars, nanorods, and nanowires for PV cells [55-62]. Due to the nanostructured devices' unique geometry, they have advantages in simultaneously enhancing charge collection and improving light absorption, compared to their planar thin film counterparts. In a real environment, the sun's movement can cause sunlight diffusion, leading to non-normal incidents to the solar cells, which can negatively influence the time-averaged output. Nanostructure-based PV cells perform better than their conventionally textured counterparts, because of multiple absorption opportunities. These opportunities originate with the internal multiple reflections of light back and forth between the elongated nanostructures under an angle [63]. Their distinctive properties make semiconductor NWs more promising components for solar energy conversion devices than other categories of nanomaterials [34]. NWs have the unique properties of one dimensional (1D) materials at their length scales, which can benefit the absorption, diffusion, and charge separation steps of solar energy devices. Not only do they provide high surface areas for increased light absorption, a high interfacial surface area, and small minority-carrier diffusion length, but they also offer a direct pathway for electron transport, resulting in increased electron recombination reactions. The advantages of greater light absorption within the NW arrays have been studied in silicon NW-based PV cells [55]. Depending on the NW dimensions, the vertically arrayed geometry efficiently scatters the light, especially at short wavelengths, and can absorb more light than a comparable thickness of solid crystalline film [64]. Because of larger series resistance of the NWs and their contacts, charge extraction through the NWs results in the decrease of J_{sc}. Conversely, silicon NWs' radial heterostructure has been demonstrated as the ideal design for efficient charge collection [61, 65, 66].

However, either using a Si-wafer as a starting material or employing a high synthesis temperature, whether these methods will eventually reduce material usage and/or energy consumption is unpredictable. Therefore, a simple fabrication process with low material usage at low temperature should be preferred. Zinc Oxide (ZnO) NW arrays generally are used as the backbone because of their several advantages, such as easy preparation on various cheap substrates (e.g., glass or plastic) by

solution-deposition at a temperature below 100°C, and the enhancement of both optical scattering and anti-reflection [67]. Moreover, during NW growth, the Fermi level of a single crystalline NW can be tuned by introducing doping elements [68].

NW diameters are smaller than or comparable to the sun's radiation wavelength; therefore, optical interference and guiding effects are dominant factors affecting reflectivity and absorption spectra [69]. Waveguiding effects are essential to low-absorbing materials such as indirect bandgap ones (e.g., silicon) [70, 71]; on the other hand, highly absorbing semiconductors, such as direct bandgap GaAs, exhibit resonances that increase the total absorption several times. NWs lying on a substrate also exhibit such resonances, described by Mie theory [72, 73], but with significantly lower total absorption rates . Without the constraint of lattice-matching requirements, NWs offer much more freedom to combine materials with the optimum bandgaps so that higher PV efficiency results. Strain relaxation at the NW sidewall surfaces can accommodate lattice mismatches in NWs without generating defects. Not being constrained by lattice-matching requirements, III-V NWs can be fabricated on relatively low-cost substrates such as Si [74-76]. Dong *et al.* have demonstrated single III-V NWs serving as PV cells that use InGaN/GaN core/shell NWs at triangular cross-section voltage (Ni catalyst, MOCVD growth) [77]. Single-NW devices achieve an open-circuit voltage, V_{oc} = 1~2V, a short-circuit current density J_{sc} = 59~390 μA/cm^2, and a best fill factor *FF* = 56%, while their conversion efficiency stands at ~0.19% under AM1.5G conditions because of the relatively low indium content. The highest PV efficiencies, above 44.4% under concentrated sunlight, are attained by using compound III-V InGaP/GaAs/InGaAs semiconductor material with research-grade PV cells [78].

TABLE 1.3 Photovoltaic Cells of Some Typical Nanowires

Nanowires	Efficiency (%)	Area (cm^2)	V_{oc} (V)	J_{sc} (mA/cm^2)	Fill factor (%)	Description
P3HT:CdSe	0.69		0.68	2.37	0.43	Different surface capping ligands [79]
Cu_2S/CdS			0.54	3.47 nA		A single coaxial NW [80]
ZnO	n/a	n/a	0.415	252 μA/cm^2	n/a	Hybrid device [21]
ZnO, P3HT:PCBM	1.5%	n/a	0.55	9.2	n/a	Hybrid device [22]
ZnO	3.3%		0.559	9.5	62.3	Optical fiber [81]
Si NWs	8.2%		0.893	13.9	65.8	Coaxial n-i-p Ag-coated Si NWs [82]
InP	13.8%		0.779	24.6	72.4	p-i-n doped [83]
InN	0.68		0.14	14.36	30.24	CdS passivated p-i-n NW [84]

1.2.4 Comparison of Energy Harvesting Techniques

The primary advantages and disadvantages of piezoelectric, thermoelectric, and photovoltaic energy harvesting technologies are summarized in **Table 1.4**. Harvesting efficiency is critical because high harvesting efficiency helps to reduce the dimensions of the harvester.

Designing efficient energy harvesting circuits involves considering complex compromises such as in the characteristics of the energy source, energy conversion efficiencies, power management, power storage, and application requirements [85, 86]. The efficiency of the energy harvester can be divided into several categories: conversion efficiency from one form to another (e.g., from vibration to electricity), transfer efficiency from the energy converter to the electrical load, storage efficiency, and consumption efficiency. A micro-scale energy converter can be configured as a single modality, a stack modality, or multiple harvesting modalities. The type of configuration significantly impacts the efficiency and performance of the power conversion circuitry attached to the output of the converter. In addition, energy harvesters, such as TEC or solar cells, produce DC, whereas vibration-based energy harvesters output AC, which needs extra AC-DC conversion (rectification) steps. The voltage and currents delivered by a harvester are often not compatible with the needs of the circuitry. Hence, voltage conversion and regulation are generally necessary, and also ensure that harvesters operate at high efficiency (maximum power point tracking, MPPT). Moreover, the power consumption can be dynamically adjusted to match the amount of power harvested, by using various power management techniques, thus leading to an adaptive and self-sustaining system [87, 88].

TABLE 1.4 Comparison of piezoelectric, thermoelectric, and photovoltaic energy harvesting technologies [89]

Source	Advantages	Drawbacks	Potential Applications
Piezoelectric ($1\text{-}10\ mWcm^{-2}$)	1) Compatible with MEMS/NEMS 2) Compact configuration 3) No separate external energy source needed 4) High energy density 5) Large voltage levels 6) Multifunctional material	1) Depolarization and aging problems 2) A poor coupling coefficient in the piezo thin film 3) Brittleness in the PZT material 4) Charge leakage and high output impedance 5) Each element has to be manually tuned to the vibration frequency 6) Hard CMOS integration	1) Remote sensing 2) Environmental monitoring 3) Structural-health monitoring 4) Wearable systems
Thermoelectric ($10\text{-}100\ uWcm^{-2}$)	1) No separate external energy source needed 2) No moving parts, capable of continuously supplying DC power 3) Reversible heating and cooling elements 4) No materials need be replenished 5) Long lifetime	1) Irreversible effects in thermoelectric materials limit their efficiency and economy for energy harvesting 2) Low efficiency for small temperature differences 3) Seebeck coefficient cannot be improved beyond a limit	1) Structural-health monitoring for engines and machines 2) Wearable biomedical devices
Photovoltaic ($10\text{-}100\ mWcm^{-2}$)	1) Photon source is infinite, high power output 2) Low operating and maintenance costs, system operation at ambient temperature 3) No hazardous material for disposal 4) High reliability in commercial modules, electricity can be generated at the point-of-use in most cases 5) Long lifetime	1) Photon source is not always available; depends strongly on day, night, and weather, limited by environmental conditions 2) High installation costs 3) Balance of system components and storage not as reliable as solar cells' 4) Commercial grid-connected systems are not in widespread use yet	1) Remote sensing 2) Environmental monitoring

1.3 Challenges and Research Objectives

The goal of this research is to study the use of semiconductor nanowire based piezoelectric energy harvesters for potential aircraft SHM applications. The research goal will be met by addressing the following harvester requirements: 1) it should not use an additional external power supply; 2) it should be small and light weight; 3) it should possess a very small physical and operational foot print; 4) the control circuit should draw minimum power; 5) it should possess simplified functions and be easily monitored; 6) it should have the least possible impact on aircraft systems and subsystems, and be integratable into the structure of the airframe as well as conform to its aerodynamic surfaces; 7) it should have very little impact on or even improve operation and maintenance procedures.

The requirements pose significant challenges in energy harvesting: 1) In an SHM application, sensor nodes must not be obtrusive or significantly alter the environment itself. The simplest way to accomplish this is by reducing the size of the sensor nodes. However, for piezoelectric vibration harvesters, decreasing the device size rapidly increases the resonant frequency and simultaneously gradually decreases the output power of generators; 2) the output power from thermal harvesters is also limited by small-scale sensors. Small-scale sensor nodes result in low output power as well as small temperature gradients that further reduce available power; 3) in SHM applications, sensor nodes are always embedded within structures; solar energy harvesting would be an option with small-scale and flexible energy transmission devices, providing a means to integrate devices into airframe structures as well as conform to aerodynamic surfaces. However, solar cells do not work well without sufficient sun light. Thus, the best solution is believed to be a hybrid one that harvests vibration, thermal, solar, electromagnetic energies simultaneously.

The project has been motivated by four main objectives: The first was to complete a comprehensive literature review that provides a solid understanding of energy harvesting techniques with potential aerospace SHM applications. The literature review also identifies gaps in current knowledge of energy harvesting for wireless self-powered system. To meet the second objective, based on this review, a physical model was developed. The piezoelectric properties of InN NWs were simulated using a software package. The simulations were also used to change specific parameters of the NWs so as to optimize voltage output. The aim here was to identify parameters that can be changed during the various stages of NG manufacturing in order to achieve a higher output voltage. Then, piezoelectric NGs based on vertically aligned InN NWs are fabricated, characterized, and evaluated. These NWs were crucial to the success of this project, and the material also needed to be easily synthesized to be considered suitable. Hence, the third objective was to find a synthesis method that consistently synthesized high quality NWs. Therefore, *p-n* homojunction ZnO NWs, using different doping concentrations to

determine which achieved the best results. Optimization techniques were applied to these growth methods with the aim of increasing the output power product. The fourth main objective of this project was to further increase NG's performance so that it can be of practical use. Towards this goal, a compact two-terminal hybrid energy cell (CHEC) that uses vertically-aligned *p-n* junction ZnO NWs was investigated. The design avoids the large output impedance typical with piezoelectric NGs: the bottom has a flexible *p-n* homogeneous ZnO NW array to harvest mechanical energy; the top has an *a*-Si:H single junction solar cell to harvest solar energy. The output power is sufficient to power nanodevices and even commercial electronic components.

1.4 Thesis Overview

The work addressed in this dissertation is intended to develop nanoscale energy harvesters with high-throughput for potential aircraft SHM applications. This thesis focused on 1) modeling semiconductor nanowires for piezoelectric energy harvesting, 2) characterizing and analyzing single nanowire material or energy harvester devices, 3) fabricating piezoelectric or hybrid energy harvesting devices.

The chapters of this dissertation are organized as follows: Chapter 2 gives a brief description of piezoelectric effect and the working mechanism to this work. Then it gives an account of the computational details. COMSOL 5.3 and FEM were used extensively for the simulations. This chapter discusses the carrier density, diameter, length; Schottky barrier height, temperature, and force of III-Nitride nanowires, all of which influence the output piezopotential. To further understanding piezoelectric effect on III-Nitride-based NWs, Chapter 3 describes efforts to characterize the piezoelectric potential of a single InN nanowire, using C-AFM. Furthermore, p-type III-Nitride NW-based piezoelectric nanogenerators have been fabricated and characterized. To achieve high performance piezoelectric NGs, Chapter 4 shows the approach for growing p-n junction type ZnO nanowires on a flexible PEN substrate for applications in energy harvesting; KPFM is used to characterize the surface potential of NWs with different doping concentrations. Flexible piezoelectric NGs have been fabricated and characterized. To fully utilize the energy available in our environment, Chapter 5 develops a technology that simultaneously harvests multiple types of energy, including solar and mechanical energy. Finally, Chapter 6 concludes with a summary of the research presented in this thesis and discusses future directions.

Chapter 2

Modeling of Nanowires-based Piezoelectric Energy Harvesters

2.1 Motivation

Recent research on piezoelectric harvesters is focused on designing, synthesizing, and characterizing new functional materials with controllable sizes, shapes, and/or structures. Thus, using nanotechnology to develop such devices and systems is attracting attention [90-93]. Piezoelectric nanogenerators (NGs) using nanowire (NW) arrays are a novel technology developed for scavenging mechanical energy. They have been shown to perform better than bulkier forms, with unique advantages such as having enhanced piezoelectric surface area, higher mechanical flexibility, high sensitivity to small forces, and being ideal templates on which to build other structures [94-96].

In 2006, Ref. [97] demonstrated that voltage could be generated when a single ZnO NW was bent by a conductive atomic force microscopy (AFM) tip. Hu *et al.* [98] introduced the first prototype of an integrated self-powered NG-driven system that works wirelessly for long-distance data transmission. Although the measured output power density was only 6 $\mu W\ cm^{-3}$, this demonstration proved the feasibility of using NGs in building self-powered systems. Since then, various NGs, made with poly(vinylidene fluoride) PVDF [99], BaTiO3 thin film [100], lead zirconate titanate (PZT) nanofibers [101], and based on piezoelectric effect have also been investigated for electricity generation under tension strain. Recently, piezoelectric NGs fabricated with nanomaterials (wurtzite structures) have attracted interest because of their superior mechanical and semiconductor properties. Most published studies on NGs using NWs rely on II-VI compound semiconductors such as ZnO, CdS, and ZnS to convert mechanical energy into electricity for self-powered, small scale, integrated nanosystems. The ground breaking work by Zhong L. Wang and his Nano Research Group at the Georgia Institute of Technology, USA, has greatly influenced current efforts to use NGs to convert nanoscale mechanical energy into usable electrical energy.

In 2007 and 2009, Gao and Wang theoretically calculated the potential distribution in a lateral ZnO NW, using finite element method (FEM) to solve a fully coupled nonlinear electromechanical system. The numerical calculation showed that the maximum piezopotential that can be generated at the NW surface is directly proportional to the lateral displacement of the NWs and inversely proportional to the length-to-diameter aspect ratio [102]. Charge carriers are accumulated at the stretched side of the ZnO NW, and the compressive side is largely depleted. Degeneracy in the positive side is significant, but the temperature dependence of the potential profile is weak, in the range of 100-400 K [103]. The behavior of free charge carriers in a compressed/tensioned ZnO was also invertigated, by Romano *et*

al. [104] and Araneo *et al*. [105], using FEM. The numerical calculation showed that the displacement, piezopotential, and charge concentrations under traction/compression drop between the tip and the base of the NWs as a function of force and donor concentrations.

NW III-nitrides, such as AlN, AlGaN, GaN, and InN, are noted for their tunability, direct band gap, high stability, and tolerance to moisture in the atmosphere, and are also characterized by a pronounced piezoelectric property arising from their wurtzite crystal structures [106]. Based on initial investigations, the increasing piezopotentials in the sequence of AlN, AlGaN, GaN, and InN lead to increasing levels of electricity generation [106]. However, AlN or AlGaN generates almost no power, owing to poor conductivity. The GaN NW arrays demonstrate an outstanding potential for piezoelectric energy generation, with a performance probably superior to that of ZnO NWs [107]. The highest voltage and current separately reported for single InN NW using a conductive AFM tip are 1 V and 205.6 nA, respectively [108, 109]. However, as high-quality GaN and InN nanomaterials are difficult to grow and fabricate, research on GaN- or InN-based NGs is just beginning, as is investigation into related theoretical calculation. This chapter discusses the piezoelectric and semiconductor properties of wurtzite compound nanomaterials, emphasizing III-nitrides semiconducting InN and GaN NWs.

2.2 Working Mechanism

Figure 2.1(a) shows the SEM image of the as-grown GaN NW array; the diameter and the length of the NWs are about 77 nm and 2 μm, respectively. The configuration of an integrated NG can be perpendicular, tilted, and wave/buckled, as shown in **Figure 2.1(b).** Different force directions (lateral force/compression/tension, shown in **Figure 2.1(c)** can be applied. The NWs are usually made of wurtzite materials, which simultaneously have piezoelectric and semiconductor properties. One end of the NWs is fixed to a bottom electrode, while the top end is left free and manipulated by a driving top electrode. The signal is output through an external load. To generate a measureable signal above the noise level from NGs, the presence of a Schottky contact at least at one end of the NWs is essential. In most cases, the contact between the NW and the bottom electrode is Ohmic. Once stress is applied by the top driving electrode, the piezoelectric charges are created at the end surface of the nanowire due to the piezoelectric effect and cannot move freely, which results in a macroscopic potential in the NWs. The stress modulates the local Fermi energy to change the Schottky barrier height and can serve as the driving force for the flow of electrons in the external load. According to the direction in which the stress is applied ─ lateral or vertical ─ the NG is divided into DC or AC type. However, whether DC or AC, the fundamental principle is similar. When the piezopotential is negative at the Schottky barrier side (near the driving top electrode), and positive at the Ohmic side (bottom electrode), as is the case with compression, the Fermi level of the top electrode is raised with respect to the bottom electrode.

a-1

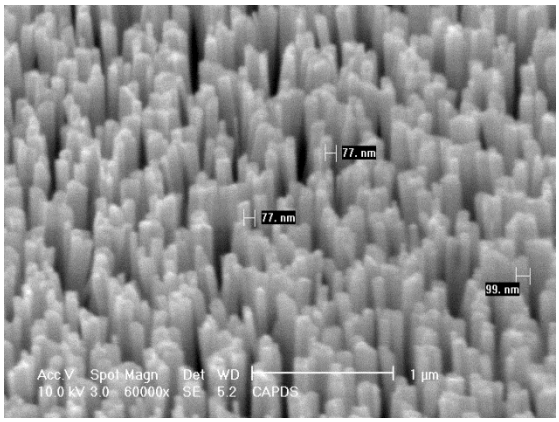

a-2

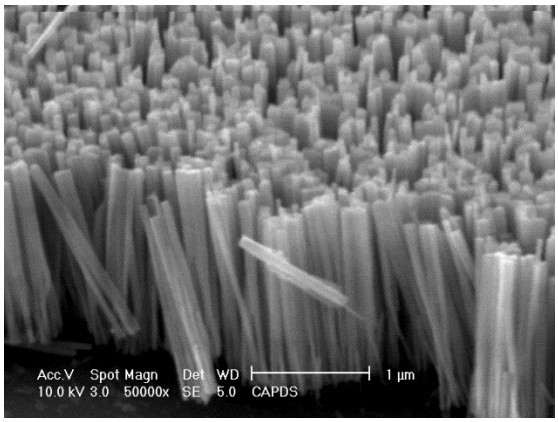

b-1

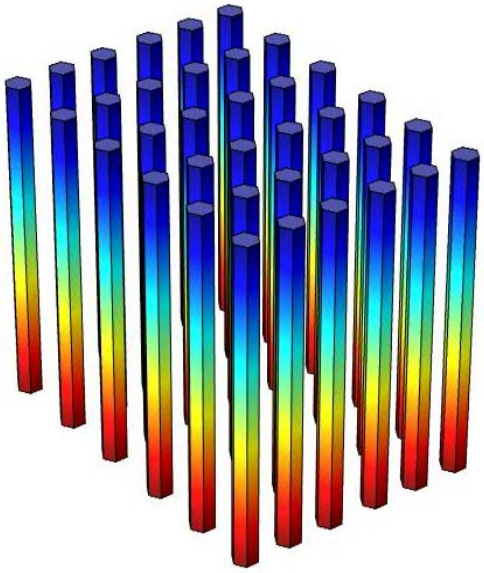

b-2

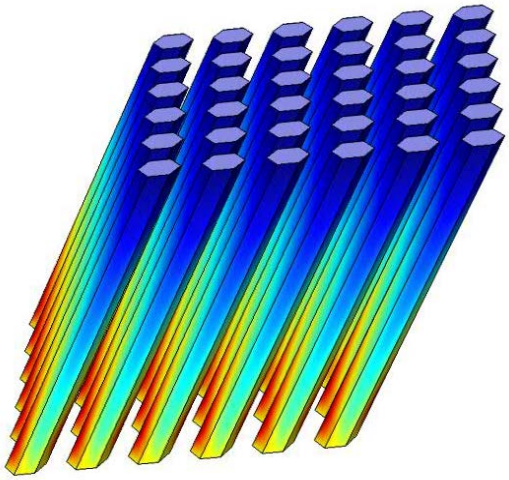

b-3

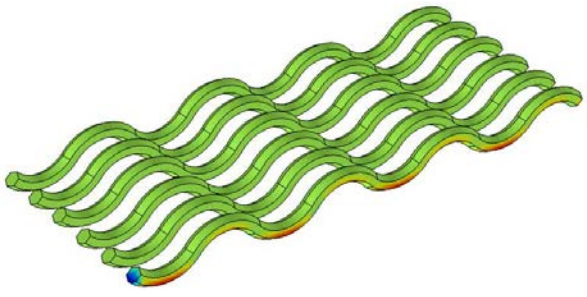

c-1

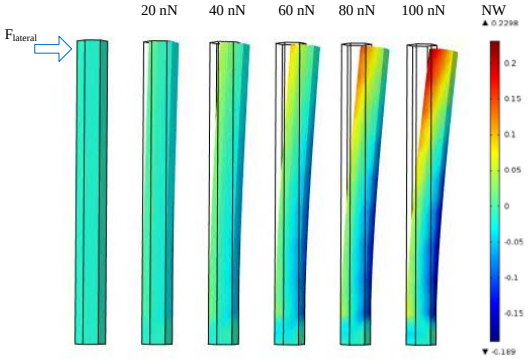

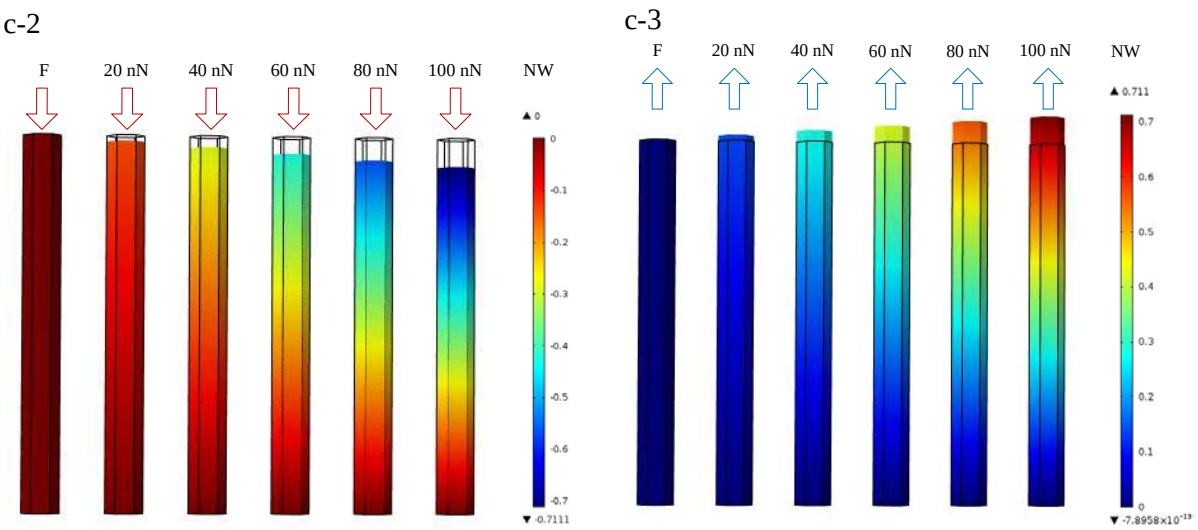

FIGURE 2.1 (a-1) SEM image of the as-grown GaN NW array. (a-2) Tilted cross-sectional SEM image of the GaN NW array. (b) Configuration for NGs using: perpendicular/tilted/wave/buckled NWs. (c) Different force directions: lateral force/compression/tension.

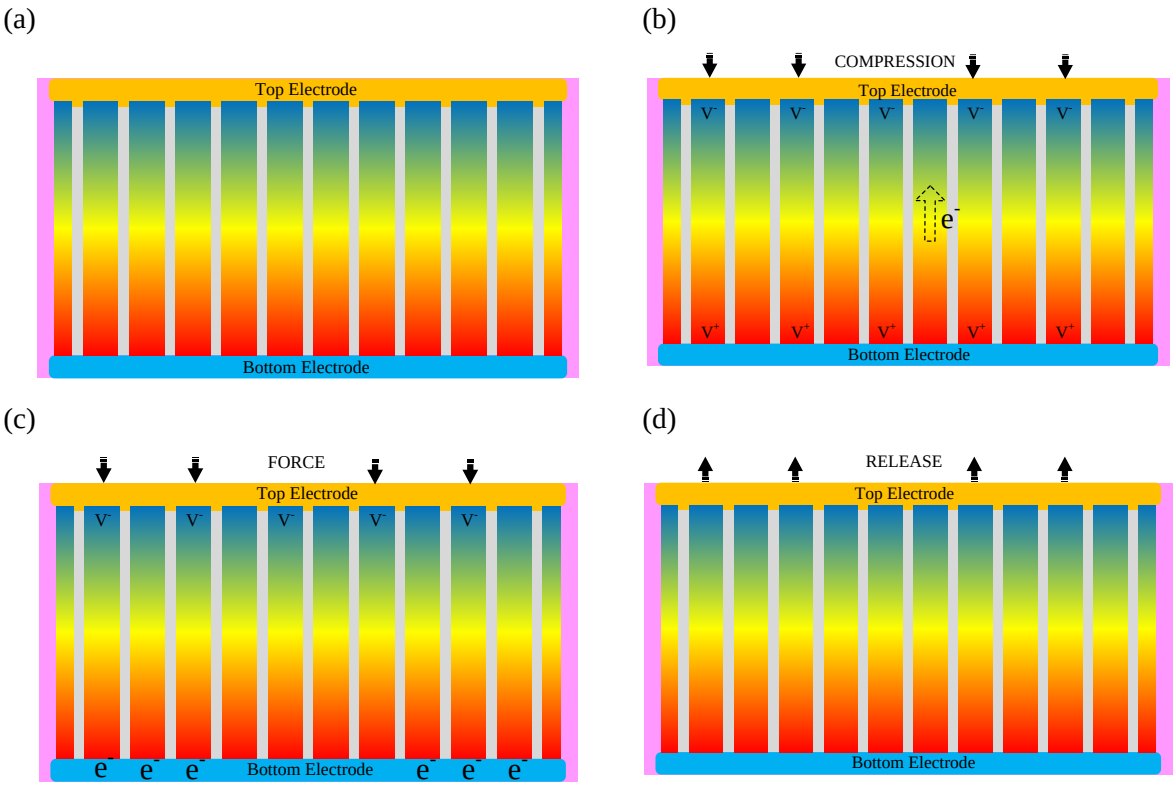

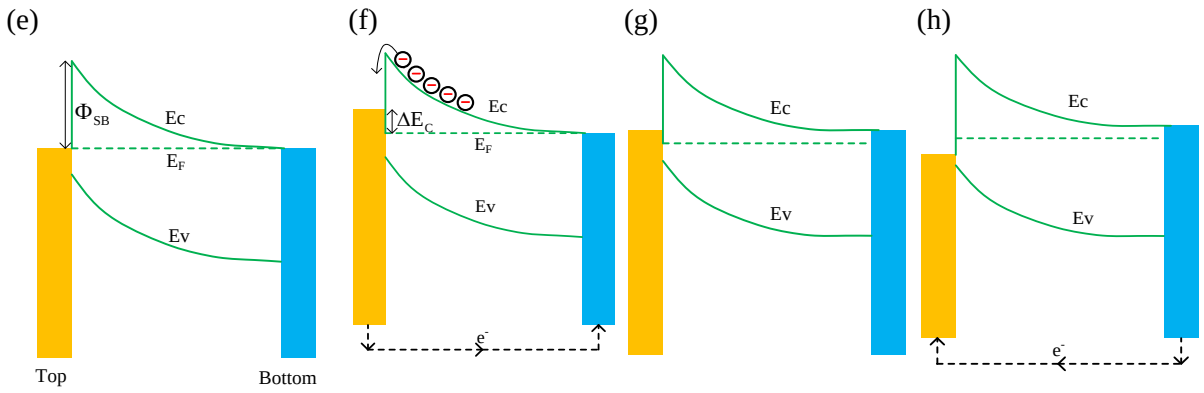

FIGURE 2.2 AC Power generation mechanism in vertically aligned NW-based NGs. (a) Vertically aligned NW-based NG in original state; (b) Electrons flow from the top electrode, contacting NWs with a negative potential to the bottom electrode through the external circuit under a compressive force; (c) This process continues until an electric potential due to the free moving electrons is created across the NWs to balance the piezopotential and the Fermi levels at the two electrodes, leading to a new equilibrium value; (d) The piezopotential-induced electrons are moved via the external circuit and accumulate at the interface between the bottom electrode and NWs with positive potential;(e-h)Schematic energy band diagram of the interface between metal and NWs and the changes of Schottky barrier by the piezopotential.

Electrons will then flow from the top electrode to the bottom electrode through an external load resistor. The electrons will enter the NW and screen the piezoelectric charges, leading to reduced local effective potential. This process continues until the Fermi levels of the two electrodes reach a new equilibrium value. When the strain is released, the disappearance of the piezopotential makes the free charges screening the piezoelectric charges free to move. The Fermi level of the top electrode drops to a lower one than that of the bottom electrode. In such cases, the electrons flow back from the bottom to the top electrode through the external load until the Fermi levels of the two electrodes balance again and the system returns to its original state. When the piezopotential is positive at the Schottky barrier side, the situation is almost opposite. **Figure 2.2** shows the AC power-generation mechanism in NGs with vertically aligned NWs.

2.3 Theoretical Framework

The theoretical basis of NGs is the creation of piezopotential when NWs are deflected. Thus, it is very important to know the voltage drop across NWs under different situations, such as the magnitude of stress, the ambient temperature, and the NWs' size and doping concentration. Numerous theories have

been proposed to calculate piezopotential across NWs, including first-principles calculations, molecular dynamics simulations, and continuum models. The first model is based on the Lippman theory [103], and can only be used for extremely low carrier concentration. However, in most practical cases, the as-grown NWs have a significant number of free carriers due to unavoidable defects. These free carriers redistribute in NWs because of the presence of piezoelectric charges and partially screen the piezoelectric charge. Therefore, the carrier concentrations may dominate the magnitude of the piezopotential directly. In this chapter, the piezopotential of the ZnO/GaN/InN wurtize family NW material is calculated using FEM and considering the finite carrier concentration. FEM is a universal method for solving differential equations, and has the character of generality and elegance, allowing a wide range of differential equations from all areas of science to be analyzed and solved within a common framework. It also has flexibility of formulation, allowing discretization properties to be controlled by the choice of approximation finite element spaces. These different materials will be comprehensively analyzed under different conditions.

To investigate deformed NWs' behavior, both the piezoelectric constitutive equation and the redistribution of electrons under thermodynamic equilibrium are considered by Fermi-Dirac statistics. The constitutive equation of the piezoelectric medium is given by [102, 103]

$$\begin{cases} \sigma_i = \sum_j c_{ij}\varepsilon_j - \sum_j e_{ji}E_j \\ D_i = \sum_j e_{ij}\varepsilon_j + \sum_j \kappa_0\kappa_{ij}E_j \end{cases} \tag{2.1}$$

where σ_i, ε_j, D_i, and E_j denote, respectively, the stress, the strain, the electric displacement and the electric field; c_{ij}, e_{ij}, and κ_{ij} are the mechanical stiffness tensor, piezoelectric coefficient, and relative dielectric constant, respectively. A constant temperature is assumed; otherwise, thermally induced effects such as elongation/contraction and pyroelectricity can occur. If the symmetry of a NW crystal (with a wurtzite structure) is considered, c_{ij}, e_{ij}, and κ_{ij} can appear as in [102]:

$$\begin{pmatrix} \sigma_{xx} \\ \sigma_{yy} \\ \sigma_{zz} \\ \sigma_{yz} \\ \sigma_{zx} \\ \sigma_{xy} \end{pmatrix} = \begin{pmatrix} c_{11} & c_{12} & c_{13} & 0 & 0 & 0 \\ c_{12} & c_{11} & c_{13} & 0 & 0 & 0 \\ c_{13} & c_{13} & c_{33} & 0 & 0 & 0 \\ 0 & 0 & 0 & c_{44} & 0 & 0 \\ 0 & 0 & 0 & 0 & c_{44} & 0 \\ 0 & 0 & 0 & 0 & 0 & \dfrac{(c_{11}-c_{12})}{2} \end{pmatrix} \begin{pmatrix} \varepsilon_{xx} \\ \varepsilon_{yy} \\ \varepsilon_{zz} \\ \varepsilon_{yz} \\ \varepsilon_{zx} \\ \varepsilon_{xy} \end{pmatrix} - \begin{pmatrix} 0 & 0 & e_{31} \\ 0 & 0 & e_{31} \\ 0 & 0 & e_{33} \\ 0 & e_{15} & 0 \\ e_{15} & 0 & 0 \\ 0 & 0 & 0 \end{pmatrix} \begin{pmatrix} E_1 \\ E_2 \\ E_3 \end{pmatrix} \tag{2.2.1}$$

$$\begin{pmatrix} D_1 \\ D_2 \\ D_3 \end{pmatrix} = \begin{pmatrix} 0 & 0 & 0 & 0 & e_{15} & 0 \\ 0 & 0 & 0 & e_{15} & 0 & 0 \\ e_{31} & e_{31} & e_{33} & 0 & 0 & 0 \end{pmatrix} \begin{pmatrix} \varepsilon_{xx} \\ \varepsilon_{yy} \\ \varepsilon_{zz} \\ \varepsilon_{yz} \\ \varepsilon_{zx} \\ \varepsilon_{xy} \end{pmatrix} + \begin{pmatrix} \kappa_{\perp} & 0 & 0 \\ 0 & \kappa_{\perp} & 0 \\ 0 & 0 & \kappa_{\parallel} \end{pmatrix} \begin{pmatrix} E_1 \\ E_2 \\ E_3 \end{pmatrix} \tag{2.2.2}$$

The fully-coupled non-linear partial differential equations to be solved are taken from [105]

$$\begin{aligned} \nabla \cdot \sigma &= 0 \\ \nabla \cdot D &= q(N_{\mathrm{D}}^{+} + p - N_{\mathrm{A}}^{-} - n) \end{aligned} \tag{2.3}$$

where q is the unit charge, p is the hole concentration in the valence band, n is the electron concentration in the conduction band, N_{D}^{+} is the ionized donor concentration, and N_{A}^{-} is the ionized acceptor concentration. Because the NWs are usually *n*-typed, we adopt $p = N_{\mathrm{A}}^{-} = 0$. The electron concentration in the semiconductor is computed by considering the parabolic electron band of the Fermi-Dirac statistics

$$n = N_{\mathrm{C}} F_{1/2}\left(-\frac{E_{\mathrm{C}}(x) - E_{\mathrm{F}}}{k_{\mathrm{B}} T} \right) \tag{2.4}$$

$$N_{\mathrm{C}} = 2\left(\frac{2\pi m_{\mathrm{e}} k_{\mathrm{B}} T}{h^2} \right)^{3/2} \tag{2.5}$$

$$F_{1/2}\left(-\frac{E_{\mathrm{C}}(x) - E_{\mathrm{F}}}{k_{\mathrm{B}} T} x \right) = \int_0^{\infty} \frac{E^{1/2}}{1 + \exp\left[E + \dfrac{E_{\mathrm{C}}(x) - E_{\mathrm{F}}}{k_{\mathrm{B}} T} \right]} dE \tag{2.6}$$

where k_{B} is the Boltzmann constant, h is the Planck's constant, T is the absolute temperature, m_{e} is the effective mass of conduction band electrons, $E_{\mathrm{C}}(x)$ is the conduction band edge with a function of space coordinates, E_{F} is the Fermi level, N_{C} is the effective state density of the conduction band. In particular, the band edge shift ΔE_{c} is the sum of the electrostatic energy part $q\phi$ and the deformation potential term, i.e.,

$$\Delta E_{\mathrm{C}} = E_{\mathrm{C}}(x) - E_{\mathrm{C0}} = -q\phi + \Delta E_{\mathrm{C}}^{\mathrm{def}} = -q\phi + \alpha_{\mathrm{def}} \frac{\Delta \nu}{\nu_0} \tag{2.7}$$

where E_{C0} is the conduction band edge of a free-standing un-deformed semiconductor material; ϕ is the electrostatic potential, and $\alpha_{def}\frac{\Delta\nu}{\nu_0}$ is the band-edge shift because of the deformation, proportional to the relative volume change $\frac{\Delta\nu}{\nu_0}$ with the deformation potential constant α_{def}. The ionized donor concentration is given by

$$N_D^+ = \frac{N_D}{1+\eta\exp\left[(E_F - E_C - \Delta E_D)/k_B T\right]} \tag{2.8}$$

where N_D is the concentration of the donors, η is the ground-state degeneracy of the donor impurity levels (usually $\eta = 2$), and $\Delta E_D = E_C(x) - E_D(x)$ is the level of the donors below the conduction band.

Physical parameters of these NW materials used in the potential calculation were collected from other references and are listed in **Table 2.1.**

TABLE 2.1 Dielectric constants used in the theoretical piezoelectric potential calculation

	Mechanical stiffness tensor (GPa)					Piezoelectric constants (C/m^2)			Relative dielectric constants			Density (kg/m^3)	Young's modulus GPa	Poisson's ratio
	c_{11}	c_{12}	c_{13}	c_{33}	c_{44}	e_{15}	e_{31}	e_{33}	k_{11}	k_{12}	k_{33}			
ZnO[a]	207	117.7	106.1	209.5	44.8	-0.45	-0.51	1.22	7.77	7.77	8.91	5680	129.0	0.349
InN[b]	223	115	92	224	48	-0.57	-0.57	0.97	13.1	13.1	14.4	6810	141	0.42
GaN[c]	390	145	106	398	105	-0.49	-0.49	0.73	9.28	9.28	10.01	6150	324	0.26

[a]Reference 103.
[b]Reference 108.
[c]Reference 107.

2.4 Results and Discussion

This section considers the case when force is applied vertically, corresponding to AC power generation. This case is favored for two reasons: first, the force along the polarization direction easily produces high piezopotential. That is to say, producing the same magnitude of piezopotential requires much less deformation than bending a NW by transverse force. Second, this case reflects the more common application of NG.

We first calculate the potential distribution along a ZnO/InN/GaN NW with a length L = 3.5 um and radius R = 57 nm when a compression force F = 100 nN is uniformly acting on the NW surface in the opposite direction parallel to the c-axis. The donor concentration is fixed at $N_D = 10^{16}$ cm^{-3}, which is quite similar to the case of as-grown ZnO. As shown in **Figure 2.3**, two obvious voltage drop regions

are presented. The free end shows a negative potential, and the fixed end shows a positive potential. Under the same conditions, ZnO generates a potential drop of 122.9 mV between the two end sides, which is obviously higher than InN with 86.8 mV and GaN with 29.0 mV. Thus, ZnO seems to be a more appropriate NG.

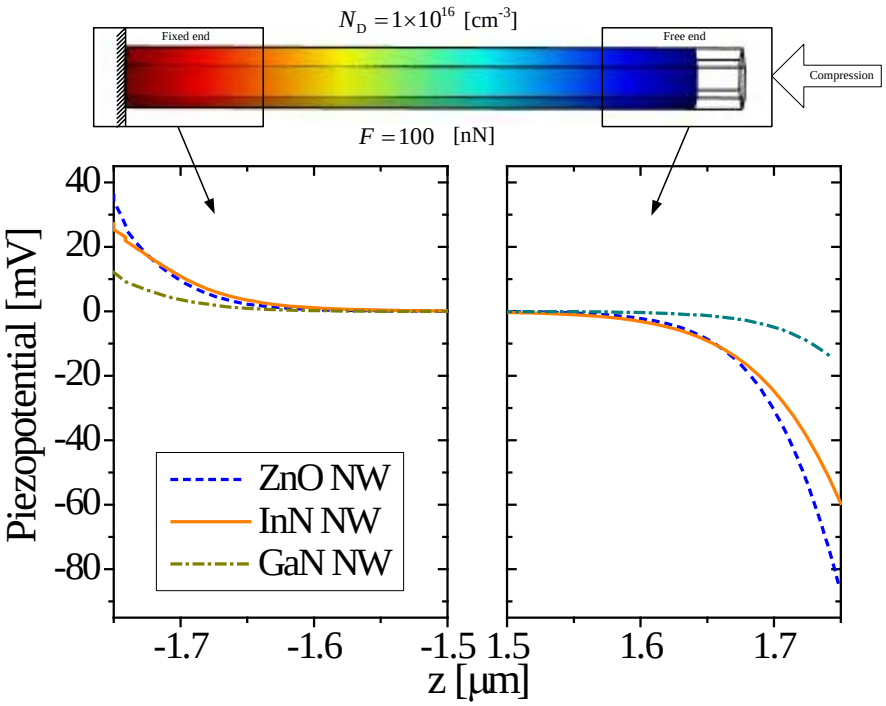

FIGURE 2.3 Piezopotential distribution of semiconductive ZnO/GaN/InN NW (R = 57 nm and L = 3.5 μm pushed by a uniaxial compressive force of 100 nN for a donor concentration of about N_D = 1×10^{16} cm^{-3}.

Though NWs with very low carrier concentration are preferred, the as-grown NWs are generally semiconductors with a certain carrier concentration. Due to the presence of piezopotential, the free carrier in NWs will redistribute to screen the piezoelectric charge and tend to neutralize the potential as a result. If the piezopotential is totally screened, the NG cannot work smoothly anymore. Therefore, one must know the free charge carrier's influence on the piezopotential and how much the piezopotential is neutralized.

Figure 2.4 shows the effect of the donor concentration of InN NW on (a) the potential, (b) the conduction band, (c) the free electron concentration, and (d) the activated donor concentration. Clearly, the potential continuously drops from the fixed end to the free end, corresponding to the conduction band (**Figure 2.4(b))** continuously increasing from the fixed end to the free end for any donor concentration. As the donor concentration increases, the potential distribution (following the

conduction band pattern) along the NW is more and more asymmetric, at around z = 0, and the magnitude of potential (like the conduction band pattern) at the two ends decreases. When the donor concentration is very low, e.g., $N_D = 1 \times 10^{11}$ cm^{-3}, the NW can be regarded as a dielectric and the effect of the carrier can be totally ignored. In such a case, the potential and the conduction band bending are affected only by the rigid and non-mobile piezoelectric charges located at the ends of the wire under compression. Because the piezoelectric charges are macroscopic ones resulting from displacement of the center of the cations and anions, the concentration of the positive and negative piezoelectric charges is equal, which leads to a symmetric potential distribution and conduction band bending along the InN NW. When the donor concentration increases, the free carrier concentration increases accordingly. The free electron will accumulate at the fixed end where positive piezoelectric charges exist (**Figure 2.4(c)**), resulting in the screening of piezoelectric charges at the fixed end. In contrast, the electron will be depleted at the free end, leaving the activated donor (**Figure 2.4(d)**). Thus, the local potential and the conduction band bending are modulated by the carrier concentration, and a new equilibrium will be established. Because, unlike the electrons, the activated donor cannot move freely, asymmetric potential distribution and conduction band bending occurs. The magnitude of potential that drops at the free end is larger than that at the fixed end where a screen of electrons acts as a major influence. When the donor concentration is large enough, e.g., $N_D = 1 \times 10^{18}$ cm^{-3}, the piezopotential is screened out almost completely, which corresponds to the conduction band distribution, the free electron concentration, and the activated donor. The maximum potential is only + 3.1 mV at the fixed end and – 6.0 mV at the free end.

Figure 2.5 displays the applied compression's influence on the potential distribution with L= 3.5 um, R = 57 nm and $N_D = 10^{16}$ cm^{-3}. The force ranges between 100 nN < F < 800 nN. The potential dropping along the NW is proportional to the applied force when the force is small, and tends to saturate gradually when the force is large enough. The maximum potential drop along the NW is about 700 mV under uniaxis stress. That is to say, the resultant voltage output of a NG cannot be modulated by increasing the external force infinitely.

Figure 2.6 shows the potential along NW when it is subjected to compressive/tensile force in both *n*-type and *p*-type InN NW. The length, radius, and donor concentration remain as above. It is seen that the potential distribution along the NW under compressive/tensile force is similar for both *n*-type and *p*-type material. For the *n*-type under compression, electrons accumulate at the fixed end and are depleted at the free end. In contrast, for the *p*-type under compression, holes accumulate at the free end and are depleted at the fixed end. Similar analysis is applicable for *n*-type and *p*-type NWs under tensile force.

(a)

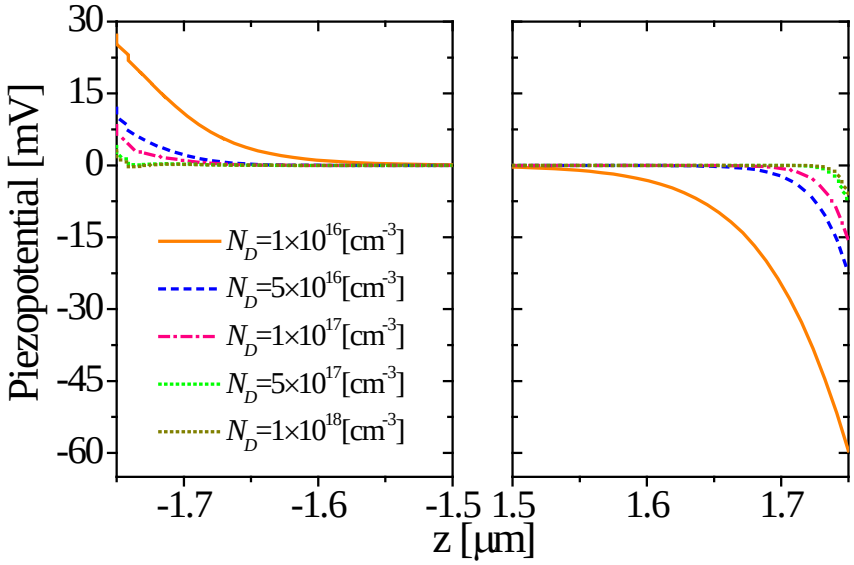
Piezopotential [mV]
30
15
0
-15
-30
-45
-60
N_D=1×10^{16}[cm^{-3}]
N_D=5×10^{16}[cm^{-3}]
N_D=1×10^{17}[cm^{-3}]
N_D=5×10^{17}[cm^{-3}]
N_D=1×10^{18}[cm^{-3}]
-1.7
-1.6
-1.5
1.5
1.6
1.7
z [μm]

(b)

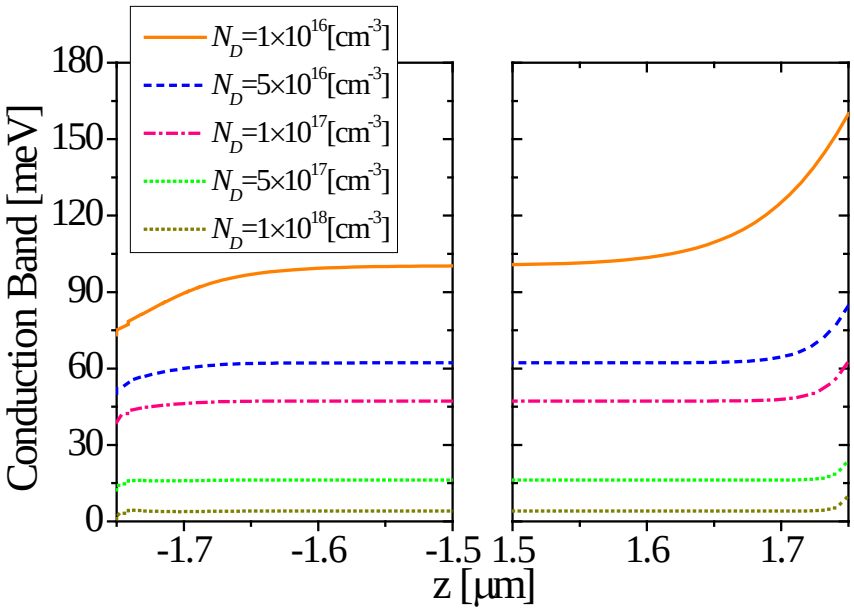
Conduction Band [meV]
180
150
120
90
60
30
0
N_D=1×10^{16}[cm^{-3}]
N_D=5×10^{16}[cm^{-3}]
N_D=1×10^{17}[cm^{-3}]
N_D=5×10^{17}[cm^{-3}]
N_D=1×10^{18}[cm^{-3}]
-1.7
-1.6
-1.5
1.5
1.6
1.7
z [μm]

(c)

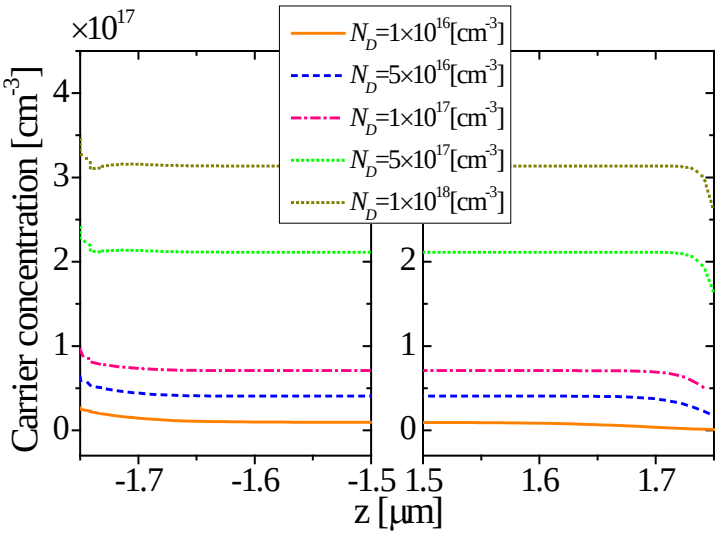

(d)

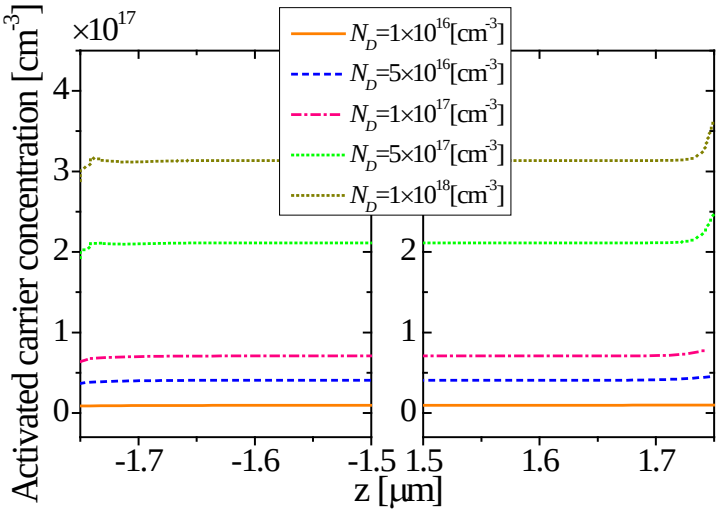

FIGURE 2.4 (a) Piezopotential distribution of a semiconductive InN NW (R = 57 nm and = 3.5 μm) pushed by a uniaxial compressive force of 100 nN (corresponding to a stress σ = 11.847 MPa) for different donor concentrations. The conduction bands and electron density in the presence of free charge carriers are shown in (b) and (c), respectively. The conduction bands, which refer to the Fermi level (set to zero), are deflected in the region near the free end of the NW, but if the donor concentration increases, the conduction bands tend to reach the Fermi level, thus screening out the piezopotential. In (d), the activated donor center concentration is shown.

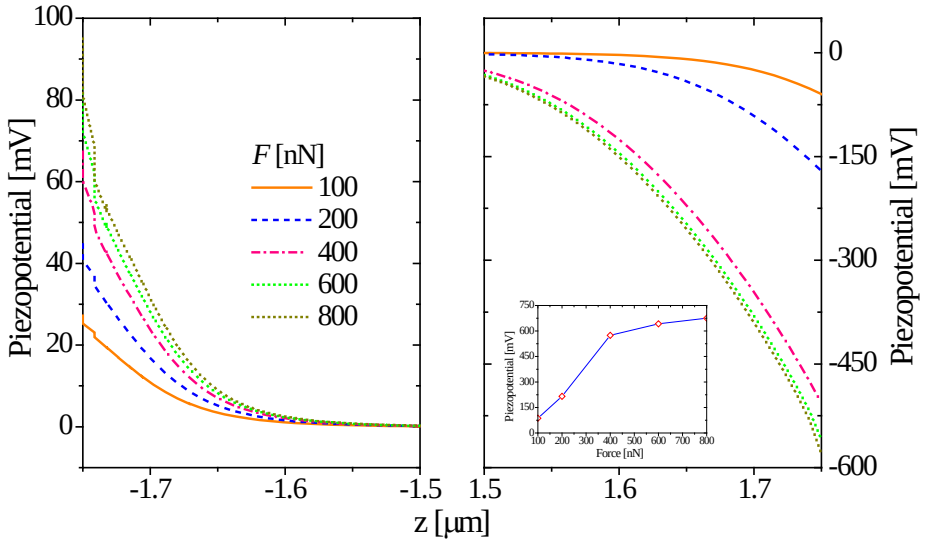

FIGURE 2.5 Piezopotential of InN NW (R = 57 nm and L = 3.5 μm) under different compressive forces at $N_D = 1\times10^{16}$ cm^{-3}.

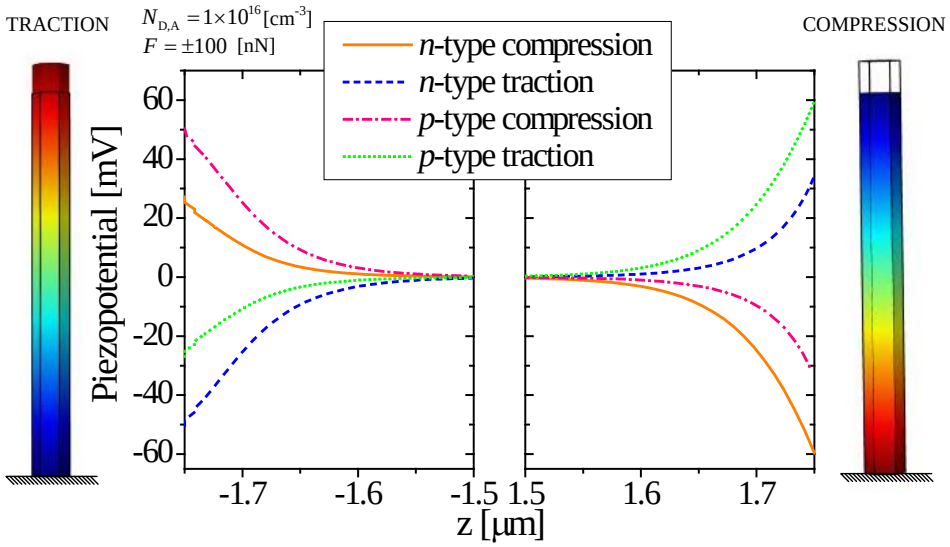

FIGURE 2.6 Piezopotential of InN NW (R = 57 nm and L = 3.5 μm) surrounded by free space and subject to compressive/tensile force in *n*- and *p*-type NWs.

It is known that temperature may affect the free carrier concentration of semiconductors, changing the resultant potential. Investigating the stability at different temperatures is thus essential to practical NG use. In **Figure 2.7**, we calculate InN NW's piezopotential when the temperature varies from 100K to

400K. Temperature influences the potential of InN NW weakly at the wire's center and significantly at both ends. The potential increases at the free NW end from 45.3 mV at 100K to 65.6 mV at 400K, indicating that the environment temperature may be considered deliberately in practical use.

The influence of NWs' geometric dimensions on electric potential has also been investigated for InN NW, as shown in **Figures 2.8** and **2.9**. In **Figure 2.8**, the length L = 3.5 um and $N_D = 10^{16}$ cm^{-3}, the electric potential drop across the NW is inversely proportional to the square of the radius, consistent with the analytical result obtained from $V_{max} = Fg_{33}L/A$, where F is the force applied to the free end electrode, or the force applied in stretching the NWs, g_{33} is the piezoelectric voltage coefficient of the NWs, L is the length of the NWs and A is the contact area of the NW [110]. When R = 100 nm, the piezopotential can be completely screened out under the donor concentration of $N_D = 10^{16}$ cm^{-3}. Thus, an ideal piezopotential NG depends on a proper choice of radius and donor concentration. As for the NW length, this matter remains controversial. In **Figure 2.9**, we investigate the effect of length on piezopotential, when R = 57 nm, $N_D = 10^{16}$ cm^{-3}, F = 100 nN and the length of NW varies between 2.5 μm < L < 5.0 μm. It is shown that NW length rarely influences the piezopotential except when the donor concentration is low enough, e.g., $N_D = 10^{14}$ cm^{-3}. When $N_D = 10^{14}$ cm^{-3}, the piezopotential drop across the NW changes approximately linearly. The maximum piezopotential for L = 2.5 μm is about -299.8 mV, which drops to -352.9 mV when the length is doubled to 5 um.

According to the working mechanism of piezopotentatic NG, to generate a measureable signal above the noise level, a Schottky contact is essential at least at one end of the NWs. Therefore, a Schottky contact is especially important for piezopotential NGs. In **Figure 2.10**, the effect of the height of the Schottky barrier between Pt and InN NW is investigated. The height of this barrier is chosen to be the data range published in different studies. The barrier height affects the potential near the NW's free end significantly, because it changes the electron distribution accumulated near the fixed end.

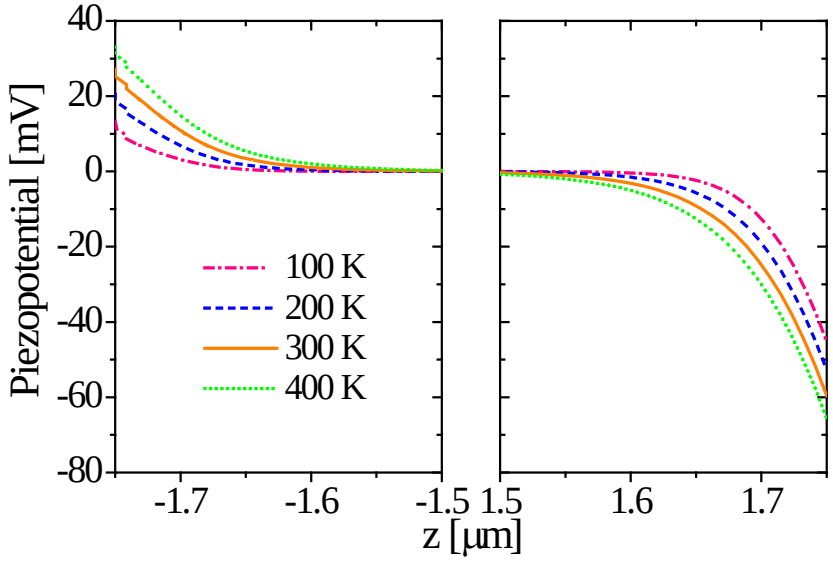

FIGURE 2.7 Piezopotential of InN NW (R = 57 nm and L = 3.5 μm) under different temperatures under compression at 100 nN and $N_D = 1\times10^{16}$ cm^{-3}.

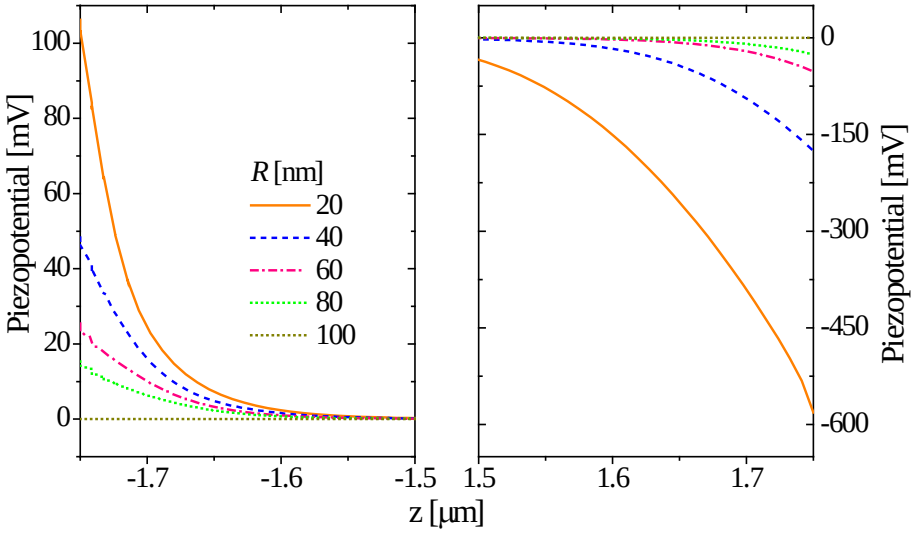

FIGURE 2.8 Piezopotential of InN NW (R = 57 nm and L = 3.5 μm) under different radius at $N_D = 1\times10^{16}$ cm^{-3}.

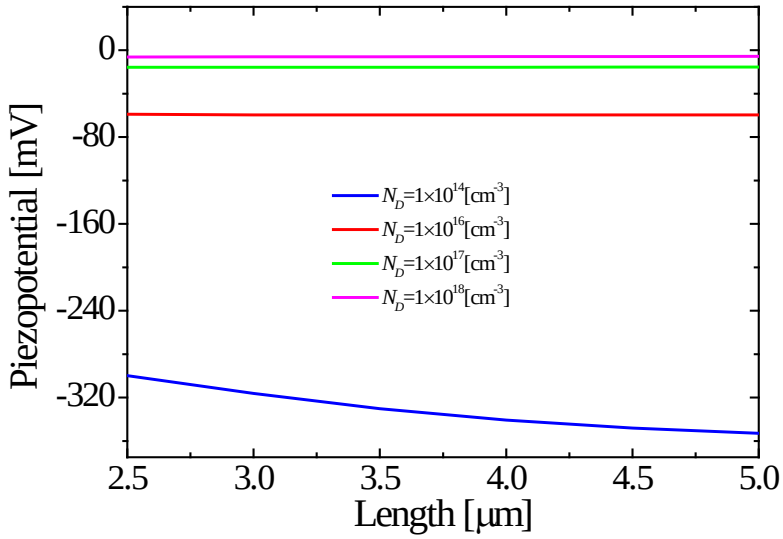

FIGURE 2.9 Piezopotential of InN NW (R = 57 nm) under different length at the top side.

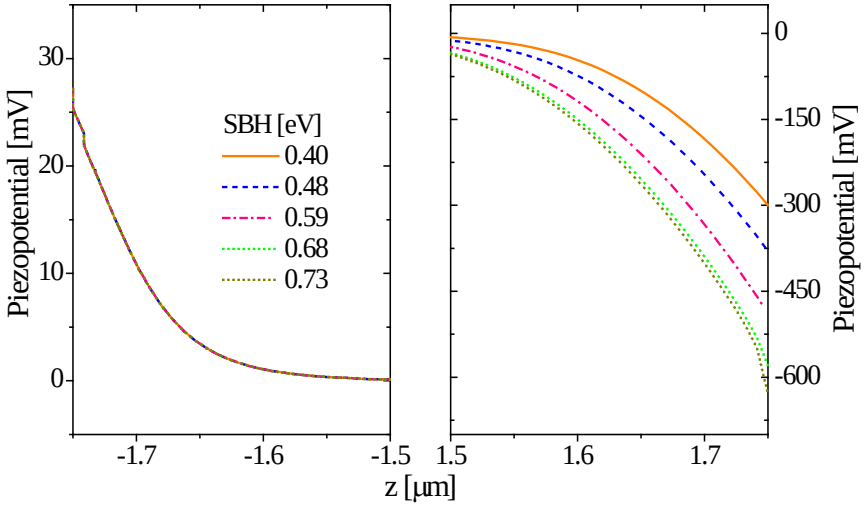

FIGURE 2.10 Piezopotential of InN NW (R = 57 nm and L = 3.5 μm) under different SBH at N_D = 1×10^{16} cm^{-3} with compression at 100 nN.

2.5 Conclusion

Compared to conventional piezoelectric material-based mechanical energy harvesters, using NWs would potentially improve the energy conversion efficiency, enhance the sensitivity to low-level mechanical energy sources, and extend the device lifetime. ZnO is the first nanomaterial that has been

applied for NG development. However, this chapter is focused on III-Nitride based NWs or NGs, III-nitrides, such as AlN, AlGaN, GaN, and InN, are noted for their tunability, direct band gap, high stability and tolerance to moisture in the atmosphere, and are also characterized by a pronounced piezoelectric property arising from their wurtzite crystal structures. The influence of different parameters on the equilibrium piezopotenital distribution in a deformed semiconductive NW has been systematically investigated. The donor concentration has been shown to markedly affect the electric potential distribution. In particular, a donor concentration of $N_D > 10^{18}$cm^{-3} will neutralize the electric potential across the NW. Increasing the applied force has been shown to increase the value of the electric potential. The influence of geometric parameters has also been investigated: the length of the NW does not affect the electric potential distribution, whereas an increase in the radius of the NW does decrease it. The Schottky barrier height affects the potential near the NW's free end significantly, because it changes the electron distribution accumulated near the fixed end. Finally, it must be pointed out that the above results were obtained for the equilibrium case. In reality, the dynamics have to be taken into account if the mechanical deformation process is rather fast.

Chapter 3

III-Nitride Nanowire-based Piezoelectric Energy Harvester

3.1 Motivation

Nanowire (NW) arrays' unique advantages, such as high surface area, relatively high flexibility, and sensitivity to small forces, make them ideal candidates for piezoelectric nanogenerator (NG) applications [34, 90, 111, 112]. Under external dynamic strain, such NGs produce a piezoelectric potential (piezopotential) in their NWs, which is then balanced by a corresponding transient flow of electrons through an external load [113]. Under applied strain, the ions of crystals within the non-centrosymmetric wurtzite structures of semiconductors such as ZnO, GaN, InN, and CdS become polarized, generating piezopotential [114]. The simultaneous possession of piezoelectric and semiconductor properties strongly affects carrier transport at interfaces and junctions where the piezopotential is created in NWs.

The NWs based on III-nitrides such as AlN, AlGaN, GaN, and InN are noted for their tunability, direct band gap, high chemical stability, and strong resistance to atmospheric moisture [108, 115]. Earlier research revealed that the piezopotential and piezoelectricity of these materials increase in the sequence AlN, AlGaN, GaN, and InN [115]. Due to their very poor conductivity, intrinsic AlN and AlGaN cannot produce electric output power upon the application of mechanical strain. In contrast, InN NWs demonstrate outstanding potential for piezoelectric energy generation, outperforming ZnO and GaN NWs' [107, 109, 115]. Furthermore, InN can be grown on Si substrates at low temperature, within the complementary metal-oxide-semiconductor (CMOS) thermal budget, thereby enabling its integration with Si CMOS technology. InN is also critically important for ternary III-nitride semiconductors, such as In(Ga)N-based devices [116-126], which are being widely adopted by the semiconductor industry. Unlike arsenide and phosphide-based materials, InN is environmentally friendly and much safer to use.

While, GaN-based devices and systems are relatively mature, indium-containing III-nitride devices remain underdeveloped, hampered by InN planar/bulk structural challenges, such as uncontrolled surface electron accumulation, and by difficulties in realizing *p*-type and intrinsic InN. Because of highly efficient strain and thermal relaxation in NW lateral surfaces [127-129], the large dislocation density observed in InN planar structures grown on lattice-mismatched substrates can be substantially minimized using nanowire structures.

This chapter investigates the use of InN NW arrays to develop piezoelectric NGs. It demonstrates for the first time NGs based on *p*-type and intrinsic InN NWs. A systematic study is carried out to compare the materials of *p*-type and intrinsic InN NWs, and the performance of piezoelectric NGs based upon

them. Section 2 describes the fabrication and characterization of the NWs and NGs. Section 3 reports the results of those experiments. Section 4 analyzes the characteristics of *p*-type and intrinsic InN NWs and the performance of NGs based on them, while section 5 concludes this chapter.

3.2 Experimental Section

3.2.1 InN NW Growth

Using radio frequency plasma-assisted molecular beam epitaxy (MBE), magnesium (Mg)-doped (*p*-type) and nominally un-doped (intrinsic) InN NWs were grown on separate Si (111) substrates under nitrogen-rich conditions by means of the InN NW growth procedure detailed in [120, 124, 130]. A thin (~ 0.6 nm) indium seeding layer was deposited on Si substrates before introducing nitrogen. This layer forms nanoscale droplets at high temperature, enhancing subsequent nucleation and growth of InN NWs. The *p*-type and intrinsic InN NWs were grown at a substrate temperature of ~ 480 °C, an indium beam equivalent pressure of ~ 6×10^{-8} Torr, a nitrogen flow rate of ~ 1.0 sccm, and an RF plasma forward power of ~ 350 W. Under these optimized growth conditions, nominally un-doped InN nanowires are nearly intrinsic. To grow *p*-type InN NWs, a magnesium (Mg) cell was introduced into the chamber.

3.2.2 NW Characterization

The morphology and crystalline structure were investigated using a field-emission scanning electron microscope (FE-SEM, Zeiss) and a high resolution X-ray diffraction (XRD) system (Jordan Valley QC3). Raman spectroscopy was taken at room temperature, using a HeNe laser operating at a wavelength of 632 nm and power of 30 mW, with its focal spot tuned to a diameter of ~ 5 μm. The samples' electric and piezoelectric properties were investigated using conductive atomic force microscopy (C-AFM, SmartSPM^{TM}-1000, AIST-NT) with platinum-coated conductive tips (HQ: NSC14/Pt, MikroMasch) with a force constant of ~ 5 N/m. Kelvin probe force microscopy (KPFM) imaging was conducted using MikroMasch HQ-NSC15/Pt tips with a natural frequency of ~ 325 kHz and force constant of ~ 40 N/m. The examination was carried out in amplitude-modulation (AM) mode simultaneously with the topography, by scanning the lines twice (once for height and another for KPFM) at a setoff distance of 10 nm. AM-KPFM offers significantly enhanced resolution and sensitivity over the more traditional lift mode KPFM. The scan rates were kept low (0.5 – 1 Hz) for optimal image quality.

3.2.3 Device Fabrication

To fabricate the nanogenerators (NGs), an insulating layer made of polymethyl methacrylate (PMMA), MicroChem 950k A11, was spin-coated to encapsulate the NWs. The PMMA layer was then cured at

90 °C for 3 hours. The encapsulation protects the NWs from damage under mechanical strain and prevents electrical shorting between the NWs' electrodes [11]. It does not prevent the application of external strain to the NWs, due to the PMMA's compliance [131]. To increase the interfacial energy barrier and protect against the inconsistency of the PMMA polymer matrix, a thin (10 nm) molybdenum oxide (MoO_3) interlayer was deposited atop the PMMA polymer matrix by vacuum thermal evaporation, immediately followed by a 50 nm thick gold (Au) cathode layer to complete the devices. Silver paste was used to glue Cu wire leads to the bottom highly doped Si substrate and the top Au electrode. The completed NGs' area was 9×9 mm^2. They were encapsulated in polydimethylsiloxane (PDMS), Dow Corning Sylgard 184 premixed with curing agent at a ratio of 10:1 w/w and degassed, to prevent contamination, damage, and moisture penetration from the ambient environment.

3.2.4 Device Characterization

Characterizations of the fabricated InN NW-based piezoelectric NGs was performed using a closed loop (Vibration Research Corporation, VR9500) electromagnetic shaker (Labworks Inc., ET-126B-1). The NGs output voltage and current signals were measured using Stanford low-noise voltage/current preamplifiers (Model SR560/570) and a National Instruments I/O module (NI CompactDAQ USB-9239). The input resistances of the preamplifiers were set to 100 MΩ (SR560) and 10 kΩ (SR570), respectively, for voltage and current measurements. To minimize electromagnetic interference, two copper wires connected to the NG leads were twisted together. All measurements were taken at ambient room temperature.

3.3 Results

Figure 3.1a shows a 45°-tilted SEM image of as-grown *p*-type InN NWs on a Si (111) substrate. The NWs exhibit a non-tapered surface morphology with a well-defined hexagonal structure and nearly perfectly straight and smooth surfaces along the *c*-axis. The typical *p*-type NW diameter and length were 400 nm and 1.0 μm, respectively, and the areal density was 8×10^7 cm^{-2}. The typical intrinsic NW (**Figure 3.1b**) diameter and length were 500 nm and 0.7 μm, respectively, and the areal density was 3×10^6 cm^{-2}. We define the NW aspect ratio, α, as the average NW length divided by the average NW diameter, and the fill ratio, β , as the average NW diameter divided by the average NW pitch. We observe that *p*-type InN NWs have a higher aspect and fill ratio, of $\alpha_p = 2.5$ and $\beta_p = 0.3$, than intrinsic NW at $\alpha_i = 1.4$ and $\beta_i = 0.1$, a finding consistent with [124, 130].

Figure 3.2 shows the 2θ-scan spectra of the XRD intensity for *p*-type and intrinsic NWs. The sharp peak at 31.4°, corresponding to the (002) plane, reveals the highly crystalline quality of the InN NWs and their *c*-axis preferred orientation. The full width at half-maximum (FWHM) of the θ-rocking curve

of the (002) peak is 0.23° (**Figure 3.2**, inset), demonstrating the NWs' excellent alignment. The intensity of the diffraction peak in the XRD 2θ-scan of the *p*-type InN NWs is much stronger than that of the intrinsic NWs, confirming that incorporating Mg dopants enhances NW growth along the preferred direction [130]. When measured, the Raman spectrum of *p*-type InN NWs (Figure S3.1) exhibited a very narrow E_2^h phonon peak at 488 cm^{-1} (FWHM = 4 ± 0.1 cm^{-1}) and an A_1 (LO) phonon peak at 593 cm^{-1} (FWHM = 9 ± 0.1 cm^{-1}). We conclude that *p*-type InN NWs are strain-free and of high crystalline quality.

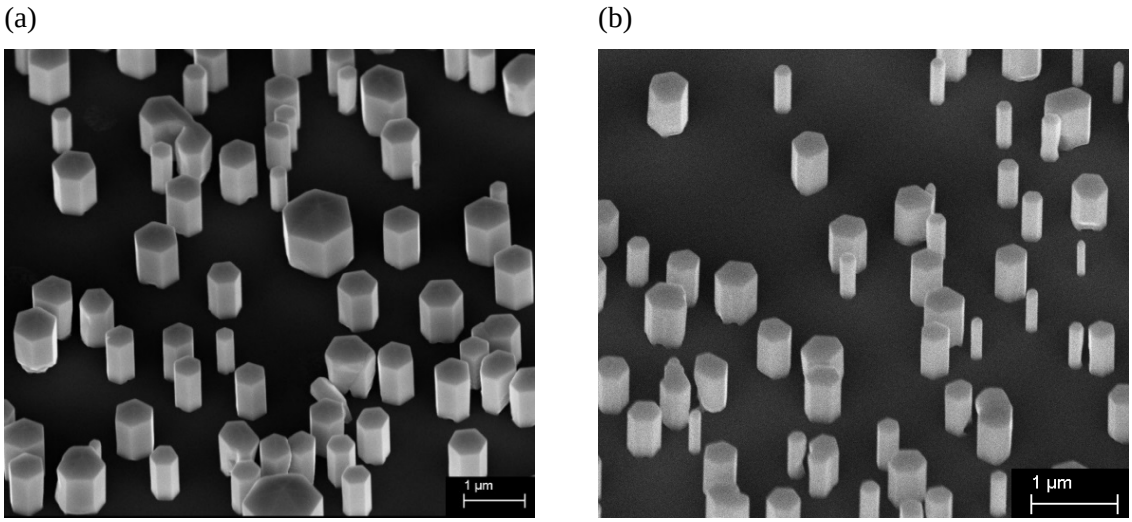

FIGURE 3.1 SEM images of non-tapered (a) p-type and (b) intrinsic InN NWs grown on Si (1 1 1) substrate, taken at a 45° angle.

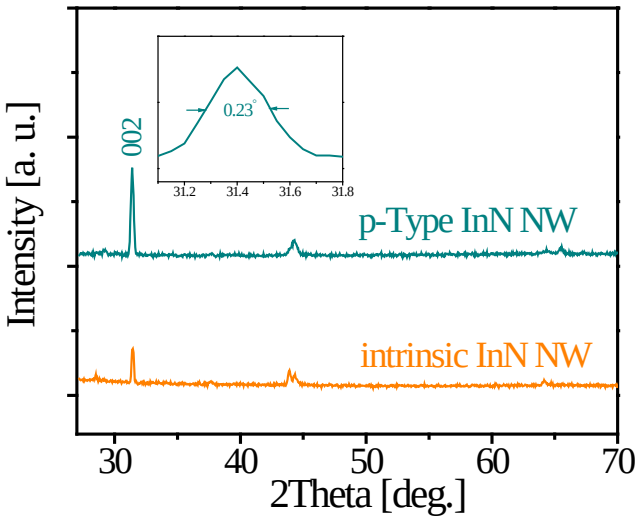

FIGURE 3.2 The 2θ-scan spectra of the XRD intensity for p-type and intrinsic InN NWs, demonstrating the high crystalline quality of as-grown NWs on silicon substrate.

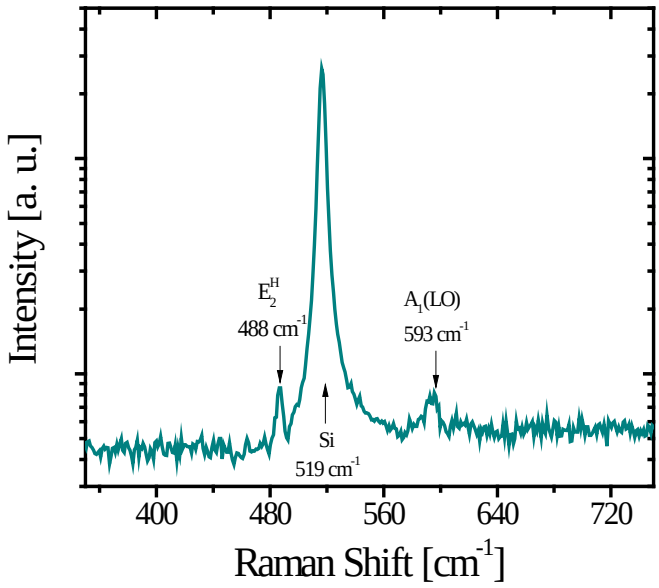

FIGURE S3.1 Room-temperature Raman spectrum of Mg-doped InN NWs, showing a very narrow E_2^h phonon peak at 488 cm^{-1} and A_1(LO) mode at 593 cm^{-1}.

The piezoelectric properties of *p*-type InN NWs were first investigated using conductive AFM, **Figure 3.3a.** A Pt/Ir coated Si cantilever probe scans in contact mode across an array of as-grown NWs at a speed of 10 μm/s under a constant compressive force of 66.7 nN. The scan simultaneously captures both the topography of the NWs and their corresponding piezoelectric current. The bottom profile in **Figure 3.3b** presents a typical current profile, in which electric current spikes of up to more than 300 pA occur at the leading edge of each nanowire, along the AFM probe scanning direction (left to right). The electric current signal is roughly two orders of magnitude higher than the noise level incurred with the C-AFM scan (~3 pA). This current arises due to the compressive load applied to individual NWs by the AFM tip.

The inset in **Figure 3.3b** shows an AFM topography image of the NWs under test. The scan line is marked with a dashed line in the inset. The peaks in the topography profile, the upper curve in **Figure 3b**, indicate that the NW heights are about 1.0 μm, consistent with the SEM images shown in **Figure 3.1a**. The profile also indicates that the diameter of individual NWs is ~900 nm, which is much higher than that measured by SEM (~400 nm). This value is an artefact caused by the conic shape of the probe tip (cone angle 40°) and the flexibility of the NWs. Contact typically occurs between the side face of the probe tip cone and the NW. As the probe continues to scan, it drags the wire with it. As the wire deforms, the probe tip climbs across the NW top and drags the NW along with it, until the tip leaves

the NW top surface. The two consecutive spikes in the electric current profile on the right-hand side of **Figure 3.3b** occur because two neighbouring nanowires in a row are in very close proximity, such that the topography profile is unable to distinguish them as two individual wires. They instead appear as a joint and broader peak.

The good correlation between the location of electric current spikes and the leading edge of the NWs indicates that the measured electric current is indeed generated by the InN NWs as they are compressed. For further confirmation, four experiments (Figure S3.2) were carried out to exclude the possibility that the output current arose from friction, contact potential, or other artefacts:

1) Similar C-AFM scans of a heavily doped Si film show no detectable current signals, which indicates that Si has no piezoelectric effect [132]. This is consistent with the noise floor results observed in the troughs of Fig. 3b where the tip contacts the Si substrate.

2) C-AFM scans of doped GaN NWs (highly conductive) produce no detectable current signals due to a screening effect, where the positive and negative charges generated piezoelectrically are completely compensated for by free charge carriers [133, 134].

3) C-AFM scans of intrinsic GaN NWs lead to sharp output current spikes, attributable to the piezoelectric effect and similar to those reported in **Figure 3.3b**.

4) C-AFM scans of *p*-type InN NWs with a Si tip detect no current signals because of Ohmic contact between the Si tip and the NW. Typically, a Schottky contact is needed to detect piezoelectric signals.

In summary, all observations support the conclusion that the electric current signals measured on *p*-type InN NWs originate from the NWs' piezoelectric effect.

Figure 3.3c and **d** show three-dimensional images of electric currents measured from *p*-type and intrinsic InN NWs in C-AFM over an area of 10 ×10 μm^2, respectively. Most of the current spikes from the *p*-type InN NWs are positive, with a maximum output current of 331 pA. Only a few negative current spikes (less than 0.02% of the whole population) are observed exhibiting a smaller magnitude of -20.5 pA or less. Thus, the overall negative current output is negligible compared to the positive current output. The inset of **Figure 3.3c** shows a histogram of the measured piezoelectric current. Quantitative analysis reveals that these NWs can produce an average output current density of 90.7 ± 70.6 pA over 100 μm^2 area. Four *p*-type InN NW samples were tested, producing similar results. For intrinsic NWs, the current spikes have large fluctuations, with a maximum output current of 600.9 pA, while most current spikes are below 50 pA. The inset of **Figure 3.3d** shows a histogram of the measured piezoelectric current. These NWs can produce an average output current density of 101.8 ± 127 pA over a 100 μm^2 area.

(a)

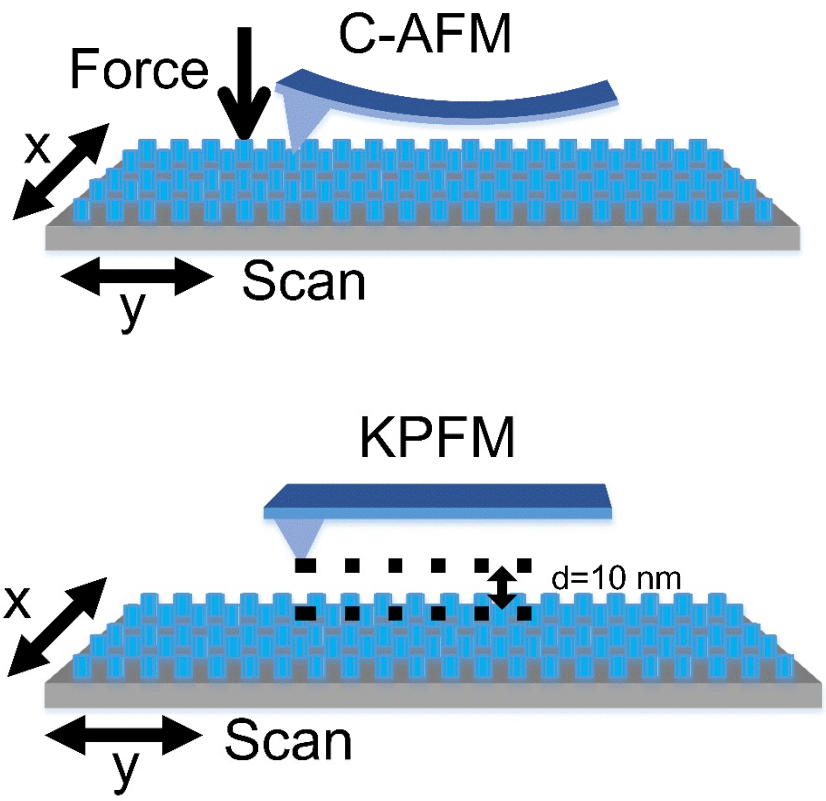
C-AFM
Force
x
Scan
y
KPFM
d=10 nm
x
Scan
y

(b)

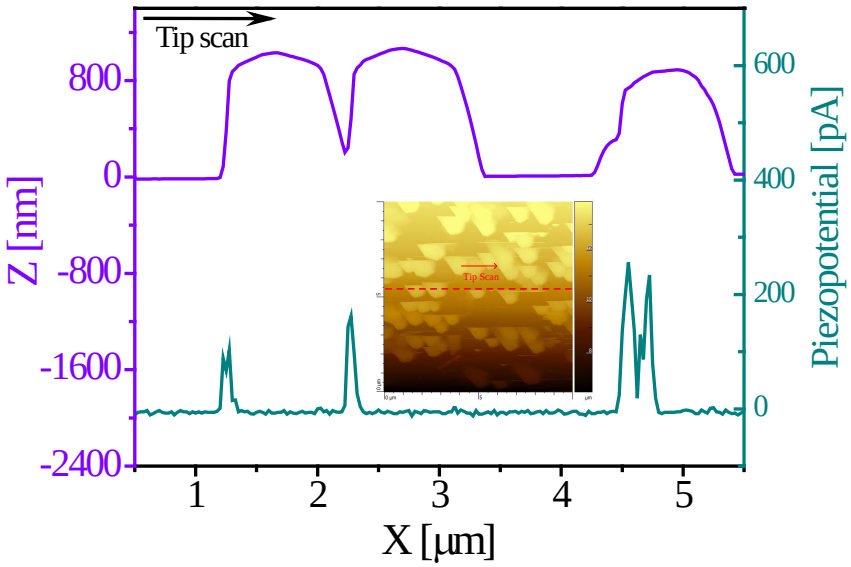
Tip scan
800
0
-800
-1600
-2400
Z [nm]
600
400
200
0
Piezopotential [pA]
1
2
3
4
5
X [μm]
Tip Scan

(c)

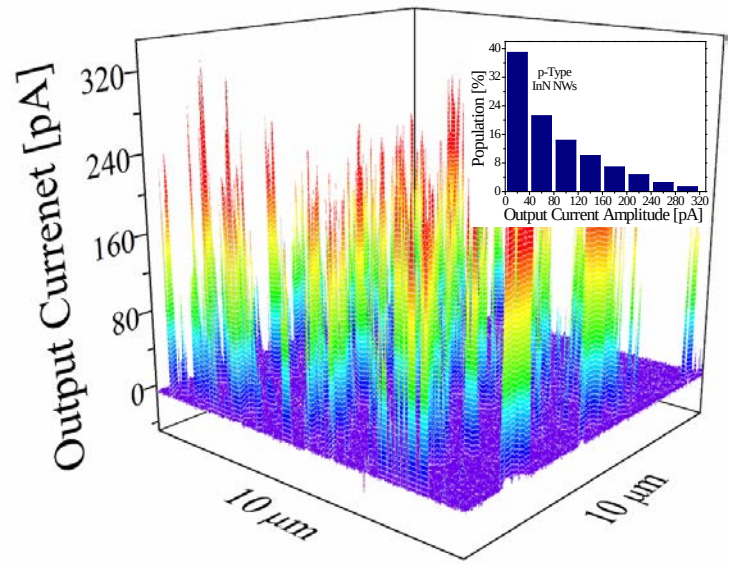

(d)

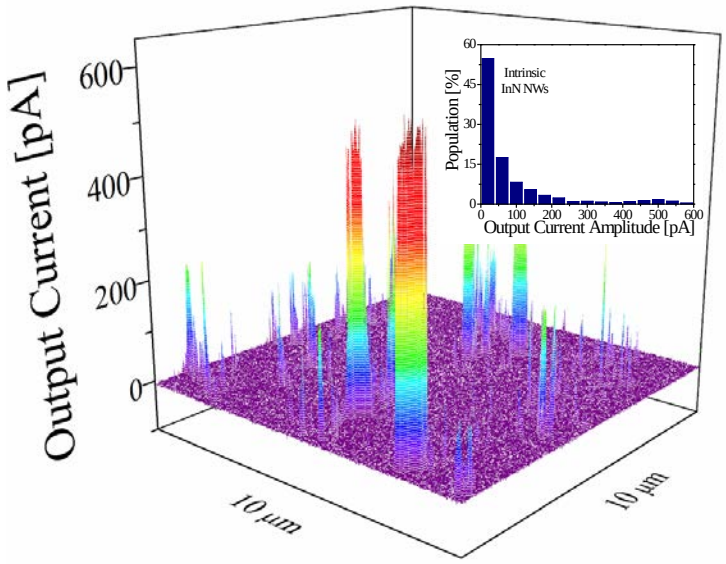

FIGURE 3.3 Piezoelectric characteristics of InN NWs. (a) Schematic illustration of the experimental setup of C-AFM and KPFM scans. (b) Line profiles of the topography and output current of *p*-type InN NWs; the inset is an AFM image of the surface; (c) *p*-type and (d) intrinsic InN NWs' current output signals for a C-AFM of 10 μm × 10 μm area with a scan speed of 10 μm/s under a constant normal force of 66.7 nN; the insets are the statistical distribution of the output current.

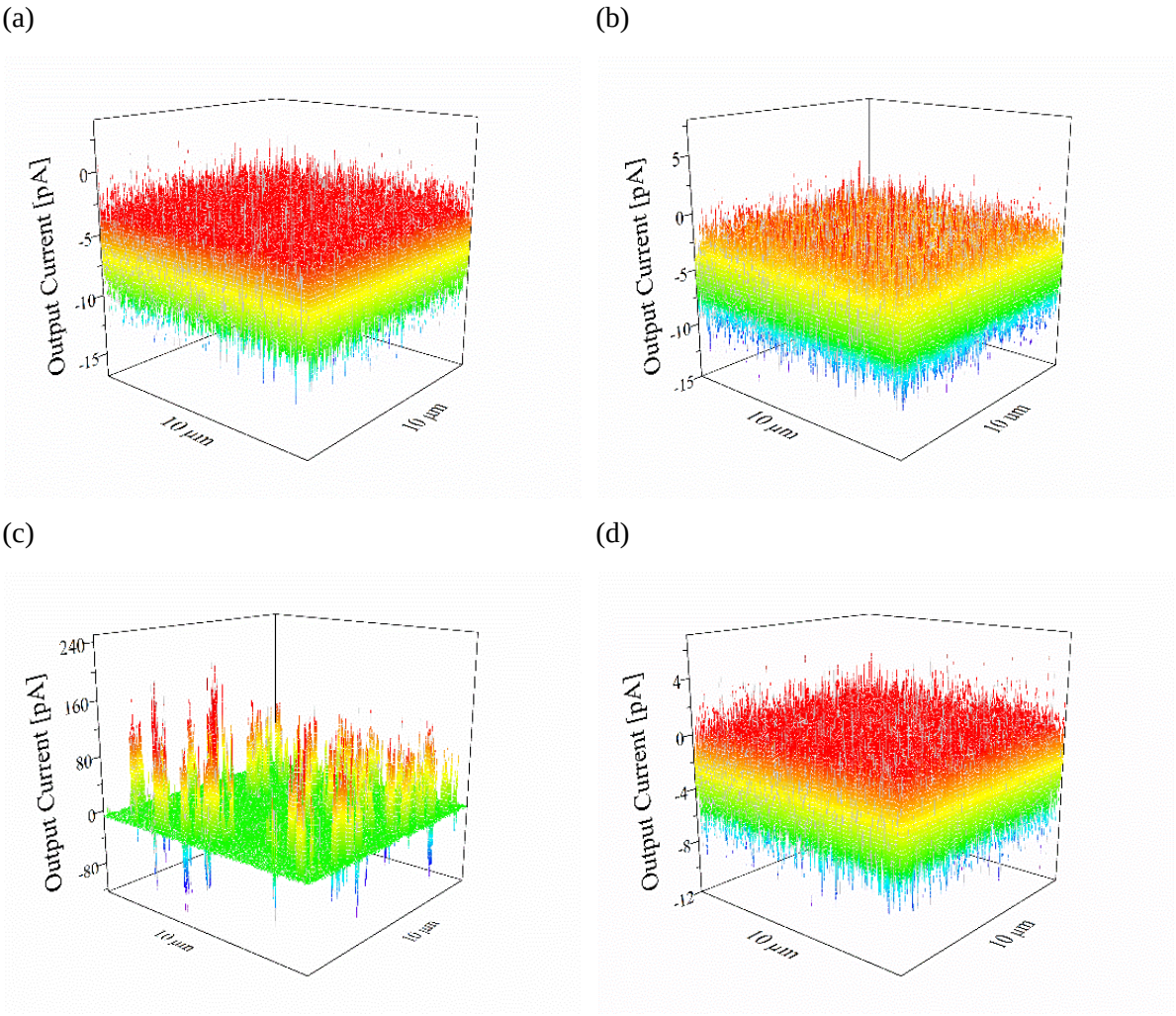

FIGURE S3.2 3D positive and negative current output signals when scanning over an area of 10 μm×10 um for (a) Si substrate, (b) doped and (c) intrinsic GaN NWs with Pt tip and (d) *p*-type InN NWs with a Si tip.

Assuming negligible capacitance, the NW output current I_s can be written as [135]:

$$I_s \approx V_s / (r_0 + r_c) \tag{3.1}$$

where V_s is the piezopotential generated by mechanical strain, r_0 is the resistance of the NWs, including the surface depletion effect [136], r_c is the contact resistance of the metal-semiconductor interface [137]. The large output current fluctuations for intrinsic NWs may indicate more diversified interface and surface effects.

A series of C-AFM scans were performed on the *p*-InN NWs under identical experimental conditions apart from progressive changes in the compressive force applied to the AFM probe. The average piezoelectric current was roughly proportional to the applied force, as expected (**Figure 3.4a**). At a force of 83 nN, the average piezoelectric current from the *p*-InN NWs is ~ 93 pA.

Figure 3.4b shows the electrical transport properties of InN NWs. The current-voltage (*I*-*V*) curves are obtained by engaging a conductive Pt/Ir AFM probe tip with individual NWs and using it as the top electrode. A compressive force of 66.7 nN is applied between the tip and the NW to establish and maintain a stable electric contact. The *I*-*V* measurements are performed by applying a bias to the AFM probe and sweeping the voltage. The curves (**Figure 3.4b**) show a clear asymmetric and rectifying behaviour, which can be ascribed to the Schottky contact formed between the Pt/Ir tip and InN NWs. The overall wire resistance ($r_c + r_0$) at 1.0 V is calculated as 14.2 MΩ for *p*-type and 13.0 MΩ for intrinsic NWs. By adding *p*-dopant, the actual free carrier density drops before the *n*-donors are completely compensated. As a result, *p*-type NWs resistance becomes higher. Morphology analysis (**Figure 3.1**) revealed that *p*-type InN NWs are longer and narrower than intrinsic NW, consistent with a higher NW resistance r_0 for *p*-type than for intrinsic NWs. An estimate of the voltage drop across individual NWs (V_s) can be found from Equation (3.1), by multiplying the measured NW current (I_s) by the overall NW resistance calculated from its *I*-*V* curve. Using this method, the ratio of V_s generated in intrinsic NWs to that generated in *p*-type NWs is found to be 1.03. Thus, the average piezoelectric properties of *p*-type and intrinsic InN NWs are similar.

To investigate the impact of Mg doping on the overall resistance of *p*-type InN NWs, transport behaviour across the interface between the NWs and the Pt/Ir AFM probe was modelled as a Schottky junction. This is described by the thermionic-emission-diffusion (*TED*) model [138].

$$I_{\mathrm{f}} = AA^{**}T^{2}\exp\left(-\frac{\phi_{\mathrm{B}}}{k_{\mathrm{B}}T}\right)\exp\left(\frac{qV_{\mathrm{f}}}{nk_{\mathrm{B}}T}-1\right)$$
$$V_{\mathrm{f}} = \sqrt{\frac{qE_{\mathrm{m}}}{4\pi\varepsilon_{\mathrm{s}}}}, E_{\mathrm{m}} = \sqrt{\frac{2qN}{\varepsilon_{\mathrm{s}}}\left(V + V_{\mathrm{bi}} - \frac{kT}{q}\right)} \quad (3.2)$$

where A is the area of the Schottky barrier, A^{**} is the effective Richardson constant, T is the temperature, ϕ_B is the Schottky barrier height (SBH), k_{B} is the Boltzmann constant, q is the electron charge, V_f is the voltage drop on the forward biased Schottky diode, N is the carrier concentration, and n is the ideality factor. The inset in Fig. 4b compares the experimental $lnI - V^{1/4}$ curve and the theoretical curve for *p*-type InN NWs. It shows excellent agreement between the model and experiment throughout the bias range.

(a)

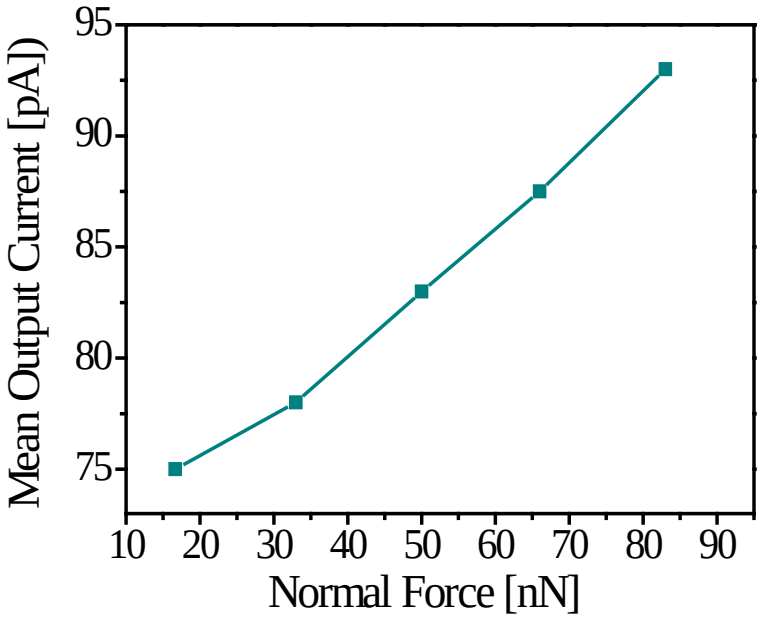

(b)

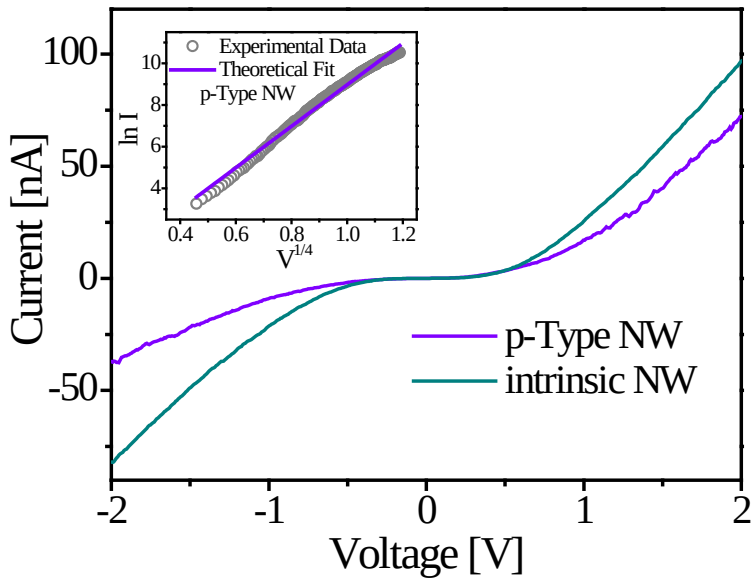

FIGURE 3.4 (a) Measured output current as a function of the compressive force applied to *p*-type InN NWs; (b) Measured *I-V* curves for *p*-type and intrinsic InN NWs. The inset compares the $ln\ I - V^{1/4}$ curves for the thermionic emission-diffusion model and the experimental results for *p*-type InN NWs.

The InN NWs samples were integrated into piezoelectric NGs (**Figure 3.5a**). The electric characteristics of NGs based on *p*-type and intrinsic InN NWs are next investigated. **Figure 3.5b** shows the measured *I*-*V* curves of the NGs. Similar to the *I*-*V* curves of individual NWs, they exhibit nonlinear characteristics, attributable to the Schottky-junction interface between the top electrode (Au/MoO_3 layer) and the InN semiconductor NWs. The *p*-type NG is more conductive than the intrinsic (*n*-doped) NG in both forward and reverse biases. The NGs' electric resistance at 1.0 V is calculated as R_i = 1 kΩ and 20 kΩ for *p*-type and intrinsic NGs, respectively. At 100 kHz, NG capacitances are measured as C_i = 0.589 and 0.582 nF, respectively (Figure S3.3). Although the *p*-type NG contains more high permittivity InN NWs than the intrinsic NG [139], it also has a larger capacitive gap due to the longer *p*-type NWs. As a result, they end up with similar capacitance.

Figure 3.6a and **b** present the piezoelectric response of the *p*-type NGs for open-circuit voltage (V_{oc}) and short-circuit current (I_{sc}) output, respectively. The NGs' substrate was anchored on a fixed stopper, leaving the top electrode facing outward and free standing. The shaker moved up and down, applying periodic strain to the NWs by striking the top electrode at the end of each cycle [140, 141]. The excitation frequency was set to 3 Hz, and the acceleration amplitude to 2 m/s^2. The NGs' response to individual mechanical strain cycles appears as a series of voltage or current spikes. The peak values of the output voltage and current exhibit reasonable consistency between pulses, with an average peak value of ~55 mV for V_{oc} and ~211 nA for I_{sc}. These values represent a potential maximum output power density of $(V_{oc} \times I_{sc})/A$ of ~0.012 μW/cm^2, given that the effective area (A) of *p*-type InN NGs is 0.81 cm^2. The inset shows the open-circuit voltage V_{oc} and short-circuit current I_{sc} during a single loading-unloading cycle. Impact bounce is observed in V_{oc} output during the loading cycle, as the shaker head bounces on the NG's top electrode surface. It is not observed in I_{sc} because of the increase in the effective damping level once the circuit is closed.

Switching polarity tests were conducted to verify that the measured signals came from the piezoelectric response of the NG devices rather than from electromagnetic interference noise or other artefacts (Figure S3.4c). Switching polarity changed the sign of the measured open-circuit voltage V_{oc} and short-circuit current I_{sc}, but not their magnitudes or wave forms. The same experiments were performed on control devices with a layer structure similar to that of the NG devices but no InN NW layer. They showed no appreciable voltage or current spikes (Figure S3.4d), confirming that the electric signals from the NGs result from the InN NWs' piezoelectric response.

The *p*-type and intrinsic NGs were tested under the same experimental conditions to compare their performance. At a fixed external excitation with an acceleration amplitude of 2 m/s^2 and a frequency of 3 Hz, both NGs yielded substantial piezoelectric response (**Figure 3.6c**); nevertheless, their output

differed greatly. The *p*-type NG's short-circuit current is 2.63 times that of the intrinsic NG, but it has a lower open-circuit voltage of 0.055 V compared to 0.085 V for the intrinsic NG. Table I shows that the power product of V_{oc} and I_{sc} of the *p*-type NG is 70% higher than that of the intrinsic NG.

The long-term stability of the InN nanowire-based NGs was next investigated. The *p*-type NG was tested for 1050 consecutive cycles. Strain was applied by an external excitation with an acceleration amplitude of 2 m/s^2 and a frequency of 3 Hz, and the open-circuit and short-circuit current were recorded. The results, shown in **Figure 3.6d**, are fairly consistent over the entire test span.

(a)

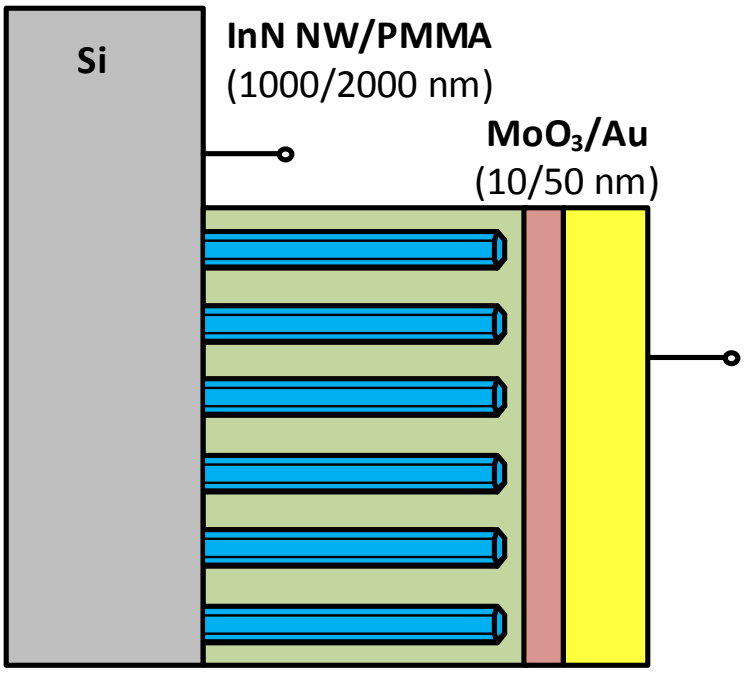

(b)

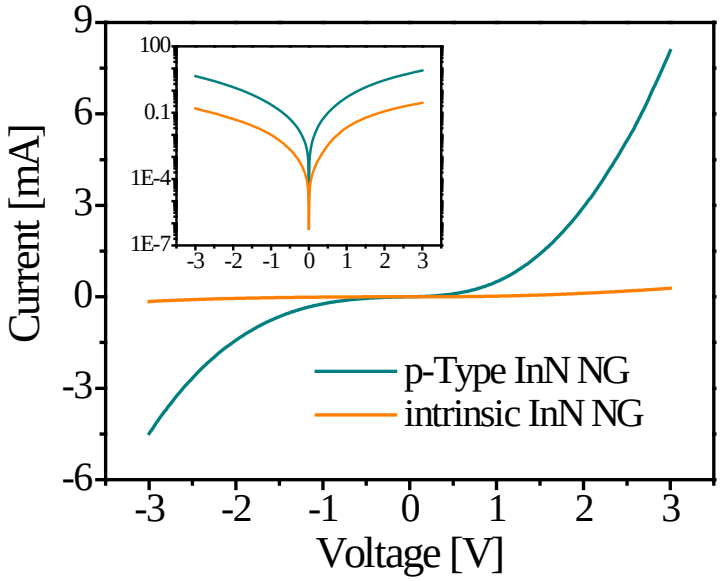

FIGURE 3.5 (a) Schematic diagram of the InN NW-based NG. (b) The measured current-voltage curves of the *p*-type and intrinsic NGs at room temperature. The inset shows the Log_{10} *I-V* curves for the NGs.

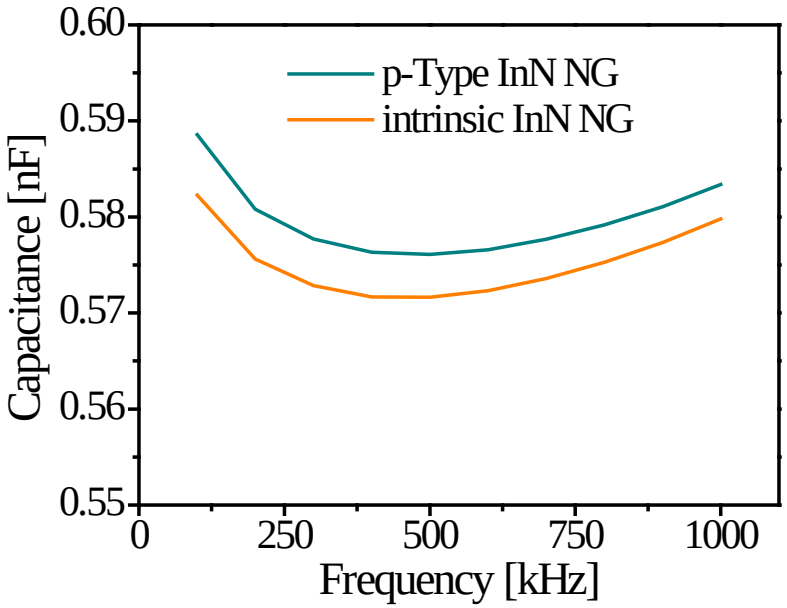

FIGURE S3.3 shows the capacitance-frequency response of InN NG device investigated by using Keithley 4200-SCS semiconductor characterization system that is carefully calibrated before measurements with the suppression of the noise down to 1fF in a wide frequency range.

(a)

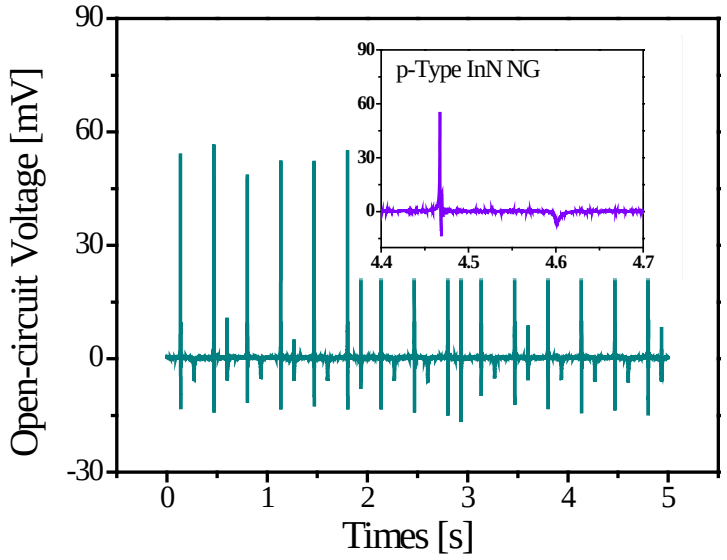
Open-circuit Voltage [mV]
Times [s]
p-Type InN NG

(b)

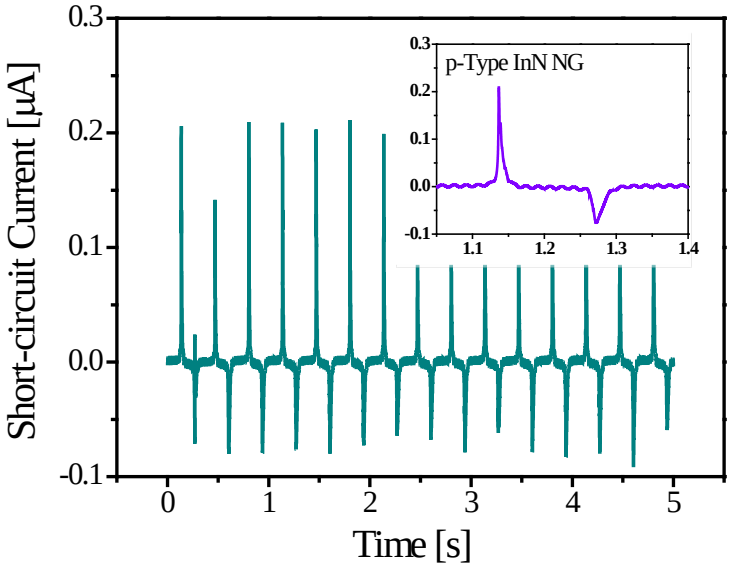
Short-circuit Current [μA]
Time [s]
p-Type InN NG

(c)

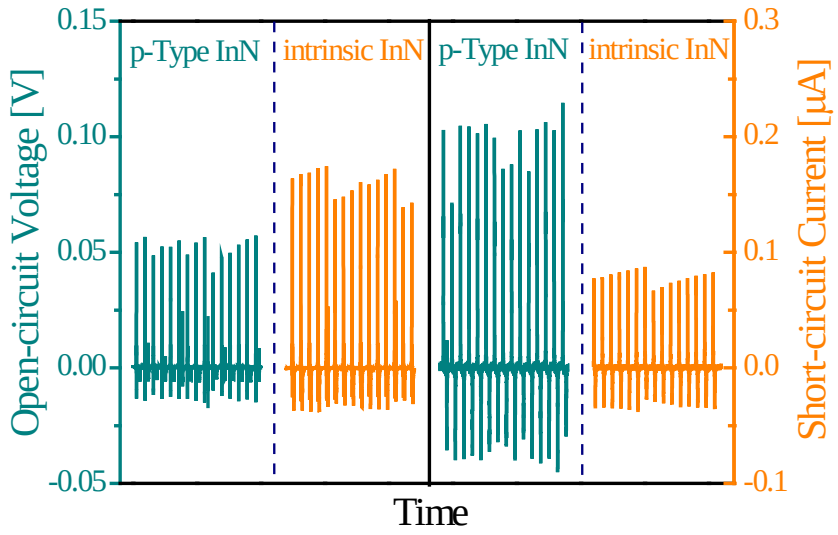

(d)

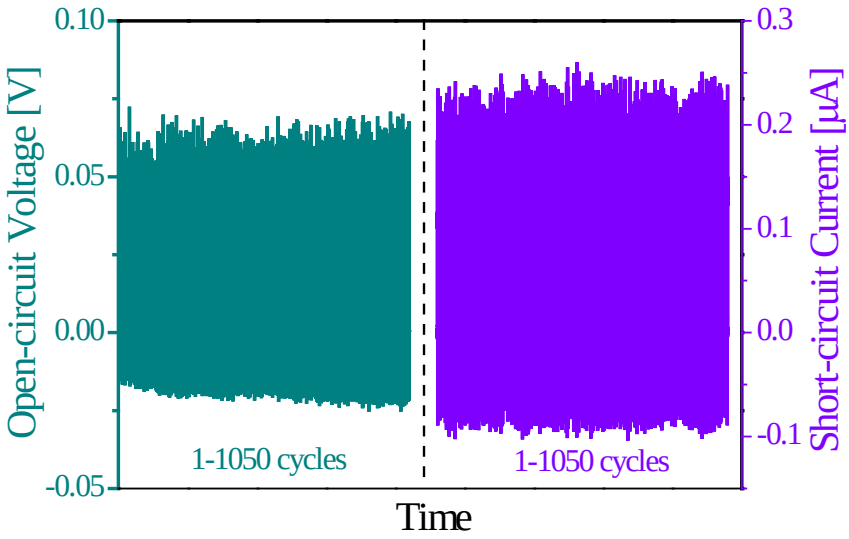

FIGURE 3.6 Piezoelectric characteristics of InN NGs. Comparison of *p*-type and intrinsic InN NGs' performance at an excitation with an acceleration amplitude of 2 m/s^2 and a frequency of 3 Hz. The measured (a) open-circuit voltage, an average peak value of ~0.055 V, and (b) short-circuit current, an average peak value of 211 nA, for *p*-type NGs. The insets show signals from one cycle of mechanical vibration. (c) The measured open-circuit voltage and short-circuit current of *p*-type and intrinsic NGs. (d) Long-term open-circuit voltage V_{oc} and short-circuit current I_{sc} recorded over 1050 excitation cycles.

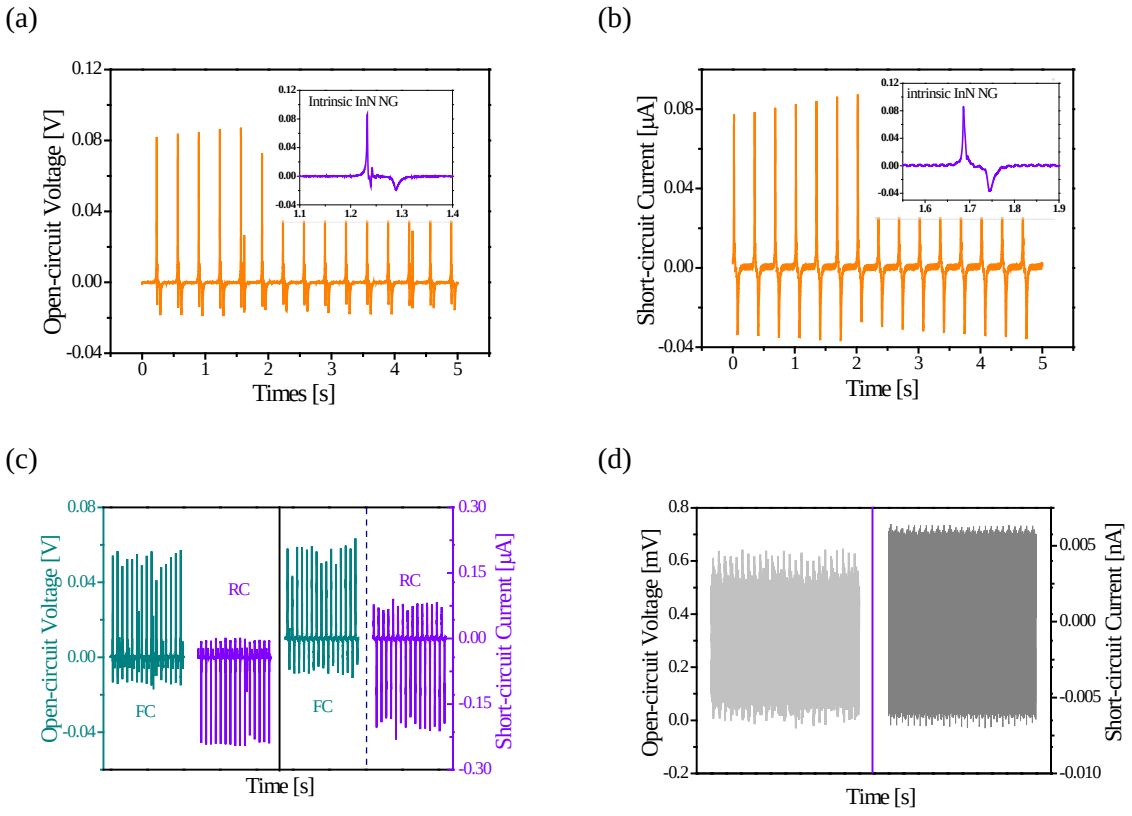

FIGURE S3.4 The piezoelectric characteristics of the NGs at an excitation with an acceleration amplitude of 2 m/s^2 and a frequency of 3 Hz. The measured (a) open-circuit voltage, an average peak value of ~0.085 V, and (b) short-circuit current, an average peak value of 80 nA, for intrinsic-type. The insets show signals from one cycle of mechanical vibration. (c) The measured open-circuit voltage and short-circuit current of the *p*-type NG under the forward and reversed connection conditions. (d) The measured open-circuit voltage and short-circuit current of the Si/PMMA/MoO_3/Au film.

3.4 Discussion

3.4.1 Use of Doping to Improve NW Piezopotential

The NGs' working mechanism is based on coupled piezoelectric and semiconducting properties. Once stress is applied to the top electrode, the piezoelectric effect creates fixed charges close to the NWs' end surfaces, resulting in a macroscopic potential across the length of the NWs. An important limitation of piezoelectric semiconductor NWs is that holes and free electrons present in the NWs can greatly reduce the piezopotential via a screening effect [14]. To investigate this effect in InN NWs, the piezopotential profile inside NWs with different doping concentrations was simulated using the TiberCAD multiscale simulation tool [104, 105]. For simplicity, the simulations were restricted to

steady-state conditions under thermal equilibrium, at a temperature of 300 K. **Figure 3.7a** and **b** show the potential along *p*-type and intrinsic (*n*-type) InN NWs when subjected to a compressive force of 100 nN. Clearly, the higher the carrier concentration, the lower the magnitude of the piezopotential, thus the more pronounced the piezoelectric screening due to free carriers, a finding consistent with results for individual ZnO NWs [103-105]. Therefore, it is possible to use low concentration *p*-type doping to balance the free electrons in intrinsic InN NWs, thereby reducing or eliminating the screening effect and increasing the piezopotential of *p*-type InN NWs beyond that realized in intrinsic InN NWs.

In our experiments, it was found that the average piezopotential of *p*-type and intrinsic InN NWs were similar, as shown in **Figure 3.3c** and **d**. This might be attributed to the fact that the effective free charge carrier density in the *p*-type NWs (estimated in the range of 2×10^{15} to 6×10^{15} cm^{-3} [130]) is somehow comparable to that in the intrinsic NWs (effective *n*-type concentration of ~ 4×10^{15} cm^{-3} [124]).

3.4.2 Scattering Spreading Inconsistency

Although the observed maximum piezoelectric current from the intrinsic NWs (601 pA) is much higher than that of the *p*-type NWs (331 pA), on average their piezoelectric current from NW ensembles over an area of 100 μm^2 is comparable, i.e., 101.8 ± 127 pA for intrinsic NWs and 90.7 ± 70.6 pA for *p*-type NWs, (the insets of **Figure 3.3c** and **d**). Furthermore, the piezoelectric current from the intrinsic NWs exhibits a much larger scattering than the *p*-type NWs (127 pA vs. 70.6 pA). The observed higher maximum piezoelectric current suggests that the intrinsic NWs could potentially be a better candidate for NG application. Nevertheless, the larger divergence in the piezoelectric current yields a poorer overall device performance for intrinsic InN-based NGs comparing to the *p*-type NGs. The observed larger divergence from intrinsic InN NWs may be related to their higher vulnerability to unstable surface states.

InN surfaces are known to possess a high concentration of donor-type surface states, resulting in an electron accumulation layer [109, 142, 143], which may lead to an elevated surface potential. Using non-contact KPFM, the electrical potential difference between the conductive probe tip and the sample surface provides a measure of the NWs' surface potentials. **Figure 3.8a** and **b** show the topography and surface potential measured along a line during a raster scan of 10×10 μm^2 of *p*-type and 25×25 μm^2 of intrinsic InN NWs, respectively. The *p*-type NWs show a potential difference of up to -160 mV (scan area average -141 ± 11 mV) between the NW and its surroundings. For intrinsic NWs, the potential difference is higher, reaching a maximum of -290 mV (scan area average - 236 ± 26 mV). These measurements were repeated from 10 separate images. While some variability was observed in the

measured surface potential, they all show that the *p*-type NWs' surface potential difference is much lower than intrinsic NWs. We propose that the elevated surface potential of intrinsic NWs increases the instability of their surface states and, therefore, the variability of their piezoelectric properties.

(a)

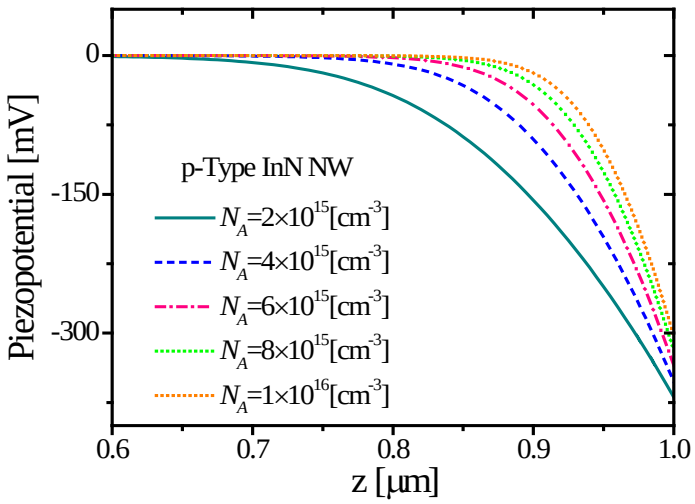

(b)

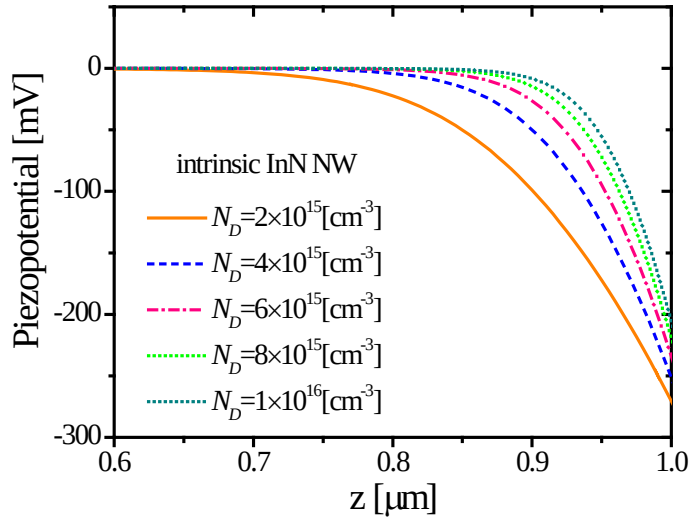

FIGURE 3.7 Calculated piezopotential in (a) *p*-type and (b) intrinsic (*n*-type) InN NW (D = 200 nm and L = 1.0 μm) surrounded by free space and subject to a compressive force of 100 nN.

(a)

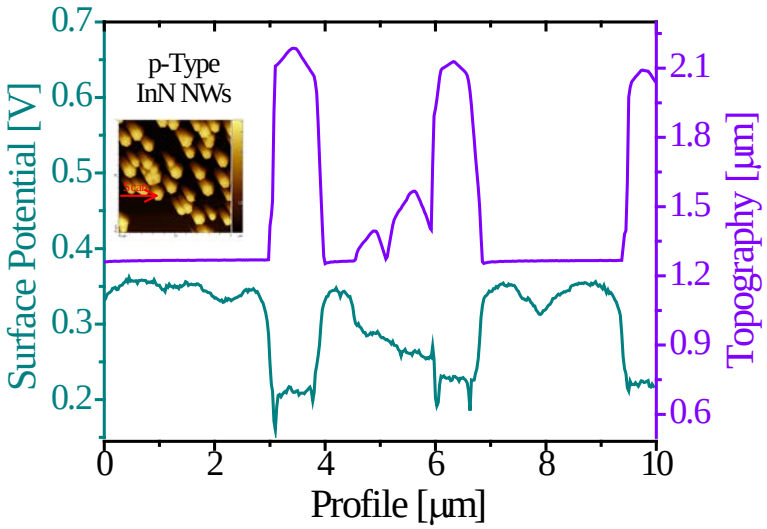

(b)

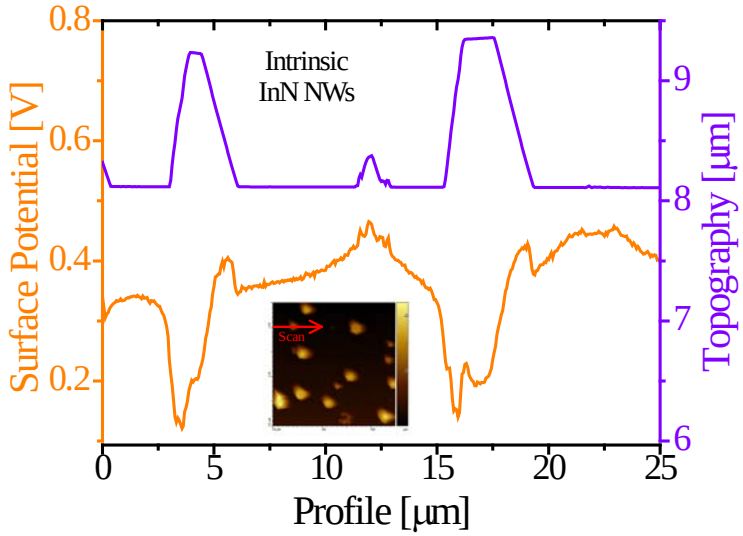

FIGURE 3.8 Surface potential (bottom) and topography (top) profiles during a line scan of (a) *p*-Type; (b) intrinsic InN NWs.

TABLE 3.1 Comparison of *p*-type and intrinsic NGs' performance

	V_{oc} [V]	I_{sc} [uA]	$V_{oc} \times I_{sc}$ [nW]	R_i @ 1V [Ω]	C_i @ 100 kHz [nF]
p-type	0.055	0.211	11.6	1 k	0.589
intrinsic	0.085	0.08	6.8	20 k	0.582

3.4.3 NG Performance

To analyse the performance of the NGs, we note that their output current may be approximated as

$$I = \frac{V}{|Z|} \tag{3.3}$$

where V is the voltage drop across the NG electrodes, and $|Z|$ is the magnitude of its total internal impedance. Since the NGs' inductance is negligible, impedance Z consists of a resistive component $Z_r = R_i$ and a capacitive component $Z_c = (i\omega C_i)^{-1}$ connected in parallel, where ω is the angular frequency [17]. Therefore, the magnitude of the total internal impedance is

$$|Z| = \frac{R_i}{\sqrt{1 + (R_i \omega C_i)^2}} \tag{3.4}$$

Calculating the electric resistance at 1 V from Fig. 3b, measuring the capacitance at 100 kHz (**Table 3.1**), and using Equation (3.4), the impedance ratio of the intrinsic to *p*-type NGs is ~2.89. Assuming similar piezoelectric performance for the *p*-type and intrinsic NGs would suggest a similar open-circuit voltage ratio. The measured ratio of the intrinsic to the *p*-type NGs' open-circuit voltage V_{oc} is 1.55. The lower V_{oc} ratio reflects better piezoelectric conversion efficiency of *p*-type NGs due to the smaller diameter of *p*-type NWs compared to intrinsic NWs [139].

Similarly, Equation (3.3) suggests that the short-circuit current of a *p*-type NG should be 2.89 times that of the intrinsic NG. The actual ratio of the short-circuit current is 2.64 (**Table 3.1**), which is in fair agreement with the estimated value. The driving factor in the significant difference between *p*-type and intrinsic NGs' impedance and short-circuit current is the lower electrostatic losses in *p*-type NGs due to longer NWs and a higher fill ratio β_p.

3.5 Conclusion

In this chapter, we have successfully fabricated the first piezoelectric NGs based on InN NWs. Raman spectroscopy, XRD, C-AFM, and KPFM were used to characterize each of the *p*-type and intrinsic InN NWs. The statistical distribution of their piezopotential, when compressed by an AFM tip, was also measured. While intrinsic NWs demonstrate the possibility for a much higher piezoelectric response than *p*-type NWs, the prospect is undermined by their highly scattered and inconsistent responses across the array. On the other hand, even though *p*-type NWs have lower peak piezopotential than intrinsic NWs, their consistent response results in their average piezoelectric performance being similar to that of intrinsic NW arrays.

We propose that the variability in intrinsic NWs' response is due to their having a greater surface potential difference than *p*-type NWs. This suggests that the surface passivation of intrinsic NWs may improve their performance. On the other hand, the piezopotential of *p*-type NWs can be significantly improved beyond that realized here by lowing the *p*-type carrier concentration to reduce the free carriers in the NWs and their detrimental screening effect.

The power product of *p*-type NGs was 70% more, at 11.6 nW, than the power product of intrinsic NGs. Both types of NGs had an area of 0.81 cm^2 and were excited by an acceleration amplitude of 2 m/s^2 and frequency of 3 Hz. The *p*-type NGs had 160% more short-circuit output current, at I_{sc} = 211 nA, than intrinsic NGs. The higher output power of the *p*-type reflects a better piezoelectric energy conversion efficiency than intrinsic NGs, due to a smaller NW diameter. The higher output current of *p*-type NGs reflects a much lower impedance enabled by the lower electrostatic losses of *p*-type NGs due to increased NW areal density and longer NWs.

Chapter 4
Flexible p-n Homojunction ZnO Nanowire Arrays for Energy Harvesting

4.1 Motivation

Piezoelectric nanogenerators (NGs) have proven effective in harvesting mechanical energy from ambient environments and converting it to electrical energy [90, 144]. They provide a clean inexhaustible power source for self-powered electronics, such as environmental monitoring sensors, structural health monitoring sensors, portable health electronics, and other wearable electronics [91]. ZnO nanowires (NWs) are promising piezoelectric materials for such devices due to their chemical stability, mechanical robustness, environmental and biological compatibility, and abundance[114, 145].

The performance of piezoelectric NGs depends not only on their piezoelectric coefficient, but also on their ability to suppress the screening effect of mobile charge carriers [146]. Undoped ZnO NWs are typically n-type semiconductors with a high density of electrons [147]. Mobile electrons can completely shield the strain-induced piezoelectric potential in NWs from being measured externally. Several approaches have been demonstrated to overcome this fundamental constraint, including surface oxygen plasma treatment [7], triboelectric layer insertion [148], and p-n junction formation [13-15, 18, 149, 150]. In p-n junction schemes, the carrier density is significantly reduced by a depleted region formed at a heterojunction between the NWs (n-type) and a p-type material. One such heterojunction combined ZnO nanorods with the p-type semiconducting polymer PEDOT:PSS and successfully demonstrated kinetic-to-electric energy conversion [13].

Nevertheless, the material properties of added hetero-material, such as less mechanical robustness, inferior chemical stability, and unmatched thermal expansion coefficients, may adversely affect the overall NG performance and raise uncertainties about long-term device reliability. With some materials, such as PEDOT:PSS, precisely controlling the doping concentration is difficult. A more desirable approach reported recently involves fabricating NGs with ZnO p-n homojunction NWs [25]. Similar NWs are already in use for many other applications [68, 151-158].

This chapter systematically investigates flexible NGs made of patterned ZnO homojunction NWs with different p-doping concentrations, grown using consecutive electrochemical deposition. Optical/electrical characterizations and second-ion mass spectroscopy (SIMS) are used to confirm the formation of ZnO nanowire-based homojunctions. We find that properly controlling the doping concentration of the p-doped section of the NWs improves NG performance eleven-fold.

4.2 Nanowire Growth and Characterization

The NWs were grown using electrochemical deposition in a three-electrode configuration, with a platinum mesh counter electrode and an Ag/AgCl reference electrode [159, 160]. An aluminum-doped ZnO (AZO, 2 wt.% Al_2O_3 + 98 wt.% ZnO) layer was coated onto a pre-cleaned polyethylene naphthalate (PEN) substrate using radio-frequency (RF) magnetron sputtering at 150 °C. The AZO layer serves as both the conductive electrode and seed layer for NW growth in the subsequent electrochemical deposition. Photolithography was then employed to open an array of square windows, 200 µm apart, in a photoresist layer spun onto the AZO-coated PEN substrate. The retained photoresist mask ensures that NWs grow only on the exposed seed layer in the open windows. The solution for growing intrinsic NWs (n-type) comprises 25 mM zinc nitrate ($Zn(NO_3)_2$), 12.5 mM hexamethylenetetramine (HMTA), 5 mM polyethylenemine (PEI), and 0.3 M ammonium hydroxide. To obtain p-type NWs (Li-doped), different concentrations of a lithium nitrate doping reagent were added. These concentrations (25 mM, 50 mM, and 75 mM) corresponded to different lithium mixture ratios (100%, 200%, and 300%, respectively) and produced differently Li-doped NWs. The working electrode's bias was fixed at -0.7 V with respect to the Ag/AgCl reference electrode. The NW length (~4 µm) was simply controlled by setting the growth time to 3 hours for the intrinsic section (n-type) immediately followed by another 3 hours for the Li-doped section (p-type). The solution temperature was maintained at 90 °C for 10 minutes followed by 88 °C for 170 minutes in both cases.

A series of p-n homojunction NW patterns with different p-doping concentrations of 0%, 100%, 200% and 300% (hereafter dubbed respectively samples A, B, C, and D) was prepared, then cleaned using a standard process. The top-view SEM images (Figure S4.1) show that NW morphology is consistent across all four samples. **Figure 4.1a** shows a photograph of an array of patterned ZnO NWs grown on a transparent and flexible PEN substrate. The square patterns side lengths vary from 600µm to 1.4 mm. For greater piezoelectric output, square patterns with side lengths of up to 5 cm were fabricated on subsequent substrates. The purpose of patterning is to exclude environmental interference and to provide a basis for effective comparison of output for a range of NGs. The position-controlled synthesis of ZnO NWs occurred only in designated areas. This approach improves not only the NWs' effectiveness in energy harvesting, but also the NGs' defect toleration because each unit can work independently [131].

The morphology of a 300 nm thick AZO layer was characterized using tapping-mode atomic force microscopy (Veeco Dimensions V SPM) in a surface area of 5 × 5 μm^2 (bottom-right inset, **Figure 4.1b**). The layer's root-mean-square (RMS) roughness was 4.9 nm. Such high uniformity is crucial for obtaining high quality ZnO p-n homojunction NWs. Morphologic and crystalline structural information

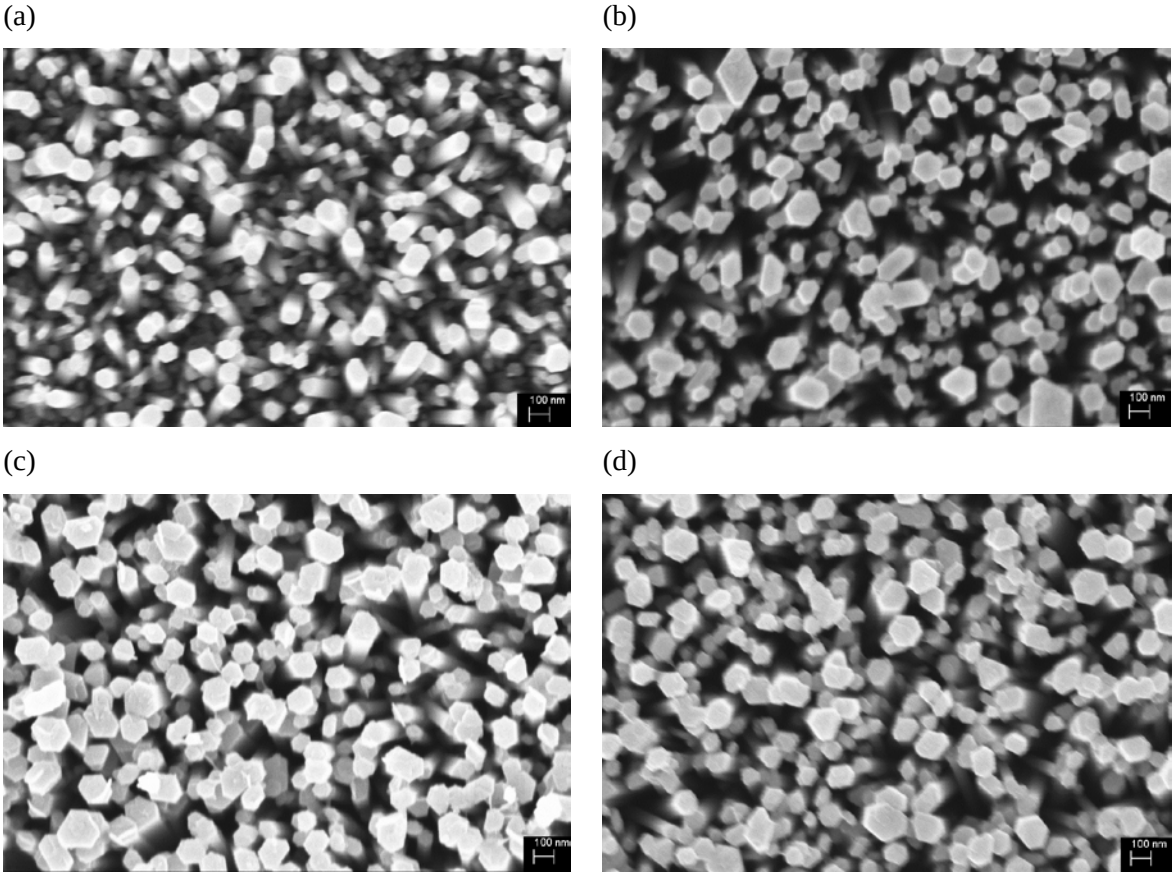

FIGURE S4.1. Top-view SEM images of ZnO homojunctions NWs on AZO with (a) 0% Li-doping (sample A); (b) 100% Li-doping (sample B); (c) 200% Li-doping (sample C); (d) 300% Li-doping (sample D)

about the as-grown ZnO NWs was obtained using a field-emission scanning electron microscope (FE-SEM, Zeiss) and high resolution X-ray diffraction (XRD) system (Jordan Valley QC3). The photoluminescence (PL) spectra of NWs with different Li doping concentrations were measured at room temperature under optical excitation ($\lambda = 325\ nm$) triggered by a He-Cd laser source. Secondary ion mass spectroscopy (SIMS, ION-ToF GmbH ToF-SIMS IV) confirmed that the growth process had achieved NWs with the desired Li-doping concentration variation.

Figure 4.1b shows a cross-sectional scanning electron microscopy (SEM) image of one of the NW p-n homojunction samples. The single-crystalline NWs are roughly aligned along the vertical direction having tilting angles within ±25°. Their diameters range from 100 nm to 200 nm. The inset of **Figure 4.1b** (top-right) shows a top-view SEM image of the NWs, whose area density is about 2.0×10^9 cm^{-2}.

The formation of shorter wires is primarily caused by the size-dependent growth of seed nanocrystals. Smaller crystals grow at a much lower rate than larger ones, especially at higher temperatures [161]. Clear spaces/gaps occur between individual NWs, allowing polymethyl methacrylate (PMMA) to surround and encapsulate them. The consistently high crystalline quality of the ZnO NWs among the four samples is confirmed by the consistent shift of the XRD peak at 34.2° ± 0.2° (Figure S4.2).

The photoluminescence (PL) spectra of the four ZnO NW samples was measured at room temperature (**Figure 4.1c**). All spectra show a narrow emission peak at ~380 nm (3.27 eV), attributed to near-bandedge (NBE) radiative recombination, and a broad emission peak at ~590 nm (2.1 eV), related to radiative recombination associated with deep-level impurities and defects. As expected, the relative intensity of the impurity/defect-related emission peak (~590 nm) with respect to that of the NBE emission peak (~380 nm) is lowest in sample A. The residual impurity/defect-related emissions can be attributed to the deep levels associated with the OH- radical group incorporated in the crystal lattices [162]. Adding lithium nitrate to the solution ensured lithium ions were incorporated in the crystal lattice and induced further defects in it. As a result, the relative intensity of the peak at ~590 nm is substantially enhanced in the other three samples (B, C and D), because of the additional impurities associated with substitutional Li (Li_{Zn}) and interstitial Li (Li_i) ions [163, 164] incorporated in the crystal lattice and related defects. The three PL spectra in **Figure 4.1c** show that the relative intensity of the impurity/defect-related emission peak decreases with increasing lithium mixture ratios, probably because of excessive incorporation of Li ions, resulting from the high lithium nitrate concentration. The excessive impurities would shorten the non-radiative recombination lifetime, suppressing the optical intensity of the PL emission (radiative recombination). Similar results have been reported in [165, 166].

The PL results clearly show that the NW's optical properties are considerably modified, as Li ions are incorporated into the crystal lattices. The elevated relative fraction of impurity/defect emission among in the doped samples may imply elevated levels of free carriers' population in the doped samples. The Li ion density depends on the lithium nitrate mixture ratio in the growth solution, with higher ratios yielding a higher Li dopant concentration, as confirmed by SIMS results (Figure S4.3).

(a)

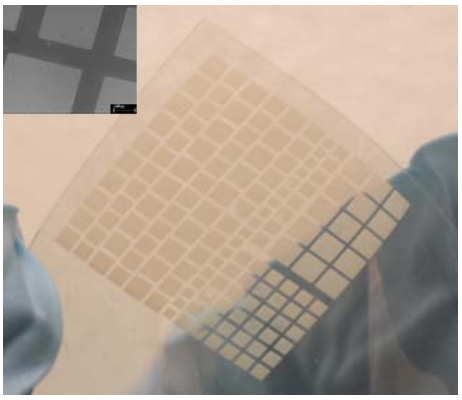

(b)

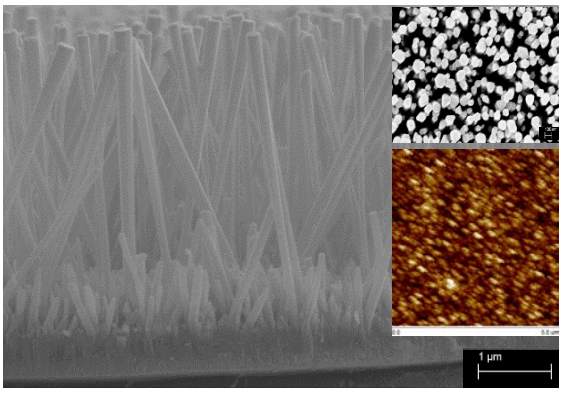

(c)

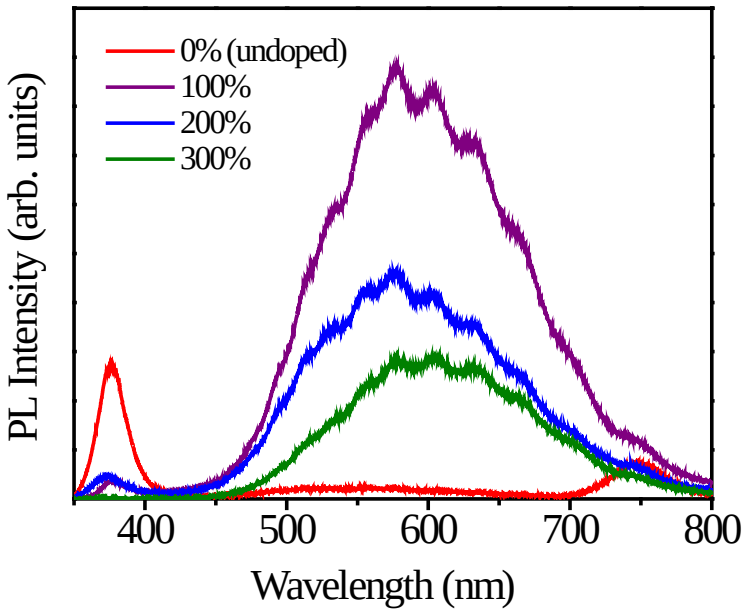

FIGURE 4.1 Topological and optical characteristics of ZnO p-n homojunction nanowires (NWs). (a) A photograph of patterned NW arrays deposited on a flexible PEN substrate. The inset shows the gap between neighboring NW patterns is 200 µm. (b) Tilted cross-sectional view of a field-emission scanning electron microscope (FE-SEM) image of NWs on the PEN substrate The insets are a top-view FE SEM image (top-right) of the NWs and an atomic force microscope (AFM) image of an Al-doped ZnO seed layer with a thickness of 300 nm, showing the layer topography. (c) Photoluminescence (PL) spectra of p-n homojunction NWs.

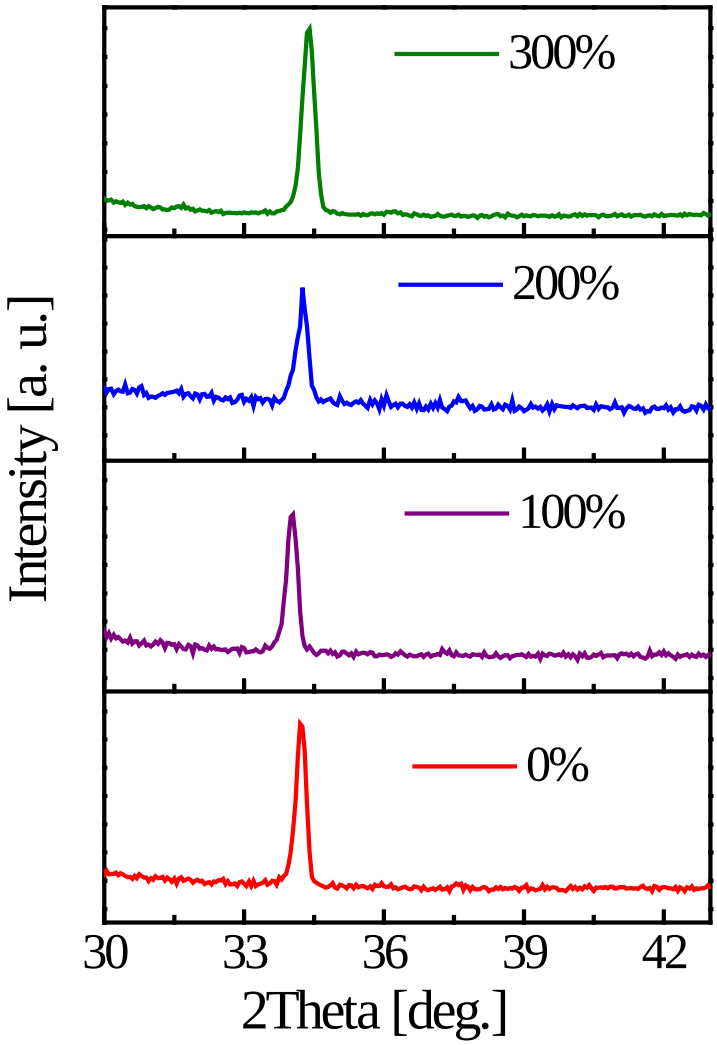

FIGURE S4.2. The x-ray diffraction (XRD) 2θ scan patterns of the un-doped and Li-doped ZnO NW arrays grown on 300 nm AZO seed layer with PEN substrates. The narrow and consistent diffraction peaks reflect the high crystalline quality of the NWs.

(a)

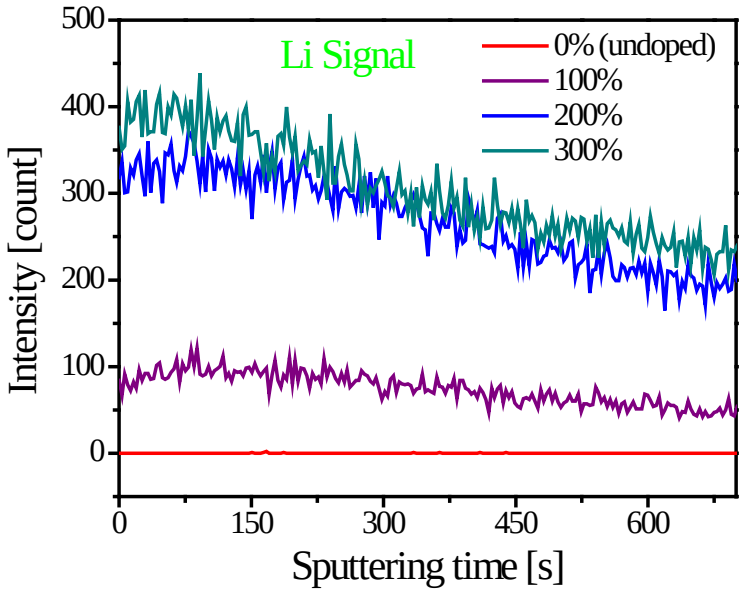

(b)

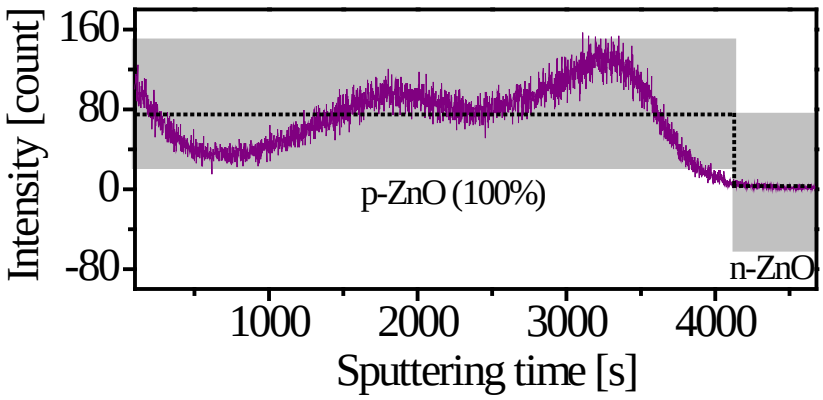

FIGURE S4.3. (a) The second ion mass spectroscopy (SIMS) depth profiles of the Li-doped p-n ZnO p-n homojunction NWs (100%, 200%, 300%) and intrinsic ZnO NWs (0%). The SIMS depth profiles for the different concentrations of Li-doped NWs confirm the incorporation of Li ions in the crystal lattice of NWs. It shows that the incorporated Li dopant concentration is higher when the NWs are grown with a higher lithium nitrate mixture ratio. (b) The SIMS depth profile of a ZnO p-n homojunction NW sample (100%). It clearly shows the transition region from the Li-doped segment (0 - ~3500s) to intrinsic segment (~4200 s and beyond).

4.3 Nanogenerator Fabrication and Characterization

NW patterns with a side length of 1.2 cm were used to fabricate the A, B, C, and D families of NGs (Figure S4.4), which respectively incorporate NW samples A, B,C, and D, hereafter dubbed NGs A, B, C and D. The NWs were first encapsulated with a spin-coated insulating layer of PMMA, then cured at 120 °C for 3 hours. This layer provides a polymer matrix to protect NWs against damage during NG operation and prevents electrical shortage between the NGs' top and the bottom electrodes.[11] Due to its flexibility, PMMA does not impede the application of external strain to the NWs [131]. To increase the interfacial energy barrier and supress leakage current [165], a thin molybdenum oxide (MoO_3) interlayer was deposited on top of the PMMA layer by vacuum thermal evaporation using a shadow mask, followed by the deposition of a 70 nm thick aluminum (Al) cathode to complete fabrication (**Figure 4.2a**). The thickness of this interlayer was set to 10 nm for all NGs except for NGs C, where the layer thickness was varied from 0 to 20 nm in steps of 5 nm. Silver paste was used to glue a Cu wire lead on the bottom AZO electrode and another on the top Al electrode. The devices were packaged in polydimethylsiloxane (PDMS), Dow Corning Sylgard 184 premixed with curing agent at a ratio of 10:1 w/w and degassed, to prevent contamination, damage, and moisture penetration from the ambient environment.

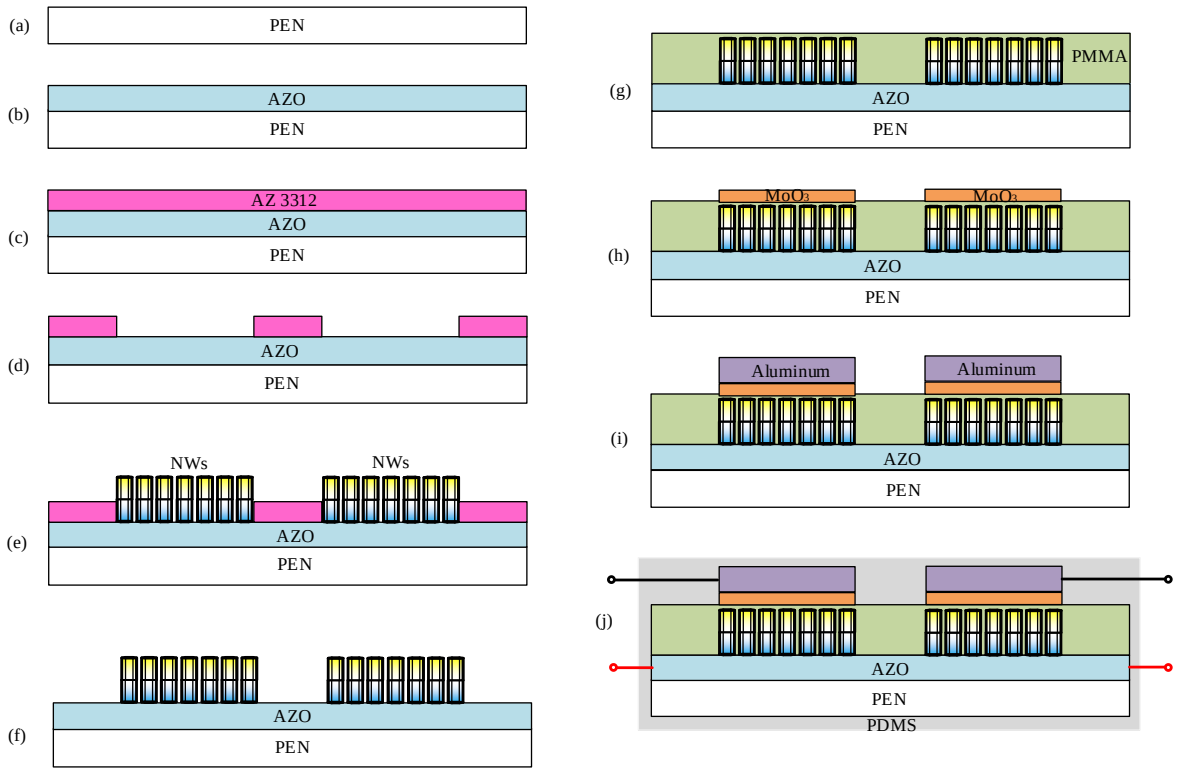

FIGURE S4.4 Schematic representation of the NG fabrication process. (a) PEN substrate. (b) Deposition of an AZO seed layer by RF sputtering. (c) Photoresist spin-coating. (d) Windows opening by photolithography. (e) Selection growth of ZnO p-n homojunction NWs. (f) Stripping off residual photoresist by acetone. (g) Spin-coating a PMMA layer to cover the structure. (h) Deposition of a MoO3 layer. (i) Deposition of a metal layer as the top electrode. (j) Packing by PDMS.

The current-voltage (*I-V*) curves of the NGs and their junction capacitance were measured using a Keithley 4200-SCS semiconductor characterization system calibrated before measurements so as to lower the system noise down to 1fF in a wide frequency range (1kHz ~ 10MHz). **Figure 4.2b** shows the *I-V* curves for NGs A, B, C, and D. The current-voltage relationship shows evidence of a cubic nonlinearity, attributable to the combined effects of the interfaces between electrode metals and ZnO semiconductor nanowires and the p-n homojunction inside the nanowires. The different p-doping concentrations significantly affect the *I-V* characteristics, with conductivity dropping as the doping concentration increases. The electric resistance at 1.0 V is 15 kΩ, 60 kΩ, and 1 MΩ for NGs B, C, and D, respectively. NGs A, with no doping, were the most resistive for forward and reverse biases. As the p-doping concentration increases, the depletion region width of the p-n junction decreases and thus the corresponding junction capacitance increases. Indeed, capacitance measured at 100 kHz, was 0.13, 0.66, and 0.76 nF for NGs B, C and D, respectively (**Figure 4.2c**). However, the higher p-doping concentration results in higher wide-gap insulator LiO_2 defects [167], which increases NWs resistivity. Additionally, by adding p-dopant, the actual free carrier density drops before the n-donors are completely compensated. As a result, NWs resistance becomes higher [167].

NG piezoelectric characterization was carried out using a system that included a close loop controller (Vibration Research Corporation, VR9500) and a linear shaker (Labworks Inc., ET-126B-1), to provide sinusoidal waves simulating a vibration source with a known amplitude. Output voltage and current signals were measured using Stanford low-noise voltage/current preamplifiers (Model SR560/570) and a National Instruments I/O module (NI CompactDAQ USB-9239). The input resistances of the preamplifiers were 100 MΩ (SR560) and 10 kΩ (SR570), respectively. To minimize electromagnetic interference, the two copper wires connected to the device under test were twisted together. All measurements occurred at ambient room temperature.

(a)

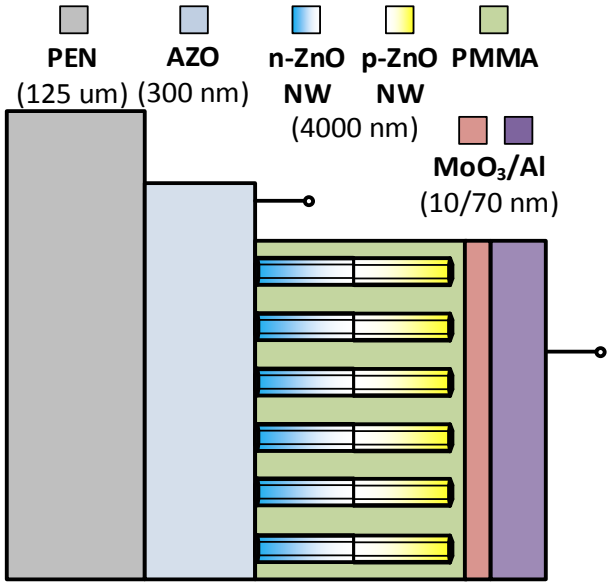
PEN
(125 um)
AZO
(300 nm)
n-ZnO
NW
p-ZnO
NW
(4000 nm)
PMMA
MoO3/Al
(10/70 nm)

(b)

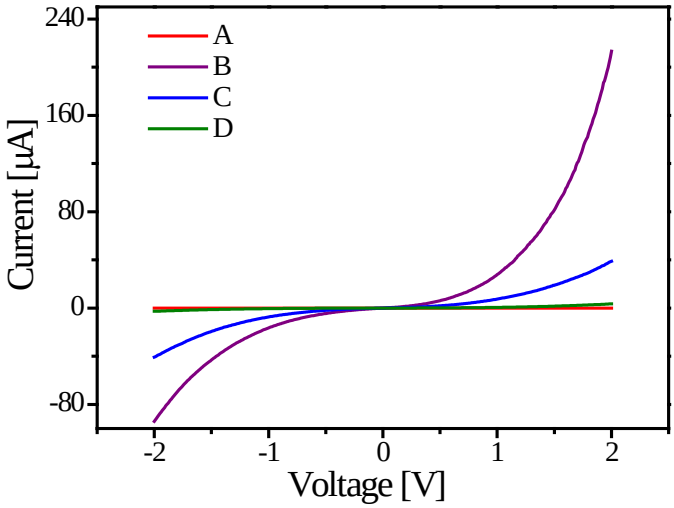
240
160
80
0
-80
Current [μA]
A
B
C
D
-2
-1
0
1
2
Voltage [V]

(c)

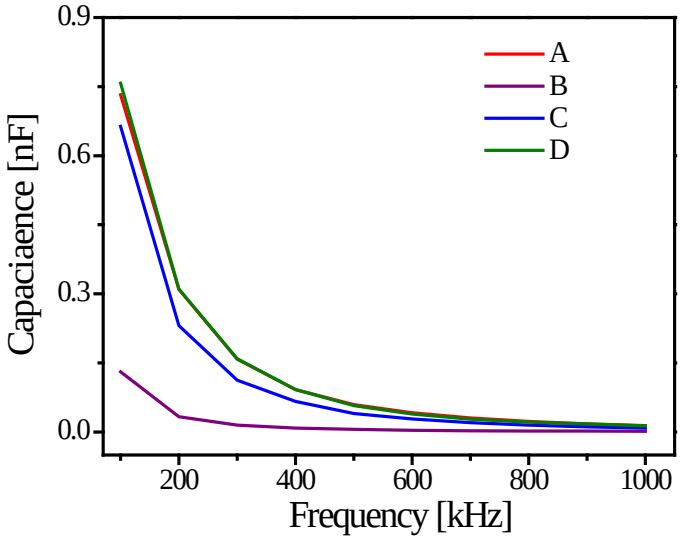

FIGURE 4.2 (a) A schematic diagram of a fabricated nanogenerator (NG) made of the p-n homojunction ZnO NWs. (b) The measured current-voltage curves of the NGs. The thickness of the interfacial MoO_3 layer in the devices was 10 nm. (c) The measured capacitance-frequency response of the NGs.

The NGs' substrate was anchored to a fixed stopper, leaving the top electrode facing outward and standing free. The shaker moved up and down, applying periodic strain to the NWs by striking the NGs, at the end of each cycle (Figure S4.5) [165]. Its excitation frequency was set to $f = 3$ Hz, and peak-to-peak displacement was set to $d = 5$ mm, corresponding to 0.9 m/s^2 peak acceleration, using

$$a = 2(\pi f)^2 d \sin(2\pi ft) \tag{4.1}$$

The piezoelectric response to individual mechanical strain cycles appears as a series of voltage or current spikes. **Figures 4.3a** and 4.**3b** show open-circuit voltage (V_{oc}) and short-circuit current (I_{sc}) output, respectively, for NGs B. The peak value of the output voltage/current is consistent between pulses, with an average peak value of $V_{oc} \approx 0.7$ V and $I_{sc} \approx 40$ nA. Interestingly, the open-circuit voltage ($V_{oc} \approx 0.3$ V) is substantially lower during unloading than during loading (compression) ($V_{oc} \approx 0.7$ V). A similar pattern is observed in the short-circuit current. The insets of **Figures 4.3a** and **b** zoom in on a single response pulse; the response time is on the order of a few milliseconds, much less than that in GaN NW devices [146].

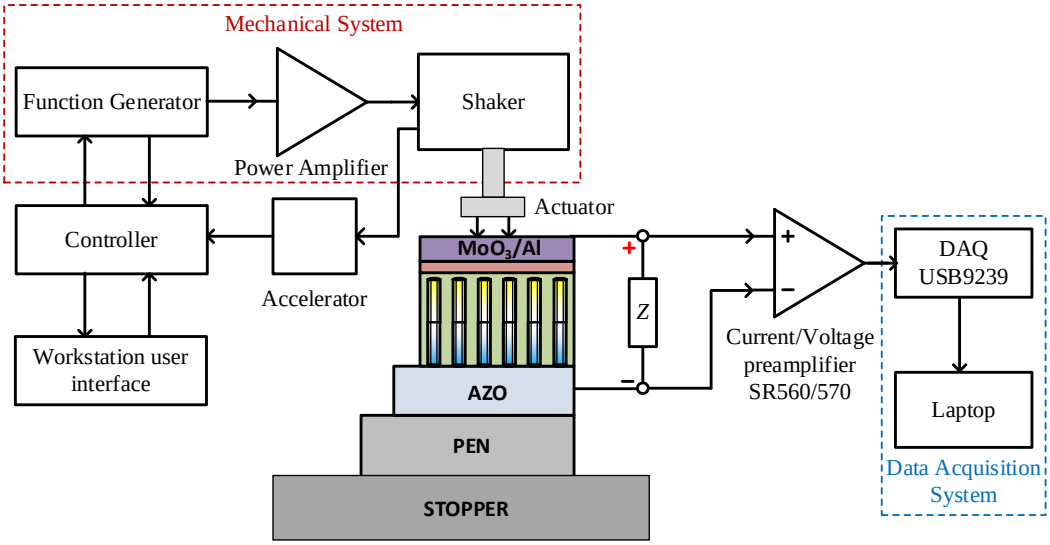

FIGURE S4.5 The schematic setup for measuring the output current/voltage of fabricated p-n ZnO homojunction NGs. A system includes a close loop controller (Vibration Research Corporation, VR9500) and a linear shaker (Labworks Inc., ET-126B-1). The shaker provided sinusoidal waves simulating a vibration source with a known amplitude. Output voltage and current signals were measured using Stanford low-noise voltage/current preamplifiers (Model SR560/570) and a National Instruments I/O module (NI CompactDAQ USB-9239). The input resistances of the preamplifiers were 100 MΩ (SR560) and 10 kΩ (SR570), respectively.

(a)

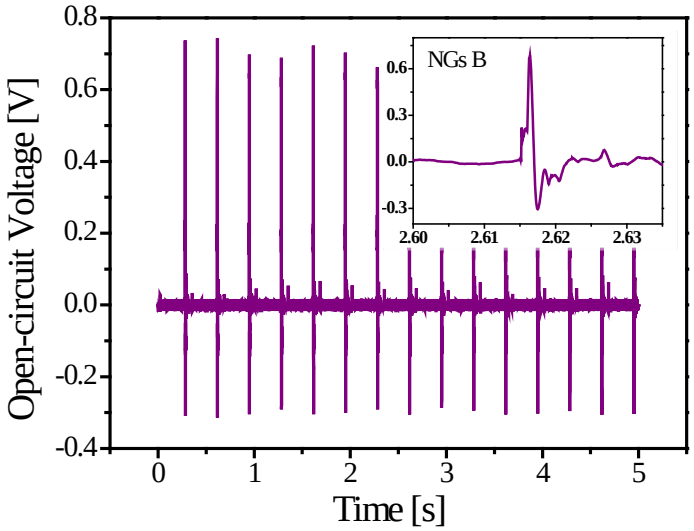

(b)

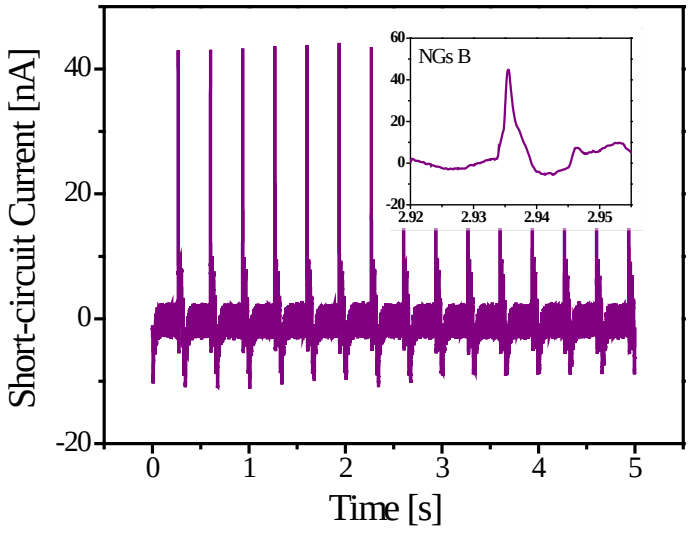

FIGURE 4.3 (a) Measured open-circuit voltage (average peak value ~0.70 V) and (b) short-circuit current (average peak value 42 nA) for NGs B. The insets are enlarged signals from one cycle of excitations at a frequency of 3 Hz. The peak-to-peak displacement was kept constant at 5 mm.

The energy harvesting mechanism exploits the piezopotential generated in the NWs under compressive loads to drive charge back and forth between the AZO and Al electrodes. When a compressive force is applied to the ZnO NWs (Figure S4.6a), it generates a negative piezopotential (V-) at the p-ZnO/PMMA interface and a positive piezopotential (V+) at the AZO/n-ZnO interface, which drives electron to flow from the Al electrode to the AZO electrode through an external load resistor. The result is a positive voltage and current pulse. A higher built-in field or a wider depletion region in the homogeneous junction can slow the carriers' drift velocity and suppress the screening rate, leading to a higher voltage drop between the electrodes [13]. Owing to the high interfacial energy barrier, the electrons keep accumulating at the interface between AZO and n-ZnO until the potential they create balances the piezopotential in an equilibrium state (Figure S4.6b). Once the compressive load is released, the piezopotential fades, and the electrons around the AZO electrode flow back to the Al electrode via the external circuit. Consequently a negative pulse is generated, and the system returns to its initial equilibrium state (Figure S4.6c and d). As the device is released, the interfacial barrier height prevents electrons from diffusing into the n-ZnO section, likewise the carriers from the p-section of the NW are prohibited from passing through the p-ZnO/PMMA interface due to the strong interfacial energy barrier between PMMA and MoO_3 [14].

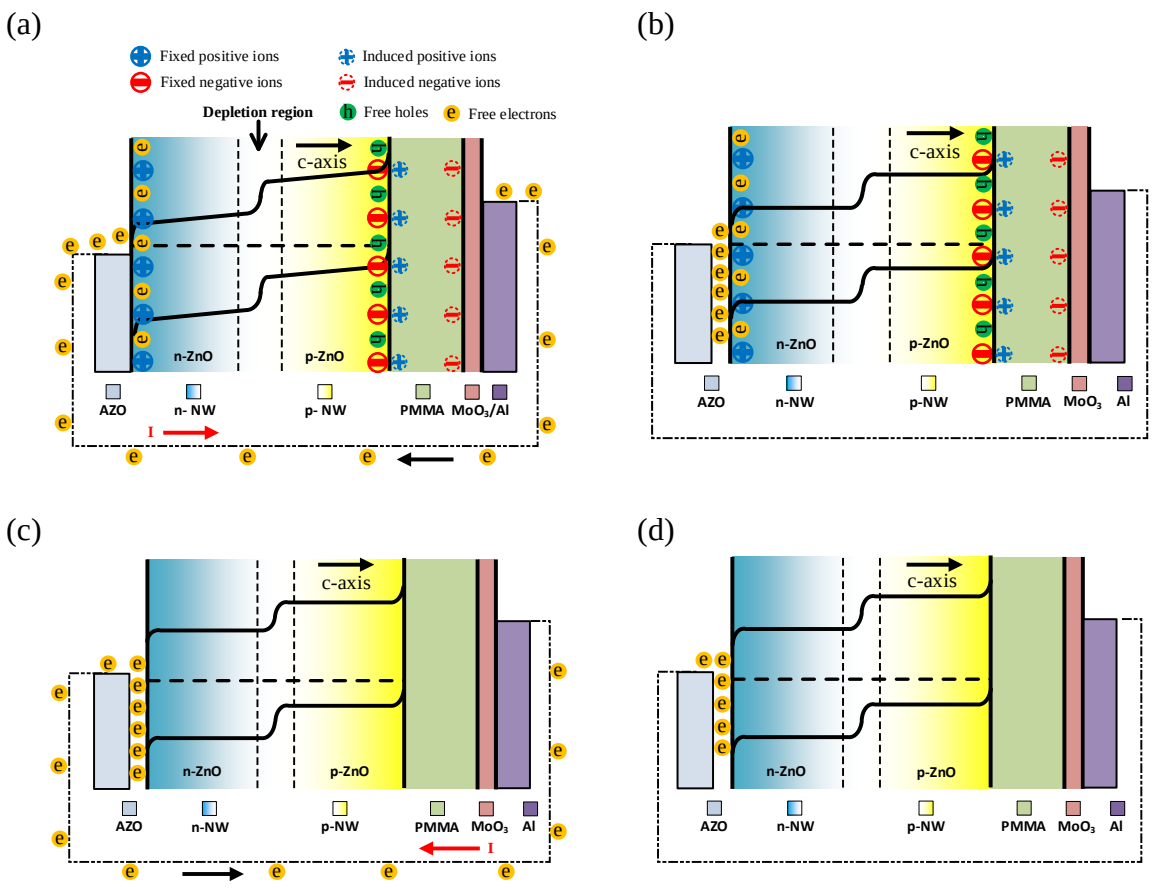

FIGURE S4.6. Energy band diagram of a ZnO p-n homojunction NG. a) Compression force is applied; b) An equilibrium state is achieved when the electric field induced by mobile charges offsets the piezopotential. Full screening of the positive polarization by the electrons. c) Once the force is released, the piezoelectric potential fades away instantly, and the electrons around the aluminum-doped ZnO (AZO) electrode flow back to the Al electrode via the external circuit, consequently a negative pulse is generated and the system returns back to its initial state. d) Finally, some electrons are blocked and remain at both AZO and Al electrodes. Some carriers from the p-NWs are prohibited from passing through the p-NWs/PMMA interface due to the strong interfacial energy barrier between PMMA and MoO_3.

The asymmetry in the voltage/current waveform between the pulse corresponding to loading and that corresponding to unloading is due to the viscoelasticity of the NGs' PMMA matrix [168]. Viscoelastic materials are hysteretic. They follow an unloading path different from that they follow during loading, which dissipates some of the elastic potential energy absorbed during loading. As a result, the output power of the unloading stage is less than that of the loading stage.

Switched polarity tests were conducted on NGs B to verify that the signals measured represent true NG energy harvesting, not electromagnetic interference noise or other artifacts (Figure S4.7a, b). The output voltage and current were found to be 0.6 V and ~35 nA for excitation with a frequency of 5 Hz and an acceleration amplitude of 2 m/s^2. The same experiments were also performed on control devices #1, which were identical to NGs B except that they contained no NWs. They showed no appreciable voltage/current spikes (Figure S4.8), confirming the piezoelectric origins of the signals obtained from NGs B.

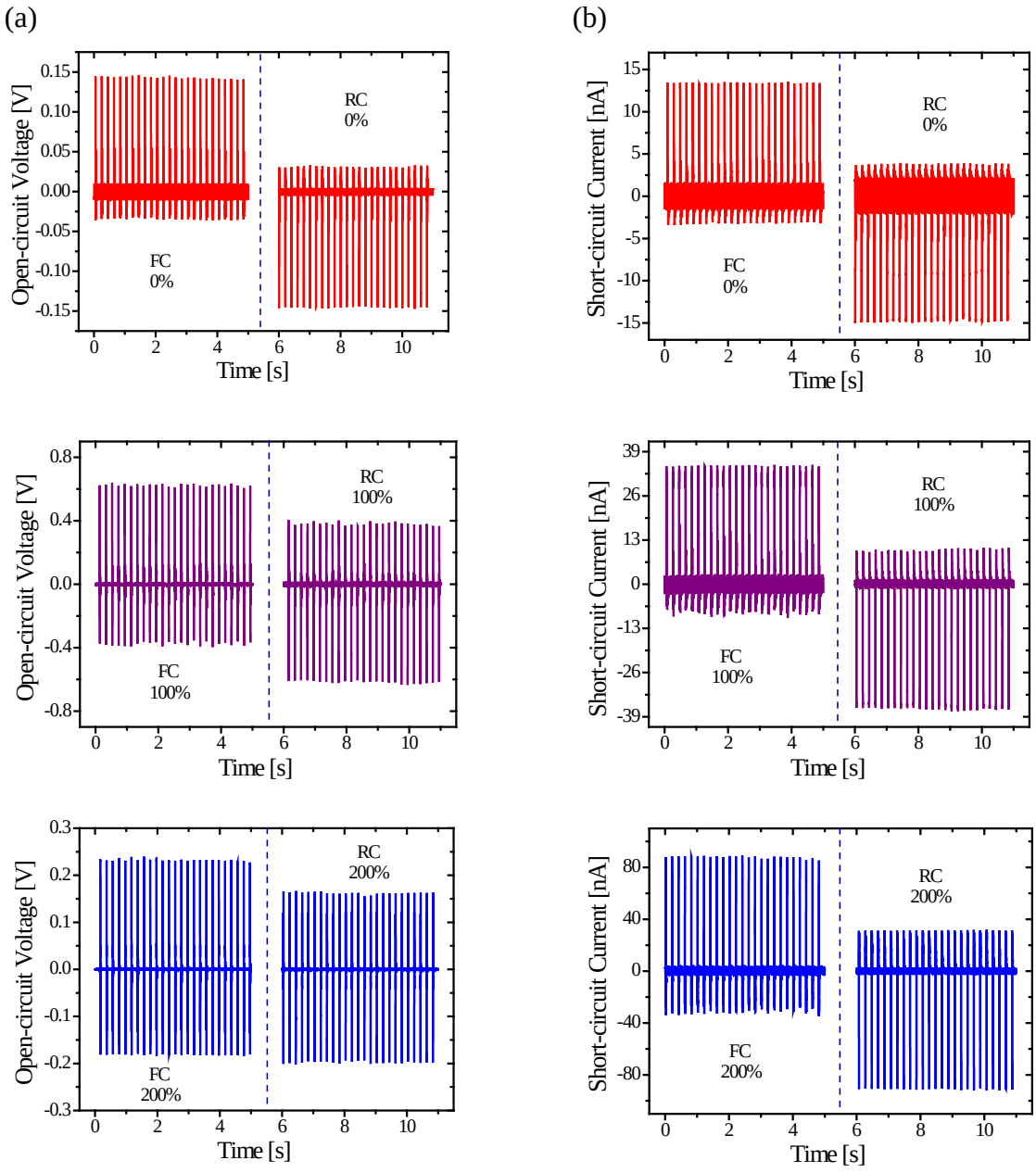

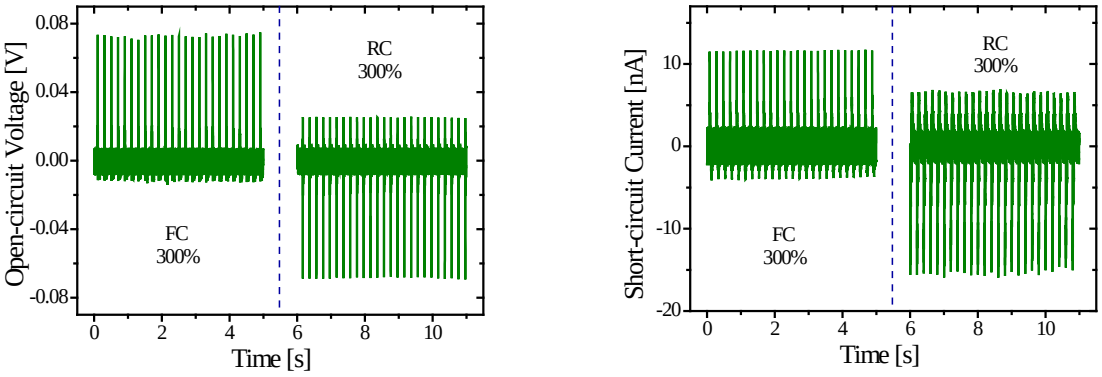

FIGURE S4.7 a) Measured open-circuit voltage and b) short-circuit current of NGs, under forward (FC) and reversed (RC) connection conditions under excitation of peak acceleration of 2 m/s^2 at a frequency of 5 Hz.

Other control devices, #2, were fabricated identical to NGs B apart from the deposition of a 200 nm-thick silicon nitride (SiN) insulating layer on the NWs before they were spin coated with PMMA. The encasement of the NWs with a hard coat of SiN (Young's modulus = 250 GPa) drastically reduces the strains they experience under loading, therefore retarding piezoelectric energy harvesting. The open-circuit voltage and short-circuit current of this device are 0.05 V and ~10 nA, respectively, under an excitation of 2 m/s^2 acceleration amplitude at a frequency of 5 Hz (Figure S4.9), significantly lower than the corresponding values (0.6 V and ~35 nA) of NGs B under the same conditions. The experimental results thus unambiguously confirm the effective use of a ZnO nanowire p-n homojunction NG in harvesting mechanical vibration energy.

NGs A, B, C, and D were tested under an excitation with an acceleration amplitude of 2 m/s^2 at a frequency of 5 Hz to investigate the effect of p-doping on device performance. In **Figures 4.4a** and **b**, the open-circuit voltage and short-circuit current of all four NGs show substantial piezoelectric response, but differ markedly in output level. NGs B perform best in terms of open-circuit voltage, with a peak value (0.63 V) 4.5 times that of NGs A. NGs C have the highest short-circuit current (92 nA), more than six times that of NGs A (15.05 nA). Overall, NGs D perform the worst, with a short-circuit current of 15.6 nA (slightly higher than NGs A) but a much lower open-circuit voltage of 0.07 V (only half that of NGs A). Clearly, doping concentration plays an important role in tuning the piezoelectric characteristics of p-n homojunction NWs. **Table 4.1** summarizes those results showing that proper doping concentration can enhance the power product ($V_{oc} \times I_{sc}$) capability by 1102%. However, NG performance can be substantially degraded with lithium over-doping.

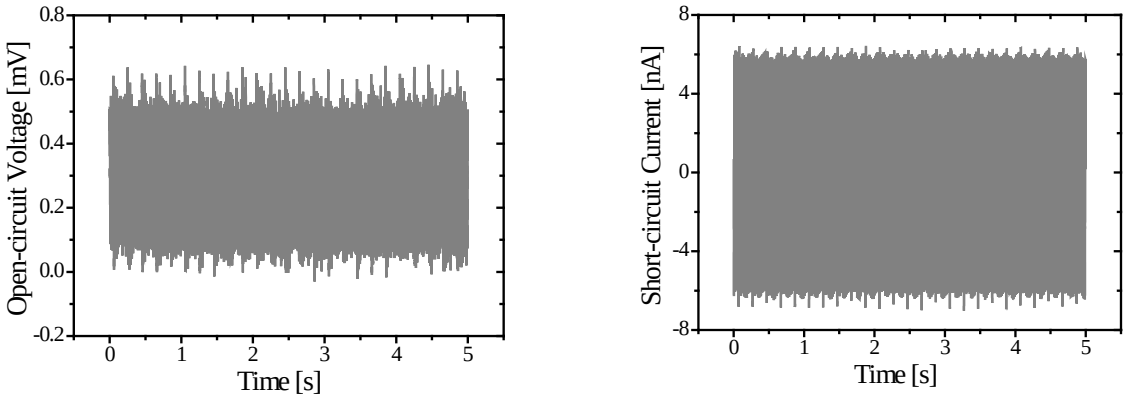

FIGURE S4.8 Measured open-circuit voltage and short-circuit current of control devices #1 with a AZO/PMMA/MoO_3/Al structure under excitation of peak acceleration of 2 m/s^2 at a frequency of 5 Hz.

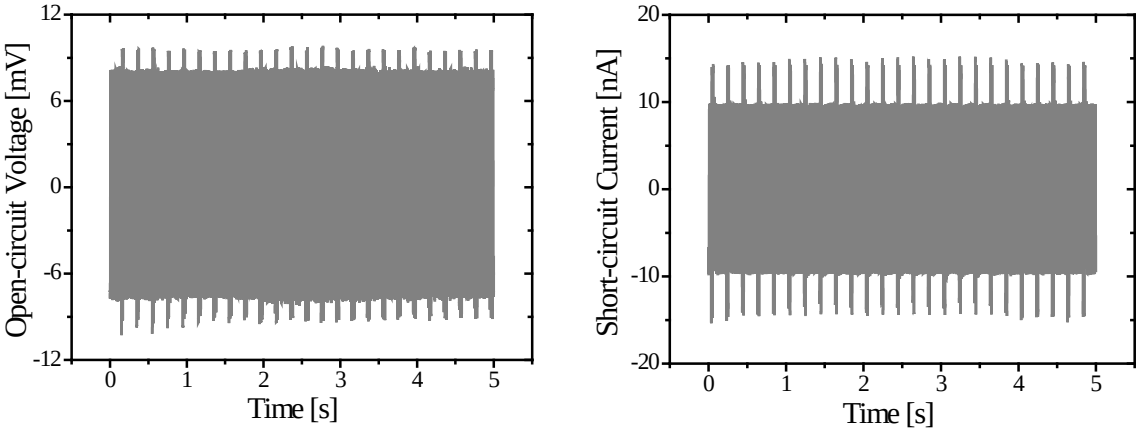

FIGURE S4.9 Measured open-circuit voltage and short-circuit current of control devices #2 under excitation of peak acceleration of 2 m/s^2 at a frequency of 5 Hz.

TABLE 4.1 Comparison of the NGs performance in this work

	V_{oc} [V]	I_{sc} [nA]	$V_{oc} \times I_{sc}$ [nW]	Ratio	R_i @ 1V [Ω]	C_i @ 100 kHz [nF]
A(0%)	0.14	15.05	2.11	100%	n/a	0.73
B(100%)	0.63	36.9	23.25	1102%	15 k	0.13
C(200%)	0.24	92	22.08	1046%	60 k	0.66
D(300%)	0.07	15.6	1.09	51.7%	1 M	0.76

(a)

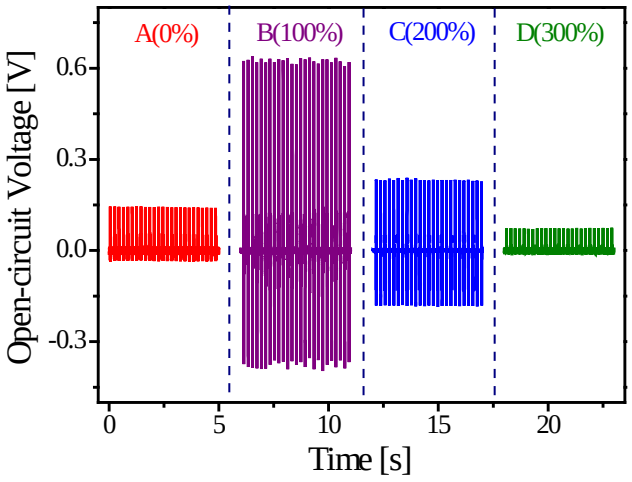

(b)

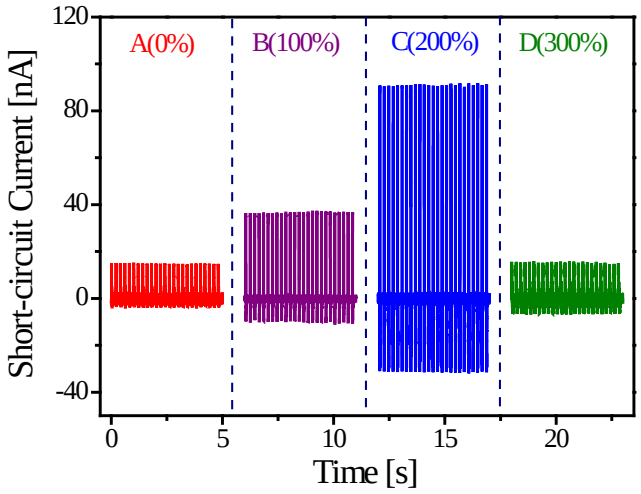

FIGURE 4.4 (a) Measured open-circuit voltage and (b) short-circuit current of NGs A, B, C, and D, showing a strong dependence on the p-doping concentration of the ZnO NWs. The excitation frequency was 5Hz and acceleration amplitude of 2 m/s^2.

NGs B performance was tested as a function of actuation level. **Figure 4.5** shows the results of a frequency sweep at a constant displacement level (5 mm peak-to-peak) and a force sweep at a constant frequency of 5 Hz. In the frequency sweep, **Figures 4.5a** and **b**, the open-circuit voltage and short-circuit current increase with the excitation frequency. The insets of **Figures 4.5a** and **b** show that the average of the peak values of V_{oc} and I_{sc} exhibit a linear dependence on frequency. As frequency

increases, the acceleration (and force) levels applied to the NGs increase, thereby increasing strains in NWs and piezoelectric energy conversion. Similarly, in the force sweep, the output increases linearly with increased input acceleration amplitude, **Figures 4.5c** and **d**. The peak open-circuit voltage and short-circuit current of NGs B reached a maximum of ~1.95 V and ~75 nA, respectively, at an excitation frequency of 5 Hz and acceleration amplitude of 3.5 m/s^2. These values represent a potential output power product ($V_{oc} \times I_{sc}$) of ~0.146 μW. Not only do longer NWs experience larger deformation as the acceleration amplitude increases, but also shorter nanowires, which are dormant at lower acceleration levels, are excited and deflected at higher acceleration amplitudes. The combined effect increases the output power of the NGs in both the frequency and force sweeps.

(a)

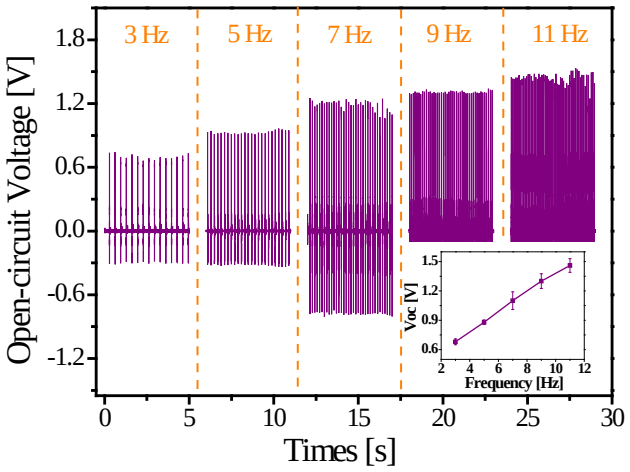

(b)

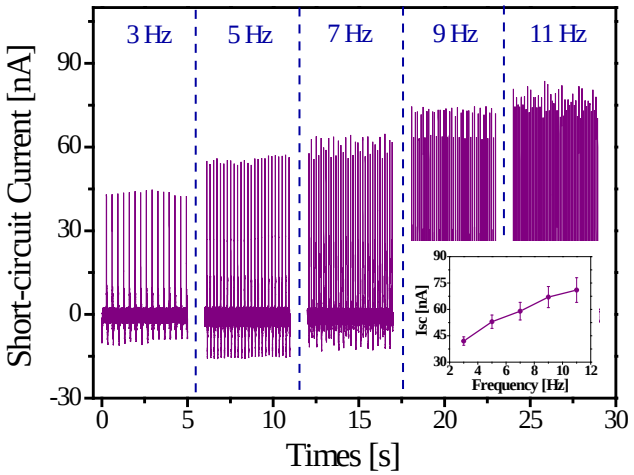

(c)

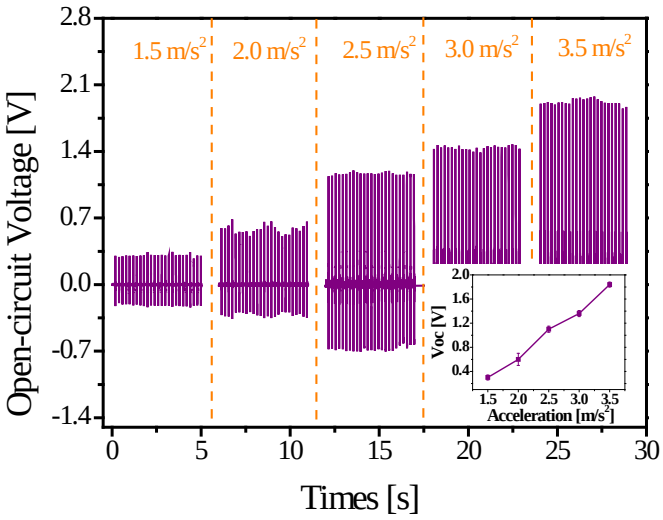

(d)

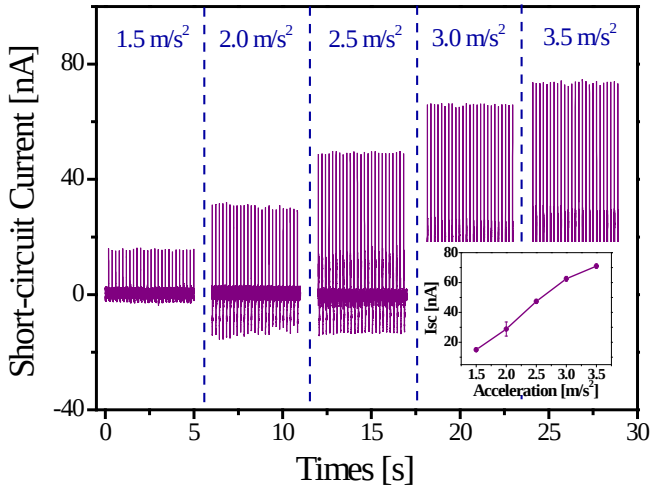

FIGURE 4.5 The frequency response and force response of NGs B. (a) Measured output open-circuit voltage and (b) short-circuit current at different excitation frequencies and a constant peak-to-peak displacement of 5 mm. The insets show that the response increases linearly with the frequency. (c) Measured open-circuit voltage and (d) short-circuit current as a function of the acceleration. The frequency was kept at a constant 5 Hz. The insets show that the output amplitude roughly linearly increases with the increase of the acceleration.

To explore the long-term stability and reproducibility of NGs, four NGs B were tested for four consecutive weeks. Each week, 5000 cycles of an excitation with an acceleration amplitude of 2 m/s^2 and frequency of 5 Hz was applied to all four NGs. The piezoelectric response in the first 1050 cycles

was recorded. In **Figure 4.6,** the open-circuit voltage output is shown, one for each of NGs B in each of the four weeks of the experiment. The insets in the figure show the waveform of the NGs' responses during 5 cycles in each week. The consistent output voltage waveform and average peak across devices and weeks prove the device-to-device and long-term stability of NGs B. Further, no perceivable performance degradation was observed from testing or storage over the four weeks period.

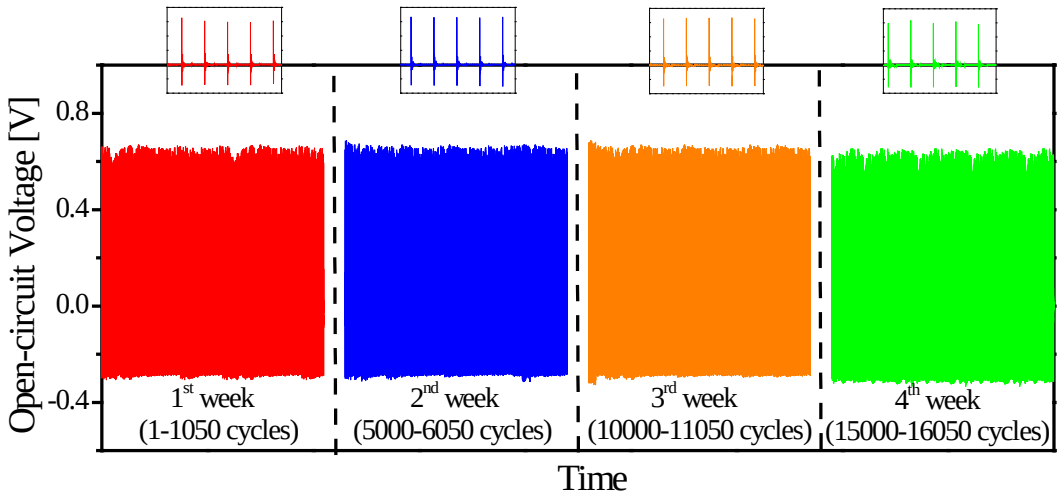

FIGURE 4.6 Measured open-circuit voltage of four different NGs B tested over four consecutive weeks. The response remains unchanged, which demonstrates the stability and reliability of the device. The excitation frequency was 5Hz and the acceleration amplitude was 2 m/s^2 in all tests.

Five NGs C with a MoO_3 layer thickness of 0, 5, 10, 15, and 20 nm, respectively, were fabricated and tested to investigate the impact of the interfacial layer on NG performance. **Figure 4.7** shows their open-circuit voltage and short-circuit current under an acceleration amplitude of 2 m/s^2 and 5 Hz frequency. Among the five NGs, the NG with a 5 nm thick MoO_3 layer yielded the highest open-circuit voltage (V_{oc} = ~0.28 V), while the NG with a 10 nm thick layer produced the highest short-circuit current (I_{sc} = ~92 nA). The NG without a MoO_3 interfacial layer had poor performance because of leakage current between the NWs tops and the top electrode. The PMMA layer on top of the NWs is thin and inconsistent, allowing localized short circuits where NW tops come into contact with the top Al electrode. The interfacial MoO_3 layer acts as a continuous insulator precluding leakage current along this route. On the other hand, increasing the MoO_3 layer thickness reduces the carrier collection efficiency of the Al electrode, possibly through carrier injection, and hence the measured NG output. **Table 4.2** shows the power product ($V_{oc} \times I_{sc}$) for the five NGs. It indicates that the optimum thickness of the MoO_3 layer is in the range of 5-10 nm.

TABLE 4.2 Effect of MoO_3 thickness on the performance of NGs C

Thickness [nm]	V_{oc} [V]	I_{sc} [nA]	$V_{oc} \times I_{sc}$ [nW]	Ratio
0	0.065	35	2.275	100%
5	0.28	40	11.2	492%
10	0.24	92	22.1	971%
15	0.06	80	4.8	211%
20	0.045	45	2.205	97%

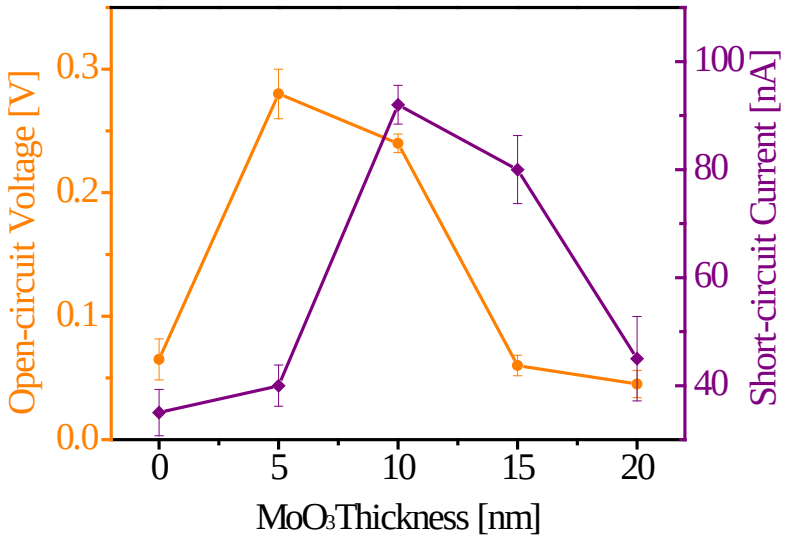

FIGURE 4.7 Measured open-circuit voltage and short-circuit current of ZnO p-n homojunction NGs with a MoO_3 interfacial layer at different thicknesses from 0 to 20 nm. The lithium nitrate mixture ratio was 200% for the growth of the p-doped segment of the p-n homojunction NWs. The excitation frequency was 5Hz and the acceleration amplitude was 2 m/s^2.

4.4 Discussion

4.4.1 The Impact of Doping on NW Piezopotential

We hypothesize that the formation of a p-n junction and a charge depletion region reduces the concentration of residual mobile charge carriers, thereby limiting their screening effect on the piezoelectric polarization and enhancing the NG's piezoelectric response [114]. To test this hypothesis, the piezopotential profiles along the *c*-axis of p-n homojunction ZnO NWs with different p-doping concentrations are shown in **Figure 4.8a** for six levels of p-doping. Similarly, the piezopotential profiles of homojunction NWs made from two n-doping concentration (n*-n) are shown in **Figure 4.8b** for six levels of n*-doping. For the p-n NWs, the acceptor concentration ranged from $N_A = 5\times10^{15}$ cm^{-}

^{3} to $N_A = 2\times10^{17}$ cm^{-3}. For the n*-n NWs, the donor concentration of the n*-doped section ranged from $N_D = 1\times10^{16}$ cm^{-3} to $N_D = 2\times10^{17}$ cm^{-3}. In both cases, the effective donor concentration of the intrinsic section (n-doped) was fixed at $N_D = 1\times10^{17}$ cm^{-3}. Other material parameters are listed in **Table S4.1** in the Supporting Information. The piezopotential was calculated for 100 nm diameter and 4 μm long NWs under a compressive force of 100 nN, corresponding to a stress of $\sigma = 11.547$ MPa, at the top end of the wire. The profiles were obtained by finite element simulation of ZnO NWs, in the TiberCAD multiscale simulation tool [104, 105]. The simulations were restricted to steady-state conditions under thermal equilibrium at 300 K and assuming no dissipation [105].

Changes in piezopotential are observed only close to the NWs' top end, where the maximum piezopotential occurs. The piezopotential gradually increases as doping concentration decreases in the NWs, **Figure 4.8c**, indicating that the screening effect can be effectively suppressed by reducing the mobile charge carrier density [103-105]. The p-doping concentration of p-n homojunction ZnO NWs, samples B, C and D, increases as the lithium nitrate mixture ratio increases in the growth precursor solution. As a result, the individual NWs' piezopotential drops and their aggregate, the open-circuit voltage (V_{oc}) of the NGs, shown in **Figure 4.4a** drops following the same sequence B, C and D. Sample A NWs are effectively n*-n homojunctions with equal doping concentrations in both n* and n sections; thus intrinsic NWs are estimated to have a background n*-type doping concentration of ~1-2×10^{17} cm^{-3} [169]. This high background mobile charge carrier density yields a low piezopotential, as seen on the far left of **Figure 4.8c**, resulting in low NGs A open-circuit V_{oc}, as seen in **Figure 4.4a**.

The position of the p-n homojunctions may be an important factor to be considered for further enhancement of the NW piezopotential. In particular, if the depletion region of the p-n homojunction is overlapping with or close to the region where the piezopotential is generated in the NWs, which merits further studies.

4.4.2 The Impact of Doping on NG Performance

These simulation results show that the marked performance improvement of NGs B and C over that of NGs A, **Figure 4.4a**, is due to increased NW piezopotential realized via low p-doping (100% and 200%) of p-n homojunction ZnO NWs. On the other hand, excessive p-doping (300%) not only reduces NW piezopotential, and thus NGs open-circuit voltage V_{oc} as seen in **Figure 4.4a**, but also undermines the piezoelectric properties of ZnO NWs. Assuming no leakage current from the bottom electrode into the PEN substrate, the open-circuit piezoelectric charge of the NGs can be written as

$$Q_i = V_{oc} C_i \tag{4.2}$$

(a)

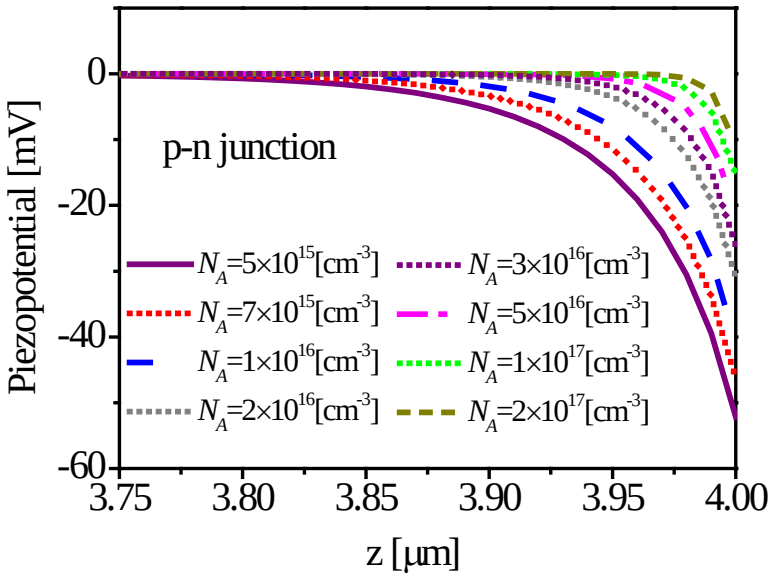
p-n junction
N_A=5×10^{15}[cm^{-3}]
N_A=7×10^{15}[cm^{-3}]
N_A=1×10^{16}[cm^{-3}]
N_A=2×10^{16}[cm^{-3}]
N_A=3×10^{16}[cm^{-3}]
N_A=5×10^{16}[cm^{-3}]
N_A=1×10^{17}[cm^{-3}]
N_A=2×10^{17}[cm^{-3}]
Piezopotential [mV]
0
-20
-40
-60
3.75
3.80
3.85
3.90
3.95
4.00
z [μm]

(b)

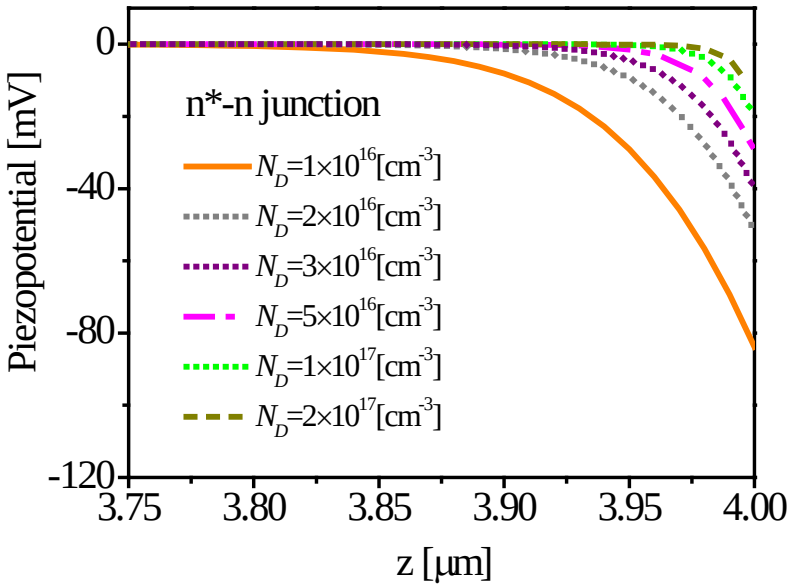
n*-n junction
N_D=1×10^{16}[cm^{-3}]
N_D=2×10^{16}[cm^{-3}]
N_D=3×10^{16}[cm^{-3}]
N_D=5×10^{16}[cm^{-3}]
N_D=1×10^{17}[cm^{-3}]
N_D=2×10^{17}[cm^{-3}]
Piezopotential [mV]
0
-40
-80
-120
3.75
3.80
3.85
3.90
3.95
4.00
z [μm]

(c)

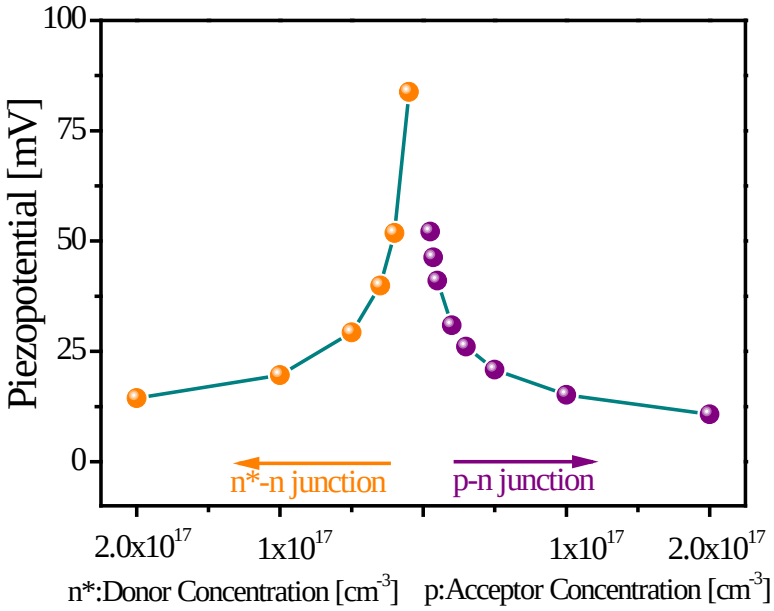

FIGURE 4.8 Simulated piezopotential distribution along the c-axis of (a) p-n and (b) n^*-n homojunction ZnO NWs (diameter D = 100 nm and length L = 4 μm) under a uniaxial compressive force of 100 nN. The piezopotential profile for the top 0.25μm of the NW is shown. The doping concentration in the p-segment of the p-n NWs varies from $N_A = 5\times10^{15}$ cm^{-3} to $N_A = 2\times10^{17}$ cm^{-3}, the doping concentration of the n^*-segment of the n^*-n NW varies from $N_D = 1\times10^{16}$ cm^{-3} to $N_D = 2\times10^{17}$ cm^{-3}, and that of the n-segment is $N_D = 1\times10^{17}$ cm^{-3}. (c) The simulated maximum piezopotential at the end of the NWs vs. the doping concentration of the homojunction.

where i=A, B, C, and D. Using the measured V_{oc} (**Table 4.1**) we calculate the charge on NGs A, B, C, and D, respectively, as 0.1022, 0.0819, 0.1584, and 0.0532 nC. The low charge level of NGs D indicates that excessive Li ion doping degrades the ZnO NWs' crystal quality and undermines their piezoelectric properties.

To further analyze the performance of NGs B and C, we note that NGs current may be approximated as

$$I = \frac{V_g}{|Z|} \tag{4.3}$$

where V_g is the voltage drop across the NG electrodes, and $|Z|$ is the magnitude of its total internal impedance. Since the NGs' inductance is negligible, impedance Z consists of a resistive component Z_r

= R and a capacitive component $Z_c = (i\omega C_i)^{-1}$ connected in parallel. Therefore, the magnitude of the total internal impedance is

$$|Z| = \frac{R_i}{\sqrt{1 + (R_i \omega C_i)^2}} \tag{4.4}$$

where ω is the angular frequency. Calculating the electric resistance at 1 V from **Figure 4.2b**, measuring the junction capacitance at 100 kHz (**Table 4.1)**, and using Equation (4), the impedance ratio of NGs B to C is ~3.93. Assuming similar piezopotential in NW samples B and C would result in open-circuit voltage V_{oc} ratio of 3.93 between NGs B and C. The measured voltage ratio is 2.63, which indicates that the piezoelectric properties of NWs sample C is better than those of sample B. Similarly, the short-circuit current ratio is 2.49 (**Table 4.1**), which again indicates that the piezoelectric properties of NWs sample C is better than those of sample B. This analysis reveals that NGs C's higher capacitance, which substantially reduces their total internal impedance, plays an important role in increasing their output current.

4.5 Conclusion

In this chapter, patterned crystalline p-n homojunction ZnO NWs were grown on flexible substrates using electrochemical deposition and successfully fabricated into nanogenerators (NGs). The lithium-doped (p-type) segment was continuously synthesized on top of the NWs' intrinsic segment (n-type). The p-doping concentration of the p-n homojunction NWs was controlled by varying the lithium nitrate mixture ratio in the growth-precursor solution.

All NGs demonstrated effective kinetic energy harvesting. Low p-doping concentrations of ZnO NWs were found to improve the performance of NW-based NGs, increasing their output power product by eleven-fold over NGs made out of intrinsic ZnO NWs. This result is attributable to reducing the mobile charge screening effect by means of the depletion region formed by p-n homojunctions. On the other hand, excessive p-doing was found to undermine the piezoelectric properties of ZnO NWs. Furthermore, it was found that low p-doping can be used to tune the internal impedance of ZnO NW-based NGs, thereby offering opportunities to balance the breakdown of the output power into output voltage and current.

An interfacial layer of MoO_3 between the nanowires and the top metal contact can also improve device performance, by suppressing leakage current. The optimum thickness of the MoO_3 is in the range of 5-10 nm. ZnO p-n homojunction nanowire-based NGs like those explored here offer a flexible power supply for self-powered electronics.

Chapter 5

Cascade-Type Hybrid Energy Cells for Driving Wireless Sensors

5.1 Motivation

Solar [58, 170-173] and vibration [174-176] energies are two of the most commonly available types of energy in the environment. They can be harvested and converted into electrical energy and used to operate autonomous wireless sensor networks (WSNs) [177]. However, vibrations generate power only while motion persists and solar energy is available only when illumination is sufficient. Thus, a technology that can harvest energy from both sources would produce a more consistent output. A nanotechnology-based compact hybrid energy cell (CHEC) is proposed here to simultaneously and individually harvest vibrations and solar energies [21, 22].

Various CHECs have been proposed to harvest vibrations, solar, and thermal energies [21, 22, 48, 146, 178-190]. Studies have described working CHECs made of intrinsic ZnO nanowires (NWs) and organic polymer blends to harvest strain and solar energies [21, 22, 48, 178, 179]. Semiconductor NW have unique energy harvesting advantages, such as enhanced surface area, high mechanical flexibility, high sensitivity to small forces, better charge collection, enhanced solar energy absorption through light trapping, and amenability to function as a template for other structures [58, 171]. However, the increase of surface area resulting from high aspect-ratio structures may also cause large nonradiative recombination across local junctions/interfaces induced by surface defects, which often undercuts these advantages [80, 191, 192].

In typical hybrid energy harvesters, the components that scavenge different types of energy are designed and fabricated independently, following distinct physical principles. Each energy harvesting modality requires its own power management circuit due to differences in output characteristics. For example, piezoelectric nanogenerators (NGs) have large output impedance and can produce high voltage but low current, while solar cells (SCs) have small output impedance, with high current but low voltage [179]. Designing a compact cell that effectively and simultaneously harvest multiple available energy sources will increase the availability and level of output power. Complementary harvesting can also be used to improve the output characteristics by increasing output current and voltage simultaneously. Achieving these goals is a challenge that requires innovative and integrated methods, materials, and structures [21, 22].

Herein, we introduce the first cascade-type transparent piezoelectric/solar hybrid energy cell synthesized on a polyethylene naphthalate (PEN) flexible substrate. The proposed cascade-type CHEC is a monolithic two-terminal structure that eliminates the large electrical losses associated with the

typical interface between mechanically stacked solar cells. In addition to achieving effective, simultaneous and complementary harvesting of strain and solar energy, it also increases power density by stacking a solar cell on top of a piezoelectric nanogenerator. The cell is made of inorganic heterostructures providing for improved chemical stability and mechanical durability. The cell consists of vertically-aligned *n*-*p* junction NW-based nanogenerator and a hydrogenated nanocrystalline/amorphous silicon (nc/a-Si:H) n^+-*i*-p^+ junction solar cell. Although the underlying physics of miniaturized junctions is not yet fully understood, they have been used to enable a diverse range of functions, such as sensors, solar cells and nanogenerators [25, 141, 160]. The NWs' and the cell's optical and electrical properties are characterized. The output power performance of the CHEC is evaluated under light illumination, vibration, and combined light and vibration input. The CHECs viability is demonstrated in charging capacitors, powering LEDs and driving wireless sensor nodes.

5.2 Methods

Figure 5.1a shows a schematic of the fabricated CHEC and its architecture. The ZnO homojunction NWs were grown hydrothermally [193]. A SiN buffer layer and aluminum-doped ZnO (AZO, 2 wt.% Al_2O_3 + 98 wt.% ZnO) layer were deposited onto a pre-cleaned polyethylene naphthalate (PEN) substrate using radio-frequency (RF) magnetron sputtering at 150°C. The SiN buffer layer improves the surface properties of the substrate. The AZO layer serves as a conductive electrode as well as a seed layer for subsequent ZnO NW growth. The aqueous solution for growing n-type ZnO NWs was a mixture of zinc (Zn) nitrate hexahydrate (25 mM), hexamethylenetetramine (25 mM) and aluminum (Al) nitrate nonahydrate. The atomic ratio of Al to (Al + Zn) in the mixture solution was controlled at 3 wt.%. To obtain *p*-type ZnO NWs (Li-doped), a doping reagent, lithium nitrate (75 mM), was added to the solution (heavily *p*-type). The solution was kept at a constant 88°C during deposition, and the ZnO NW length was simply controlled by growth time; one hour for the *n*-type section immediately followed by an additional half hour for the Li-doped *p*-type section. Additionally, *n*-*n* homojunction NWs were prepared using intrinsic (effectively *n*-type) NW growth procedure, and used as control samples [193]. All samples were cleaned using a standard process.

The solar component of the CHECs consists of a stack of n^+-*i*-p^+ nc/a-Si:H thin-film layers, deposited over the synthesized *n*-*p* and *n*-*n* homogeneous junction NWs by plasma-enhanced chemical-vapor deposition (PECVD) at a substrate growth temperature of 150°C. A 13.56 MHz PECVD cluster system was first used to deposit 60 nm of n^+ nanocrystalline (nc)-Si:H thin-film onto the NW array at an RF power density of 194 mW/cm^2 using a combination of SiH_4/H_2/PH_3 gases. Immediately after, a 500 nm thick *i*-a-Si:H intrinsic absorber layer was deposited at a power density of 9 mW/cm^2 by flowing SiH_4, followed by 60 nm of p^+ nanocrystalline (nc)-Si:H deposited at a power density of 43 mW/cm^2 using

$SiH_4/H_2/B_2H_6$ process gases. Last, a 200 nm thick AZO layer was deposited as a transparent front contact.

Photolithography was then employed to pattern the stack into arrays of square CHECs. **Figure 5.1b** shows a photograph of the patterned CHECs. The side length of the square patterns varies from 1 mm to 1 cm. The gap provides physical isolation among the CHECs of different sizes and thus avoids interference between cells. This array configuration provides a basis for effective comparison of output for a range of CHECs. Silver paste was used to glue a Cu wire lead onto the bottom AZO electrode and another onto the top AZO electrode. The completed stacks were packaged in polydimethylsiloxane (PDMS), Dow Corning Sylgard 184, pre-mixed with curing agent at a ratio of 10:1 w/w, then degassed to prevent contamination, damage, and moisture penetration from the ambient environment.

The morphology of the as-grown ZnO NWs was obtained using a Zeiss Orion Plus Helium Ion Microscope (HIM). Optical characterization of the NW structures was performed using a UV/Visible spectrophotometer (Shimadzu, UV-2501PC). The current-voltage (*I-V*) curves of the CHECs and their junction capacitance were measured using a Keithley 4200-SCS semiconductor characterization system, calibrated before measurements to keep the system noise down to 1fF in a wide frequency range (1kHz ~ 10MHz). The photovoltaic parameters were measured under 1-sun AM1.5G radiation from an ABET Sun 3000 Class AAA solar simulator with a Keithley 2400 source/meter. Piezoelectric characterization was carried out using a system that included a close loop controller (Vibration Research Corporation, VR9500) and a linear shaker (Labworks Inc., ET-126B-1) to provide sinusoidal waves simulating a vibration source with a known amplitude and frequency. Output voltage and current signals were measured using low-noise voltage/current preamplifiers (Stanford Research System Model SR560/570) and a National Instruments I/O module (NI CompactDAQ USB-9239). The input resistances of the voltage and current preamplifiers were 100 MΩ (SR560) and 10 kΩ (SR570), respectively. To minimize electromagnetic interference, the two copper wires connected to the device under test were twisted together. All measurements were conducted at ambient room temperature.

5.3 Results and Discussion

The NGs are based on densely packed ZnO *n-p* or *n-n* homogeneous junction NWs. **Figure 5.1c** shows a cross-sectional HIM image of a typical CHEC. The image confirms the monolithic and seamless integration between the nc/a-Si:H n^+-*i*-p^+ layers and the underlying ZnO NW layer. The ZnO NWs are used as the piezoelectric material for mechanical energy conversion and as the electron transport layer for the solar cell. **Figure 5.1d** shows top-view HIM images of the as-grown *n-p* and *n-n* homojunction

ZnO NWs, indicating uniform growth of high-density and vertically-aligned NWs. The average length and diameter of these NWs are ~800 nm and 80 nm, respectively.

(a)

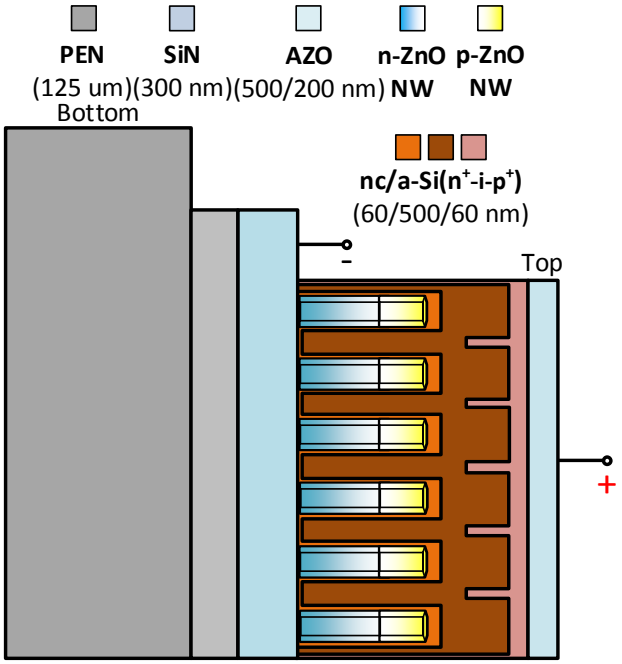

(b)

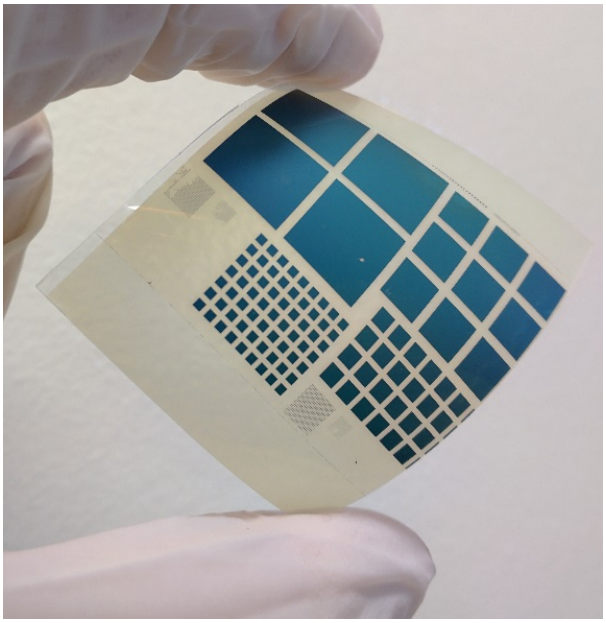

(c)

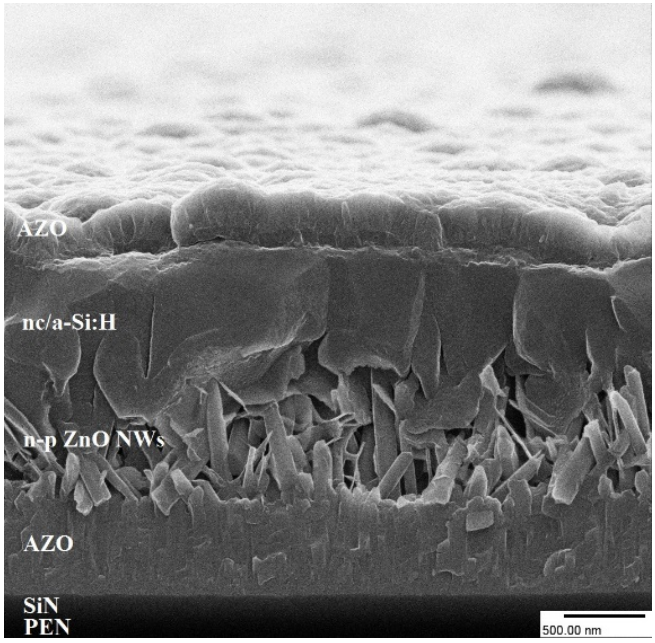

(d)

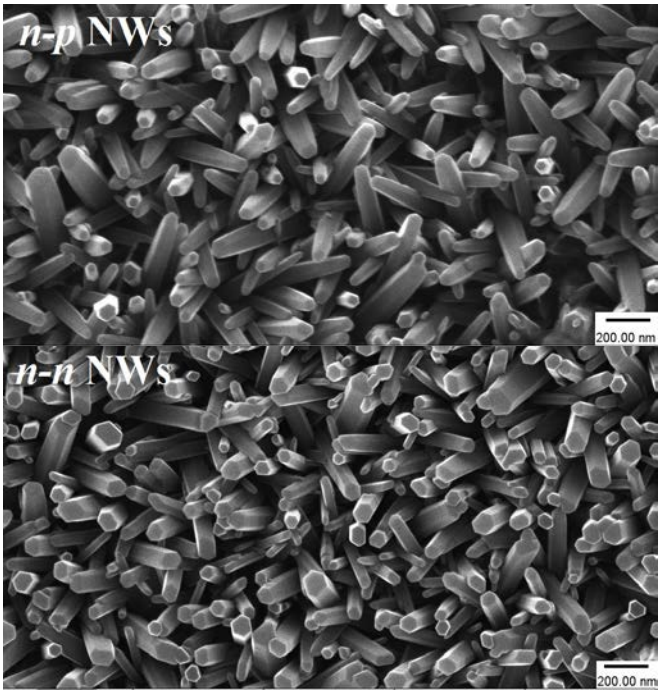

FIGURE 5.1 (a) A schematic diagram of a CHEC made of *n-p* homojunction ZnO NWs grown on a flexible substrate (cross sectional view). (b) A photograph of patterned CHEC arrays (top view). (c) A cross-sectional helium ion microscopy (HIM) image of a fabricated CHEC. (d) HIM images of the *n-p* (top) and *n-n* (bottom) homojunction ZnO NW arrays.

This monolithic CHEC can exploit piezopotential under compressive strain and photovoltaic potential under ambient optical illumination to generate electrical power. The hybrid cell, when placed solely under light illumination, follows the usual solar power generation scheme to produce continuous photocurrent output. The photocurrent flows from the n^+-nc-Si layer to the p^+-nc-Si layer, from bottom to top in **Figure 5.1a**. When a compressive force is applied, negative piezopotential (*V*-) is generated at the AZO/*n*-ZnO NW interface (bottom) and positive piezopotential (*V*+) at the *p*-ZnO NW/n^+-nc-Si interface (top). The photovoltaic potential and the piezopotential have the same direction, thus the resulting output signal is combined constructively [22], resulting in the creation of a voltage drop between a positive (top) lead and a negative (bottom) lead that drives current through an external load. Owing to the high interfacial energy barrier, electrons accumulate at the interface between the p^+-nc-Si layer and top AZO electrode until the resulting potential balances the piezopotential in an equilibrium state. Once the compressive load is released, the piezopotential drops to zero, and the electrons accumulated around the p^+-nc-Si layer flow back to the bottom AZO electrode via the external circuit. Consequently, a negative electric pulse is generated, and the system returns to its initial equilibrium state [14].

Figure 5.2a shows the measured optical absorption spectra of the *n-p* and *n-n* NW arrays in the wavelength range of 300-800 nm. The peak absorption spectra is observed at λ=~385 nm in the *n-n* ZnO NWs, corresponding to the bandgap energy of ~3.2 eV. This fact is attributed to the near band-gap absorption of ZnO. The peak absorption wavelength in the doped *n-p* homojunction NWs shows a slightly shift to a longer wavelength of ~390 nm. The *n-p* junction ZnO NWs also show stronger optical absorption over the visible and near-infrared wavelength range compared with the *n-n* ZnO NW arrays. The absorption spectra show oscillations in the wavelength range between 600 and 800 nm, which can be attributed to the Fabry-Perot resonance along the layer growth direction.

Figure 5.2b shows the current density-voltage (*J-V*) curves of the 2 mm CHECs made using *n-n* and *n-p* ZnO NWs under AM 1.5 illumination with 100 mW/cm^2 light intensity and no mechanical strain. The *n-n* junction CHECs produce a short-circuit current density (J_{sc}) of 8.7 mA/cm^2, an open-circuit voltage (V_{oc}) of 0.731 V, a cell fill factor (FF) of 39.6%, and a power conversion efficiency (η) of 2.53%. The CHECs with *n-p* junction NWs achieve a higher current density J_{sc} of 9.5 mA/cm^2 and efficiency η of 2.96%, but similar voltage V_{oc} of 0.735 V and FF of 42.3%. The devices' low solar power conversion efficiency (PCE) is attributed to the uneven surface of the cell due to deposition of the nc/a-Si layers on top of ZnO NWs and the use of a soft substrate. The marginal improvement in the output current and efficiency of *n-p* CHECs over *n-n* CHECs corresponds well with the marginally superior optical absorption of *n-p* NWs over *n-n* NWs and lower *n-p* CHECs resistance.

(a)

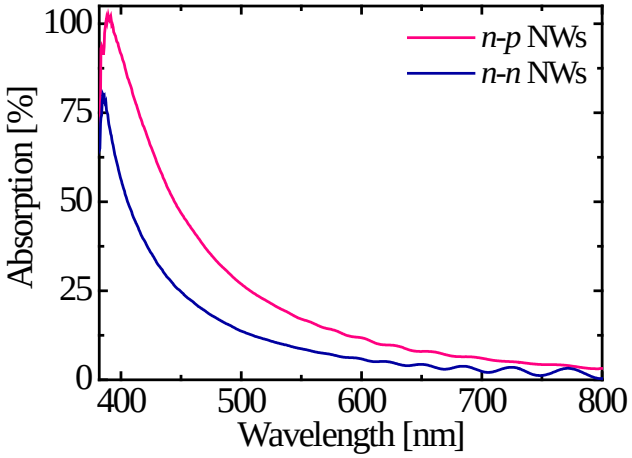

(b)

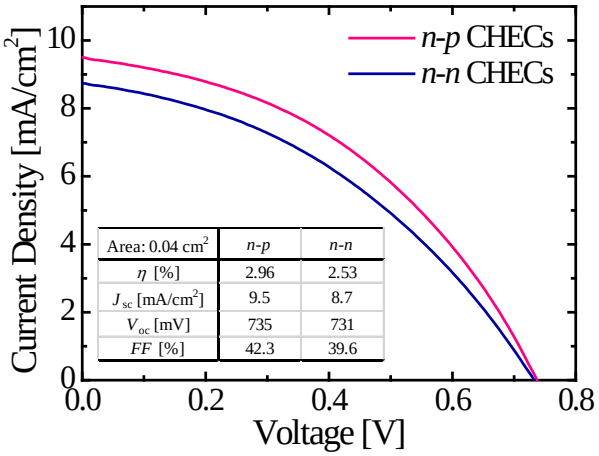

FIGURE 5.2 The measured (a) optical absorption spectra for the *n-p* and *n-n* ZnO homojunction NWs and (b) The current density-voltage (*J-V*) characteristics of 2 mm CHEC array under AM1.5G (100 mW/cm^2).

Larger 1 cm CHECs were used to harvest more solar and mechanical energy. **Figure 5.3a** shows a typical current-voltage (*I-V*) curve under dark conditions and no mechanical strain, with an inset of the corresponding semilog *I-V* plot. The CHECs maintain almost zero current until the voltage exceeds a threshold voltage. A rectifying characteristic is clearly exhibited, demonstrating that the *n-p* and *n-n* homojunction NWs and n^+-*i*-p^+ Si thin film behave as well-defined diodes. The rectification ratio of the *n-p* CHECs is 1.32×10^4 at bias voltages of -1 and +1 V. The turn-on voltage is approximately 0.7 V for both types of CHECs.

To further understand the influence of the junction and electronic structures on the CHECs, the capacitance-voltage responses were measured and shown in **Figure 5.3b**. To measure the CHEC capacitance, the AC signal is set to 10 mV and 5 kHz while the DC bias is varied from -1 V to +3 V. The anode was connected to the top AZO layer and the cathode to the bottom AZO layer. The results show that capacitance saturates at a large value for negative bias voltage and at a small value for bias voltages in the range of 1-3 V. In between these two ranges, capacitance decreases drastically as voltage increases from 0 to +1 V. The *n-p* junction CHECs have lower capacitance compared to the un-doped *n-n* CHECs because the additional junction capacitance associated with the *n-p* junction is in series with the junction capacitance of the n^+-*i*-p^+ Si junction.

Figure 5.4a shows the voltage output of the 1 cm CHECs under indoor ambient illumination (~10 mW/cm^2) and no mechanical strain. The DC-type step-function photovoltaic output was obtained by repeatedly turning the indoor light source on and off at 1 s and 2 s intervals. The *n-p* junction CHECs yield a higher open-circuit voltage (~0.6 V) than the *n-n* junction CHECs (~0.55 V), but comparable current output (~280 μA). The resistance of the *n-p* CHECs is 1.7 kΩ lower than that of the *n-n* CHECs at 4.5 kΩ, both calculated at 1 V, as in **Figure 5.3a**. The lower resistance and higher output voltage V_{oc} would suggest a higher output current for the *n-p* CHECs over the *n-n* CHECs. The fact that this did not happen in the 1 cm CHECs but did in the 2 mm ones suggests that current output is suppressed by material and interface defects, which grow with cell size.

The piezoelectric response of the CHECs under dark conditions is presented in **Figure 5.4b**. The CHECs were anchored on a fixed stopper and the shaker moved back and forth, applying periodic strain to the NWs by striking the CHECs at the end of each cycle [140, 141]. The excitation frequency was set to 3 Hz, and an acceleration amplitude of 3 m/s^2. The results show the open-circuit voltage V_{oc} of *n-p* junction CHECs is 138 times higher than that of the *n-n* junction CHECs, reaching a maximum of +2.5 V, and the maximum short-circuit current I_{sc} is more than twice that of the *n-n* junction CHECs. Clearly, both results are attributable to substantial reduction in the mobile charge screening effect by means of the depletion region formed by the *n-p* homojunction [25, 141]. The fact that the improvement in the output current I_{sc} of the *n-p* CHECs is two orders-of-magnitude lower than the improvement in output voltage V_{oc} suggests again that current output is being suppressed by material and interface defects.

While the SC has a relatively high output current, on the order of mA, it has a low output voltage of 0.5-0.6 V. Conversely, the output voltage of the NG component can be up to several volts, but with less than 1 μA output current. Hence, a hybridization of the SC and NG would enable the utilization of their advantages, thereby providing a high current, high voltage device. To demonstrate simultaneous

harvesting of solar and mechanical energies, the CHECs were tested under indoor optical illumination and mechanical strain input. The open-circuit voltage is shown in **Figure 5.4c**. During the experiment, an acceleration with 3 m/s^2 amplitude and 3 Hz frequency was applied continuously. An indoor illumination of ~10 mW/cm^2 was applied for a short period (2 s), then dark conditions were resumed. For the *n-p* junction CHECs, the maximum output voltage exceeds 3 V when combined piezoelectric and photovoltaic harvesting is realized. The results show that the outputs from the solar cell (SC) component and the nanogenerator (NG) component combine constructively, verifying that the CHEC can simultaneously and individually harvest solar and mechanical energies.

(a)

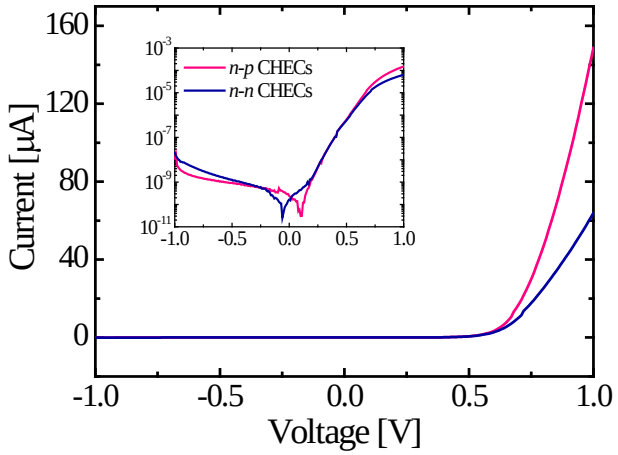

(b)

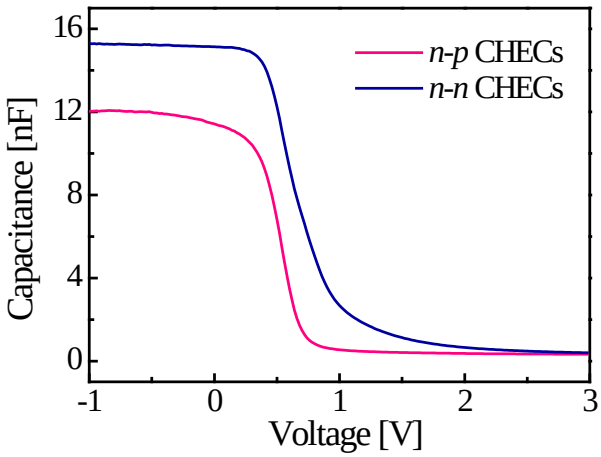

FIGURE 5.3 The measured (a) current-voltage (*I-V*) characteristics of the *n-p* and *n-n* junction CHECs (inset shows the corresponding semilog *I-V* plot) under dark conditions and no mechanical strain, and (b) capacitance-voltage responses for 1 cm side length *n-p* and *n-n* junction CHECs. The AC signal was set to 10 mV and 5 k Hz. All the *C-V* measurements were performed under dark conditions and no mechanical strain with a bias varying from -1.0 to 3.0 V.

(a)

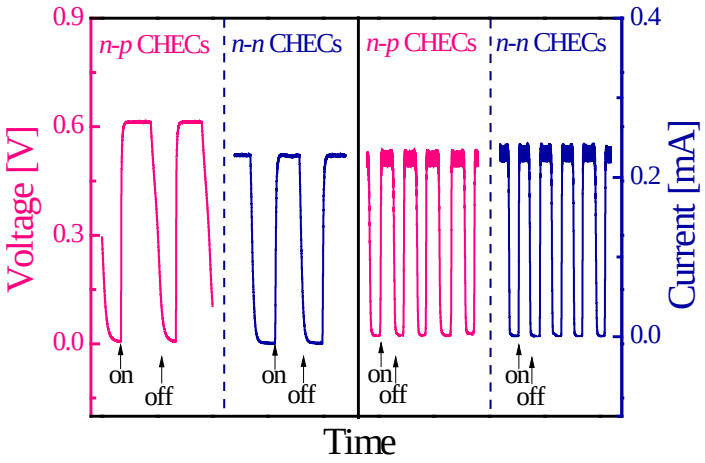

(b)

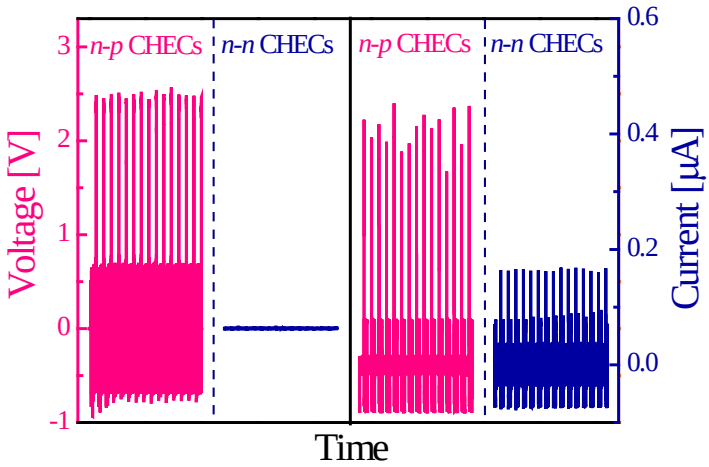

(c)

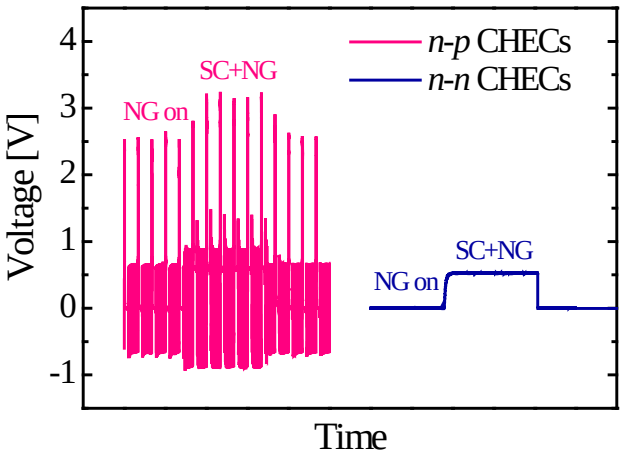

FIGURE 5.4 The open-circuit voltage and short-circuit current of *n-p* and *n-n* junction CHECs at (a) ambient indoor optical illumination level (~10 mW/cm^2) and no mechanical strain and (b) an acceleration amplitude of 3 m/s^2 and a frequency of 3 Hz under dark conditions. (c) The output voltage of the CHECs for combined harvesting of solar and mechanical energies. The ambient indoor optical illumination is ~10 mW/cm^2 and the mechanical excitation is 3 Hz in frequency and 3 m/s^2 in acceleration amplitude.

The hybrid energy cell's potential to charge capacitors, power LEDs, and drive wireless sensor nodes is illustrated using the *n-p* junction CHECs under ~10 mW/cm^2 illumination and an acceleration amplitude of 3 m/s^2 at 3 Hz frequency. Their output is rectified using a full-wave bridge. **Figure 5.5a** shows the charging curves of a 1 cm CHEC used to charge a 10 μF capacitor. From the inset of **Figure 5.5a**, one can observe that, on its own, the solar cell charges the capacitor from 0 V to 0.61 V in 0.3 s. In contrast, the combined CHEC charges the same capacitor to a voltage of 2.0 V in 920 s. The comparison results indicate that the hybrid cell can compensate for the lower voltage output of the solar cell component.

To enhance the output of the CHEC, six cells were integrated in series to charge a 1000 μF capacitor. This configuration was then utilized to power eight blue and three white LEDs connected in parallel. The emitted light lasted for 0.5-1.0 s and is clearly captured against the background in **Figure 5.5b**.

The CHECs' capacity to sustainably drive a wireless sensor node was tested on a commercial EH-LINK hybrid wireless sensor node (LORD Corporation). On this node, the AC signal of six CHECs connected in series was first rectified by the full-wave bridge and the charge was stored in the 1000 μF capacitor.

A custom-made full Wheatstone bridge was implemented using four 350 Ω commercial strain gauges sensors (**Figure 5.5c**,Vishay precision group) to measure the strain at the root of a cantilever beam. The wireless sensor node was used to transmit the measured signal to a USB base station connected to a computer. Once the data had wirelessly arrived at the base station, the strain data was recorded on the computer. **Figure 5.5d** shows the received strain signals obtained from this experimental setup. When the excitation frequency of the beam was set to 3 Hz and the acceleration amplitude to 3 m/s^2, the measured strain was about 1600 με. These results demonstrate the proposed hybrid energy cell's capacity to power commercial electronics.

(a)

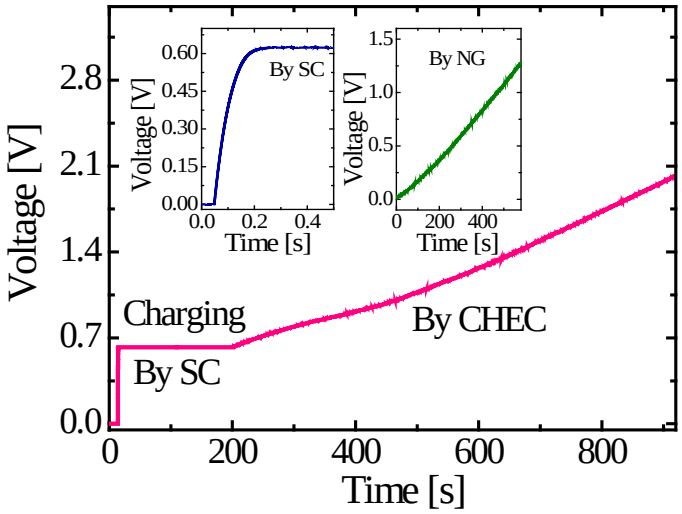

(b)

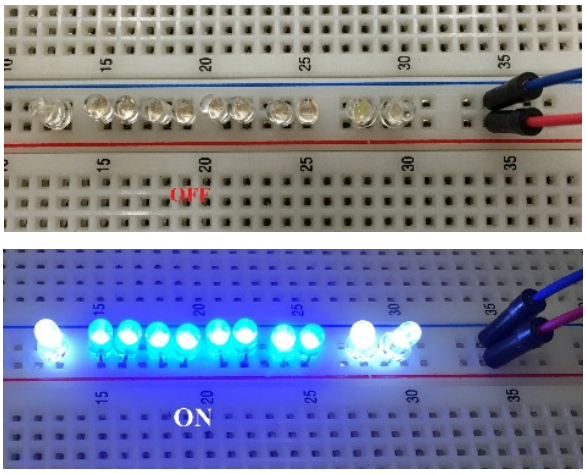

(c)

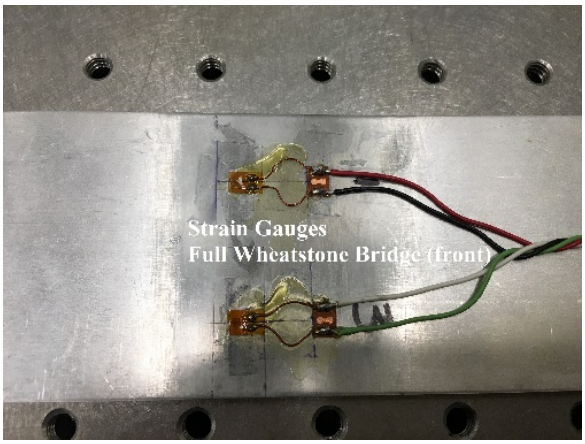

(d)

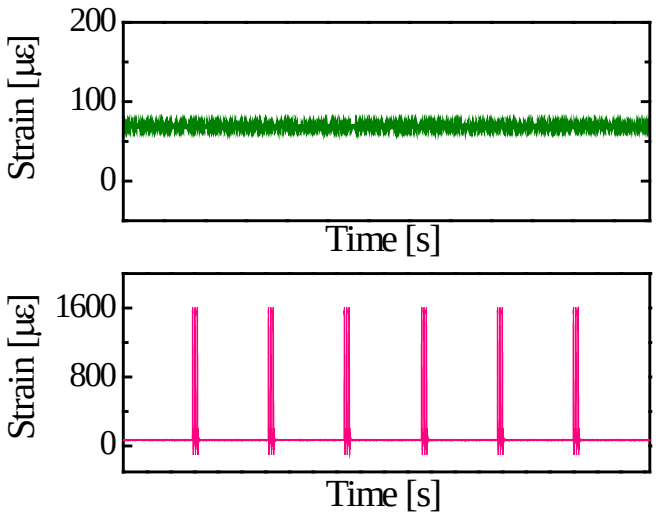

FIGURE 5.5 Applications of the *n-p* CHECs. (a) The voltage charging curves across a 10 μF storage capacitor being charged by an individual CHEC. The insets are the charging curves for the NG and SC component, separately. (b) A photograph of eight blue and three white LEDs before and after being powered by a 1000 μF capacitor. (c) A photograph of two commercial strain gauges (the front-side of a Wheatstone bridge) incorporated into the wireless sensor node. (d) The measured strain signals (top) without vibrations and (bottom) with vibrations, which are received from the wireless strain gauge sensor powered by the energy harvesting system that consists of the CHECs, the full-wave bridge rectifier and the 1000 μF capacitor.

5.4 Conclusion

This chapter introduced a hybrid energy cell made of a solar cell stacked on top of a piezoelectric nanogenerator. The nanogenerator was made of vertically aligned *n-p* homojunction ZnO NWs hydrothermally grown on a flexible substrate. The solar cell was made of n^+-*i*-p^+ nc/a-Si:H thin-film. The resulting hybrid cells were patterned into arrays of transparent square CHECs on a flexible PEN substrate.

The CHECs were able to harvest strain and solar energies simultaneously and individually. The *n-p* junction CHECs were found to improve the voltage output from strain energy 138 times over that of the *n-n* junction CHECs and the current output more than twice that of the *n-n* junction CHECs. In addition, solar cells with *n-p* junction NWs achieved marginally better energy conversion efficiency over *n-n* junction cells. The hybridized device can compensate for the lower voltage output of the solar cell with the higher voltage output of the piezoelectric nanogenerator. Its energy harvesting performance will also be improved under low mechanical strains and high light intensity, thereby making the CHECs more versatile for use in uncertain environments. The combined power output allows also for constructive coupling of the solar cell and nanogenerator and eliminates the need for two independent power management circuit for each of them as is the case in other hybrid cells. In addition to energy harvesting, the cell can also serve as a photodetector and force/pressure/strain sensor.

Under indoor illumination conditions and an acceleration amplitude of 3 m/s^2 at 3 Hz frequency, the output current and voltage from a single 1.0 cm^2 *n-p* CHEC were 280 μA and 3.0 V, respectively; enough to drive low power commercial electronics. The capacitor charging performance of the CHECs was better than that of the individual energy harvesting units. The CHECs were integrated in series to light up 8 blue and 3 white LEDs and to drive a wireless strain gauge sensor node. Cascade-type ZnO *n-p* homojunction NWs CHECs are a significant step toward effective energy harvesting. They offer a flexible power supply for self-powered electronics.

Chapter 6
Conclusions, Contributions and Recommendations

6.1 Research Summary

This research has carried out a systematic investigation of semiconductor nanowire-based piezoelectric energy harvesters, focusing on their modelling, fabrication and characterization. Simulations for InN NWs have been used to systematically show the influence of different parameters on the equilibrium-state piezopotenital distribution in a deformed semiconductive NW. The donor concentration has been shown to markedly affect the electric potential distribution. In particular, a donor concentration of $N_D > 10^{18} cm^{-3}$ neutralizes the electric potential across the NW. Increasing in the applied force has been shown to increase the value of the electric potential. The influence of geometric parameters has also been investigated: NW length does not affect electric potential distribution, but increasing the radius of the NW decreases it. The Schottky barrier height affects the potential near the NW's free end significantly, because it changes the electron distribution accumulated near the fixed end. Finally, it must be pointed out that the above results were obtained for the equilibrium case only. In reality, the dynamics have to be taken into account if the mechanical deformation process is rather fast. In addition, a NG based on InN NW arrays, grown epitaxially on an Mg-doped Si substrate, was successfully fabricated. The statistical distributions of the piezoelectric potential produced by the p-type InN nanowires under the deflection of AFM tips were investigated. Maximum output power density occurred at ~0.012 $\mu W/cm^2$. Measurement of the three-dimensional integrated NG showed that the maximum output voltage and current reached 0.055 V and 211 nA, respectively, at 3 Hz.

Patterned crystalline p-n homojunction ZnO NWs were grown on flexible substrates using electrochemical deposition and successfully incorporated into nanogenerators (NGs). The lithium-doped (p-type) segment was sequentially synthesized on top of the NWs' intrinsic segment (n-type). The p-doping concentration of the p-n homojunction NWs was controlled by varying the lithium nitrate mixture ratio in the growth-precursor solution. All devices demonstrated effective kinetic energy harvesting. With p-doping concentration tuning, device performance improves eleven-fold over that of devices made only of intrinsic ZnO nanowires, a result attributable to the mobile charge-screening effect being slowed via the p-n homojunction and optimization of internal electrical characteristics. An interfacial layer of a MoO_3 between the nanowires and the top metal contact can also improve device performance, by suppressing leakage current. The optimum thickness of the MoO_3 is in the range of 5-10 nm. ZnO p-n homojunction nanowire-based NGs promise a flexible power supply for self-powered electronics.

Our hybrid energy cell consisting of a NG and solar cell (SC) has been demonstrated to simultaneously/individually harvest vibration and solar energies. The fabricated CHEC produced an open-circuit voltage of about 3 V and a short-circuit current density of about 0.84 mA/cm^2, enough to drive a wireless strain gauge sensor node. The hybrid energy cell charged a capacitor better than the individual energy harvesting units did. Such hybrid energy cells may be a significant step toward solar and vibration energy harvesting.

6.2 Contributions

1) p-Type InN NW-based NG

As high-quality InN nanomaterials are difficult to grow and fabricate, research on InN-based NGs is now underway, as is investigation into related theoretical calculation. This work presents the first realization of an InN NW-based NG with a p-type doping concentration grown by MBE methods. It analyzes the structural characteristic and Raman spectroscopy of the InN nanowire arrays; investigates the effects of doping on the crystalline quality, Schottky barrier, and surface potential using XRD, C-AFM, and KPFM; and confirms stable and reproducible output voltage and current for NGs.

2) Flexible ZnO p-n homojunction NWs-based NGs

The performance of piezoelectric NGs depends not only on their material's piezoelectric coefficient, but also on their suppression of the screening effect from mobile charge carriers. To overcome this fundamental constraint, several approaches have been proposed and demonstrated, including surface oxygen plasma treatment, triboelectric layer insertion, and p-n junction formation. In the p-n junction scheme, the carrier density is significantly reduced by a depleted region formed at a heterojunction between the NWs (n-type) and another p-type material. This thesis systematically and experimentally investigates flexible NGs made of patterned ZnO homojunction NWs with different p-doping concentrations and grown using consecutive electrochemical deposition. Optical/electrical characterizations and SIMS results have confirmed the formation of ZnO nanowire-based homojunctions. Moreover, properly controlling the doping concentration on the p-doped section of the NWs can produce an eleven-fold improvement in device performance.

3) Hybrid energy cell that uses vertically aligned p-n junction ZnO NWs

Energy harvesters for scavenging two or more kinds of energy are usually designed independently, following distinct physical principles. For example, a piezoelectric NG has a large output impedance and can produce high voltage but low current, while a solar cell (SC) has a small output impedance, with high current but low voltage. Thus, designing a compact cell that effectively and complementarily uses any available energy resources is challenging and requires innovative methods and integrated

materials or structures. This work presents the first realization of a transparent hybrid energy cell that uses vertically-aligned p-n junction ZnO NWs synthesized on a PEN flexible substrate by hydrothermal method. The design avoids the large output impedance typical with piezoelectric NGs: the bottom has a flexible p-n homogeneous ZnO nanowire array to harvest mechanical energy, and the top has an a-Si:H single junction solar cell to harvest solar energy. The samples' transparency was evaluated by measuring the transmittance spectra, and their optical and electrical properties were investigated for solar cell application and vibration energy harvesting. Output power was generated from light illumination and vibration together and individually. In addition to converting both solar and vibration energies to electrical energy, the cell also detects weak light and subtle pressure and vibration, and thus enables more-efficient energy harvesting from the ambient environment.

6.3 Recommendations and Future Work

1) Piezoelectric constant measurement of InN NWs

Piezoelectric constants like d_{33} are essential for evaluating the performance of NWs in energy harvesting devices. Typically, piezoelectric constant-measurement methods can be either direct or indirect. The direct methods include AFM probing, single/double beam optical interferometry, plus the cantilever beam, normal or periodical load methods. The indirect methods include impedance testing, resonant testing, and acoustic testing. In general, direct testing is more reliable than indirect since the latter uses assumptions to calculate the piezoelectric constants.

2) Investigating the nonlinear piezoelectric response of NGs

When large mechanical stresses or electric fields are applied to piezoelectric material, most mechanical, electrical, and piezoelectric coefficients show nonlinear behavior. For nonlinear piezoelectricity, extra terms in the polarization, strain, and piezoelectric coefficient relation need to be considered. Knowing the characteristic of nonlinear systems is useful, especially for flexible piezoelectric energy harvesters (PEHs), and the corresponding dynamic response. Although some research on these systems exists, the corresponding theoretical investigations are still insufficient and so a systematic analysis is needed. Compared with the investigation of actual devices, simulation costs less time and money and is more convenient for device optimization. PEHs can been analyzed under parametric uncertainty using a linear model. Uncertainty in a system's natural frequency is considered as a Gaussian with various unit means and standard deviations. Monte Carlo simulation (MCS) can be used to clarify the effect of parametric uncertainty on harvested power. Theoretical investigations of a nonlinear PEH model can been presented, along with a brief comparative study of the chaotic response. Electromechanical phase trajectories of both nonlinear and linear models can be compared theoretically, allowing the substantial advantages of the former to be observed at several frequencies. Studies have revealed that linear models

integrated with nonlinear behavior can be used to improve response characteristics and broaden frequency response.

3) Optimization of the performance of hybrid energy cells

This thesis has demonstrated the first realization of a transparent hybrid energy cell that uses vertically aligned p-n junction ZnO NWs. However, more specific experiments are required for performance optimization, such as of the charge carrier transfer dynamics, the piezoelectric material growth process and thickness of different device layers. Another key issue is to develop more-efficient energy harvesting and management circuitry for transferring harvested energy from the piezoelectric layers to the battery layers for storage, as well as for managing the energy consumed by the sensor node. Future work should investigate not only optimization of the harvesting circuitry, but also the development of electronics that can be directly embedded in the energy-harvesting device. Advances in these areas will mean that all required components can be integrated into a single device. The development of hybrid energy cells presented in this dissertation holds promise for enabling the creation of autonomous, self-powered electronics. The groundwork is presented here; future work addressing the key development issues of the technology will ultimately lead to the cells' widespread use.

Bibliography

[1] C. Boller, F. K. Chang, and Y. Fujino, *Encyclopedia of structural health monitoring*: Wiley, **2009**.

[2] D.-H. Wang and W.-H. Liao, "Wireless transmission for health monitoring of large structures," *IEEE Trans. Instrum. Meas.,* **2006**, 55, 972-981.

[3] W. C. Wilson, D. C. Malocha, N. Y. Kozlovski, D. R. Gallagher, B. H. Fisher, J. M. Pavlina, N. Saldanha, D. Puccio, and G. M. Atkinson, "Orthogonal frequency coded SAW sensors for aerospace SHM applications," *IEEE Sensors J.,* **2009**, 9, 1546-1556.

[4] C. Bowen, H. Kim, P. Weaver, and S. Dunn, "Piezoelectric and ferroelectric materials and structures for energy harvesting applications," *Energy Environ. Sci.,* **2014**, 7, 25-44.

[5] A. Khaligh, P. Zeng, and C. Zheng, "Kinetic energy harvesting using piezoelectric and electromagnetic technologies—state of the art," *IEEE Trans. Ind. Electron.,* **2010**, 57, 850-860.

[6] Z. L. Wang, "Self‐Powered Nanosensors and Nanosystems," *Adv. Mater.,* **2012**, 24, 280-285.

[7] Y. Hu, L. Lin, Y. Zhang, and Z. L. Wang, "Replacing a Battery by a Nanogenerator with 20 V Output," *Adv. Mater.,* **2012**, 24, 110-114.

[8] D. Choi, M.-Y. Choi, H.-J. Shin, S.-M. Yoon, J.-S. Seo, J.-Y. Choi, S. Y. Lee, J. M. Kim, and S.-W. Kim, "Nanoscale networked single-walled carbon-nanotube electrodes for transparent flexible nanogenerators," *J. Phys. Chem. C,* **2009**, 114, 1379-1384.

[9] L. Gu, N. Cui, L. Cheng, Q. Xu, S. Bai, M. Yuan, W. Wu, J. Liu, Y. Zhao, and F. Ma, "Flexible fiber nanogenerator with 209 V output voltage directly powers a light-emitting diode," *Nano Lett.,* **2012**, 13, 91-94.

[10] A. Koka, Z. Zhou, and H. A. Sodano, "Vertically aligned BaTiO 3 nanowire arrays for energy harvesting," *Energy Environ. Sci.,* **2014**, 7, 288-296.

[11] S. Lee, S. H. Bae, L. Lin, Y. Yang, C. Park, S. W. Kim, S. N. Cha, H. Kim, Y. J. Park, and Z. L. Wang, "Super‐Flexible Nanogenerator for Energy Harvesting from Gentle Wind and as an Active Deformation Sensor," *Adv. Funct. Mater.,* **2013**, 23, 2445-2449.

[12] J. Briscoe, N. Jalali, P. Woolliams, M. Stewart, P. M. Weaver, M. Cain, and S. Dunn, "Measurement techniques for piezoelectric nanogenerators," *Energy Environ. Sci.,* **2013**, 6, 3035-3045.

[13] J. Briscoe, M. Stewart, M. Vopson, M. Cain, P. M. Weaver, and S. Dunn, "Nanostructured p‐n Junctions for Kinetic‐to‐Electrical Energy Conversion," *Adv. Energy Mater.,* **2012**, 2, 1261-1268.

[14] K. Y. Lee, B. Kumar, J.-S. Seo, K.-H. Kim, J. I. Sohn, S. N. Cha, D. Choi, Z. L. Wang, and S.-W. Kim, "P-Type polymer-hybridized high-performance piezoelectric nanogenerators," *Nano Lett.,* **2012**, 12, 1959-1964.

[15] Y. Nie, P. Deng, Y. Zhao, P. Wang, L. Xing, Y. Zhang, and X. Xue, "The conversion of PN-junction influencing the piezoelectric output of a CuO/ZnO nanoarray nanogenerator and its application as a room-temperature self-powered active H2S sensor," *Nanotechnology,* **2014**, 25, 265501.

[16] P. Wang, P. Deng, Y. Nie, Y. Zhao, Y. Zhang, L. Xing, and X. Xue, "Synthesis of CdS nanorod arrays and their applications in flexible piezo-driven active H2S sensors," *Nanotechnology*, **2014**, 25, 075501.

[17] F. F. Comjani, U. Willer, S. Kontermann, and W. Schade, "Influence of the metal-semiconductor contact by energy harvesting from vertically aligned zinc oxide nanowires," *Appl. Phys. Lett.,* **2014**, 104, 143113.

[18] N. Jalali, P. Woolliams, M. Stewart, P. M. Weaver, M. G. Cain, S. Dunn, and J. Briscoe, "Improved performance of p–n junction-based ZnO nanogenerators through CuSCN-passivation of ZnO nanorods," *J. Mater. Chem. A,* **2014**, 2, 10945-10951.

[19] Z. Zhang, Q. Liao, X. Yan, Z. L. Wang, W. Wang, X. Sun, P. Lin, Y. Huang, and Y. Zhang, "Functional nanogenerators as vibration sensors enhanced by piezotronic effects," *Nano Res.,* **2014**, 7, 190-198.

[20] W. Wu, S. Bai, M. Yuan, Y. Qin, Z. L. Wang, and T. Jing, "Lead zirconate titanate nanowire textile nanogenerator for wearable energy-harvesting and self-powered devices," *ACS Nano,* **2012**, 6, 6231-6235.

[21] C. Xu and Z. L. Wang, "Compact hybrid cell based on a convoluted nanowire structure for harvesting solar and mechanical energy," *Adv. Mater.,* **2011**, 23, 873-877.

[22] D. Choi, K. Y. Lee, M.-J. Jin, S.-G. Ihn, S. Yun, X. Bulliard, W. Choi, S. Y. Lee, S.-W. Kim, and J.-Y. Choi, "Control of naturally coupled piezoelectric and photovoltaic properties for multi-type energy scavengers," *Energy Environ. Sci.,* **2011**, 4, 4607-4613.

[23] S. Xu, Y.-w. Yeh, G. Poirier, M. C. McAlpine, R. A. Register, and N. Yao, "Flexible piezoelectric PMN–PT nanowire-based nanocomposite and device," *Nano Lett.,* **2013**, 13, 2393-2398.

[24] G. Zhu, R. Yang, S. Wang, and Z. L. Wang, "Flexible high-output nanogenerator based on lateral ZnO nanowire array," *Nano Lett.,* **2010**, 10, 3151-3155.

[25] K. Pradel, W. Wu, Y. Ding, and Z. L. Wang, "Solution-derived ZnO homojunction nanowire-films on wearable substrates for energy conversion and self-powered gesture recognition," *Nano Lett.*, **2014**.

[26] N. S. Hudak and G. G. Amatucci, "Small-scale energy harvesting through thermoelectric, vibration, and radiofrequency power conversion," *J. Appl. Phys.*, **2008**, 103, 101301.

[27] M. Hu, K. P. Giapis, J. V. Goicochea, X. Zhang, and D. Poulikakos, "Significant Reduction of Thermal Conductivity in Si/Ge Core− Shell Nanowires," *Nano Lett.*, **2010**, 11, 618-623.

[28] D. M. Rowe, *Modules, Systems, and Applications in Thermoelectrics* vol. 2: CRC Press, **2012**.

[29] P. Hiralal and H. E. Unalan, "Nanowires for energy generation," *Nanotechnology*, **2012**, 23, 194002-194018.

[30] M. S. Dresselhaus, G. Chen, M. Y. Tang, R. Yang, H. Lee, D. Wang, Z. Ren, J. P. Fleurial, and P. Gogna, "New Directions for Low ‐ Dimensional Thermoelectric Materials," *Adv. Mater.*, **2007**, 19, 1043-1053.

[31] Y. Qi, Z. Wang, M. Zhang, F. Yang, and X. Wang, "Thermoelectric devices based on one-dimensional nanostructures," *J. Mater. Chem. A*, **2013**, 1, 6110-6124.

[32] A. I. Hochbaum, R. Chen, R. D. Delgado, W. Liang, E. C. Garnett, M. Najarian, A. Majumdar, and P. Yang, "Enhanced thermoelectric performance of rough silicon nanowires," *Nature*, **2008**, 451, 163-167.

[33] A. I. Boukai, Y. Bunimovich, J. Tahir-Kheli, J.-K. Yu, W. A. Goddard Iii, and J. R. Heath, "Silicon nanowires as efficient thermoelectric materials," *Nature*, **2008**, 451, 168-171.

[34] A. I. Hochbaum and P. Yang, "Semiconductor nanowires for energy conversion," *Chem. Rev.*, **2009**, 110, 527-546.

[35] D. L. Nika, A. I. Cocemasov, D. V. Crismari, and A. A. Balandin, "Thermal conductivity inhibition in phonon engineered core-shell cross-section modulated Si/Ge nanowires," *Appl. Phys. Lett.*, **2013**, 102, 213109.

[36] M. Hu and D. Poulikakos, "Si/Ge superlattice nanowires with ultralow thermal conductivity," *Nano Lett.*, **2012**, 12, 5487-5494.

[37] N. Mingo, "Thermoelectric figure of merit and maximum power factor in III–V semiconductor nanowires," *Appl. Phys. Lett.*, **2004**, 84, 2652-2654.

[38] J. H. Seol, A. L. Moore, S. K. Saha, F. Zhou, L. Shi, Q. L. Ye, R. Scheffler, N. Mingo, and T. Yamada, "Measurement and analysis of thermopower and electrical conductivity of an indium antimonide nanowire from a vapor-liquid-solid method," *J. Appl. Phys.*, **2007**, 101, 023706.

[39] F. Zhou, J. Seol, A. Moore, L. Shi, Q. Ye, and R. Scheffler, "One-dimensional electron transport and thermopower in an individual InSb nanowire," *J. Phys.: Condens. Matter,* **2006**, 18, 9651.

[40] H. D. Park, S. Prokes, M. Twigg, Y. Ding, and Z. L. Wang, "Growth of high quality, epitaxial InSb nanowires," *J. Cryst. Growth,* **2007**, 304, 399-401.

[41] F. Zhou, A. L. Moore, M. T. Pettes, Y. Lee, J. H. Seol, Q. L. Ye, L. Rabenberg, and L. Shi, "Effect of growth base pressure on the thermoelectric properties of indium antimonide nanowires," *J. Phys. D: Appl. Phys.,* **2010**, 43, 025406.

[42] H. H. Huang, I. L. Lu, and Y. R. Wu, "Study of thermoelectric properties of indium nitride nanowire," *Phys. Status Solidi A,* **2011**, 208, 1562-1565.

[43] D. O. Demchenko, P. D. Heinz, and B. Lee, "Determining factors of thermoelectric properties of semiconductor nanowires," *Nanoscale Res. Lett.,* **2011**, 6, 1-6.

[44] Y. Liu, Z. Zhang, X. Wei, Q. Li, and L. M. Peng, "Simultaneous Electrical and Thermoelectric Parameter Retrieval via Two Terminal Current–Voltage Measurements on Individual ZnO Nanowires," *Adv. Funct. Mater.,* **2011**, 21, 3900-3906.

[45] M. Ohtaki, K. Araki, and K. Yamamoto, "High thermoelectric performance of dually doped ZnO ceramics," *J. Electron. Mater.,* **2009**, 38, 1234-1238.

[46] Y. Yang, K. C. Pradel, Q. Jing, J. M. Wu, F. Zhang, Y. Zhou, Y. Zhang, and Z. L. Wang, "Thermoelectric nanogenerators based on single Sb-doped ZnO micro/nanobelts," *ACS Nano*, **2012**, 6, 6984-6989.

[47] Y. Yang, W. Guo, K. C. Pradel, G. Zhu, Y. Zhou, Y. Zhang, Y. Hu, L. Lin, and Z. L. Wang, "Pyroelectric nanogenerators for harvesting thermoelectric energy," *Nano Lett.*, **2012**, 12, 2833-2838.

[48] Y. Yang, H. Zhang, G. Zhu, S. Lee, Z.-H. Lin, and Z. L. Wang, "Flexible hybrid energy cell for simultaneously harvesting thermal, mechanical, and solar energies," *ACS Nano,* **2012**, 7, 785-790.

[49] Y. Yang, Y. Zhou, J. M. Wu, and Z. L. Wang, "Single micro/nanowire pyroelectric nanogenerators as self-powered temperature sensors," *ACS Nano*, **2012**, 6, 8456-8461.

[50] P. Hiralal and H. E. Unalan, "Nanowires for energy generation," *Nanotechnology,* **2012**, 23, 194002-194018.

[51] N. P. Dasgupta and P. Yang, "Semiconductor nanowires for photovoltaic and photoelectrochemical energy conversion," *Front. Phys.*, **2014**, 9, 289-302.

[52] D. Kieven, T. Dittrich, A. Belaidi, J. Tornow, K. Schwarzburg, N. Allsop, and M. Lux-Steiner, "Effect of internal surface area on the performance of ZnO/In2S3/CuSCN solar cells with extremely thin absorber," *Appl. Phys. Lett.*, **2008**, 92, 3107.

[53] M. Krunks, E. Kärber, A. Katerski, K. Otto, I. O. Acik, T. Dedova, and A. Mere, "Extremely thin absorber layer solar cells on zinc oxide nanorods by chemical spray," *Sol. Energy Mater. Sol. Cells*, **2010**, 94, 1191-1195.

[54] J. Rath, Y. Liu, M. De Jong, J. De Wild, J. Schuttauf, M. Brinza, and R. Schropp, "Transparent conducting oxide layers for thin film silicon solar cells," *Thin Solid Films*, **2010**, 518, e129-e135.

[55] K. Q. Peng and S. T. Lee, "Silicon nanowires for photovoltaic solar energy conversion," *Adv. Mater.*, **2011**, 23, 198-215.

[56] R. Franken, R. Stolk, H. Li, C. Van der Werf, J. Rath, and R. Schropp, "Understanding light trapping by light scattering textured back electrodes in thin film n‐i‐p-type silicon solar cells," *J. Appl. Phys.*, **2007**, 102, 014503.

[57] Y. Kuang, K. H. Van der Werf, Z. S. Houweling, and R. E. Schropp, "Nanorod solar cell with an ultrathin a-Si: H absorber layer," *Appl. Phys. Lett.*, **2011**, 98, 113111.

[58] C. M. Hsu, C. Battaglia, C. Pahud, Z. Ruan, F. J. Haug, S. Fan, C. Ballif, and Y. Cui, "High‐Efficiency Amorphous Silicon Solar Cell on a Periodic Nanocone Back Reflector," *Adv. Energy Mater.*, **2012**, 2, 628-633.

[59] S. Geißendörfer, M. Vehse, T. Voss, J.-P. Richters, B. Hanke, K. von Maydell, and C. Agert, "Integration of n-doped ZnO nanorod structures as novel light-trapping concept in amorphous thin film silicon solar cells," *Sol. Energy Mater. Sol. Cells*, **2013**, 111, 153-159.

[60] P. R. Pudasaini, F. Ruiz-Zepeda, M. Sharma, D. Elam, A. Ponce, and A. A. Ayon, "High Efficiency Hybrid Silicon Nanopillar–Polymer Solar Cells," *ACS Appl. Mat. Interfaces*, **2013**, 5, 9620-9627.

[61] G. Jia, B. r. Eisenhawer, J. Dellith, F. Falk, A. Thøgersen, and A. Ulyashin, "Multiple core–shell silicon nanowire-based heterojunction solar cells," *J. Phys. Chem. C*, **2013**, 117, 1091-1096.

[62] S. H. Ko, D. Lee, H. W. Kang, K. H. Nam, J. Y. Yeo, S. J. Hong, C. P. Grigoropoulos, and H. J. Sung, "Nanoforest of hydrothermally grown hierarchical ZnO nanowires for a high efficiency dye-sensitized solar cell," *Nano Lett.*, **2011**, 11, 666-671.

[63] B. M. Kayes, H. A. Atwater, and N. S. Lewis, "Comparison of the device physics principles of planar and radial pn junction nanorod solar cells," *J. Appl. Phys.*, **2005**, 97, 114302.

[64] L. Hu and G. Chen, "Analysis of optical absorption in silicon nanowire arrays for photovoltaic applications," *Nano Lett.,* **2007**, 7, 3249-3252.

[65] B. Tian, X. Zheng, T. J. Kempa, Y. Fang, N. Yu, G. Yu, J. Huang, and C. M. Lieber, "Coaxial silicon nanowires as solar cells and nanoelectronic power sources," *Nature,* **2007**, 449, 885-889.

[66] M. Adachi, M. Anantram, and K. Karim, "Core-shell silicon nanowire solar cells," *Sci. Rep.*, **2013**, 3.

[67] Y. Kuang, M. Di Vece, J. K. Rath, L. van Dijk, and R. E. Schropp, "Elongated nanostructures for radial junction solar cells," *Rep. Prog. Phys.*, **2013**, 76, 106502.

[68] B. Pradhan, S. K. Batabyal, and A. J. Pal, "Rectifying junction in a single ZnO vertical nanowire," *Appl. Phys. Lett.*, **2006**, 89, 233109.

[69] P. Krogstrup, H. I. Jørgensen, M. Heiss, O. Demichel, J. V. Holm, M. Aagesen, J. Nygard, and A. F. i Morral, "Single-nanowire solar cells beyond the Shockley-Queisser limit," *Nat. Photonics*, **2013**, 7, 306-310.

[70] K. Seo, M. Wober, P. Steinvurzel, E. Schonbrun, Y. Dan, T. Ellenbogen, and K. B. Crozier, "Multicolored vertical silicon nanowires," *Nano Lett.*, **2011**, 11, 1851-1856.

[71] L. K. van Vugt, B. Zhang, B. Piccione, A. A. Spector, and R. Agarwal, "Size-dependent waveguide dispersion in nanowire optical cavities: slowed light and dispersionless guiding," *Nano Lett.*, **2009**, 9, 1684-1688.

[72] G. Brönstrup, C. Leiterer, N. Jahr, C. Gutsche, A. Lysov, I. Regolin, W. Prost, F. Tegude, W. Fritzsche, and S. Christiansen, "A precise optical determination of nanoscale diameters of semiconductor nanowires," *Nanotechnology*, **2011**, 22, 385201.

[73] L. Cao, J. S. White, J.-S. Park, J. A. Schuller, B. M. Clemens, and M. L. Brongersma, "Engineering light absorption in semiconductor nanowire devices," *Nat. Mater.*, **2009**, 8, 643-647.

[74] M. Heiss and A. F. i Morral, "Fundamental limits in the external quantum efficiency of single nanowire solar cells," *Appl. Phys. Lett.*, **2011**, 99, 263102.

[75] R. LaPierre, "Theoretical conversion efficiency of a two-junction III-V nanowire on Si solar cell," *J. Appl. Phys.*, **2011**, 110, 014310.

[76] M. Bosi and C. Pelosi, "The potential of III-V semiconductors as terrestrial photovoltaic devices," *Prog. Photovoltaics Res. Appl.*, **2007**, 15, 51-68.

[77] Y. Dong, B. Tian, T. J. Kempa, and C. M. Lieber, "Coaxial group III− nitride nanowire photovoltaics," *Nano Lett.*, **2009**, 9, 2183-2187.

[78] M. A. Green, K. Emery, Y. Hishikawa, W. Warta, and E. D. Dunlop, "Solar cell efficiency tables (Version 45)," *Prog. Photovoltaics Res. Appl.,* **2015**, 23, 1-9.

[79] J. Y. Lek, G. Xing, T. C. Sum, and Y. M. Lam, "Electron transport limitation in P3HT: CdSe nanorods hybrid solar cells," *ACS Appl. Mat. Interfaces,* **2014**, 6, 894-902.

[80] C. Pan, S. Niu, Y. Ding, L. Dong, R. Yu, Y. Liu, G. Zhu, and Z. L. Wang, "Enhanced Cu2S/CdS coaxial nanowire solar cells by piezo-phototronic effect," *Nano Lett.,* **2012**, 12, 3302-3307.

[81] B. Weintraub, Y. Wei, and Z. L. Wang, "Optical Fiber/Nanowire Hybrid Structures for Efficient Three‐Dimensional Dye‐Sensitized Solar Cells," *Angew. Chem.,* **2009**, 121, 9143-9147.

[82] M. Naughton, K. Kempa, Z. Ren, Y. Gao, J. Rybczynski, N. Argenti, W. Gao, Y. Wang, Y. Peng, and J. Naughton, "Efficient nanocoax‐based solar cells," *Phys. Status Solidi RRL,* **2010**, 4, 181-183.

[83] J. Wallentin, N. Anttu, D. Asoli, M. Huffman, I. Åberg, M. H. Magnusson, G. Siefer, P. Fuss-Kailuweit, F. Dimroth, and B. Witzigmann, "InP nanowire array solar cells achieving 13.8% efficiency by exceeding the ray optics limit," *Science,* **2013**, 339, 1057-1060.

[84] H. P. T. Nguyen, Y.-L. Chang, I. Shih, and Z. Mi, "InN pin nanowire solar cells on Si," *IEEE J. Sel. Top. Quantum Electron.,* **2011**, 17, 1062-1069.

[85] V. Sharma, U. Mukherji, V. Joseph, and S. Gupta, "Optimal energy management policies for energy harvesting sensor nodes," *IEEE Trans. Wireless Commun.,* **2010**, 9, 1326-1336.

[86] B. H. Calhoun, D. C. Daly, N. Verma, D. F. Finchelstein, D. D. Wentzloff, A. Wang, S.-H. Cho, and A. P. Chandrakasan, "Design considerations for ultra-low energy wireless microsensor nodes," *IEEE Trans. Comput.,* **2005**, 54, 727-740.

[87] Z. Qian, O. Abdel-Rahman, and I. Batarseh, "An integrated four-port DC/DC converter for renewable energy applications," *IEEE Trans. Power Electron.,* **2010**, 25, 1877-1887.

[88] A. Richelli, L. Colalongo, S. Tonoli, and Z. M. Kovacs-Vajna, "A 0.2 V DC/DC boost converter for power harvesting applications," *IEEE Trans. Power Electron.,* **2009**, 24, 1541-1546.

[89] Z. L. Wang and W. Wu, "Nanotechnology‐Enabled Energy Harvesting for Self‐Powered Micro‐/Nanosystems," *Angew. Chem. Int. Ed.,* **2012**, 51, 11700-11721.

[90] Y. Qi and M. C. McAlpine, "Nanotechnology-enabled flexible and biocompatible energy harvesting," *Energy Environ. Sci.,* **2010**, 3, 1275-1285.

[91] Z. L. Wang, "Toward self-powered sensor networks," *Nano Today,* **2010**.

[92] J. Lueke and W. A. Moussa, "MEMS-Based power generation techniques for implantable biosensing applications," *Sensors*, **2011**, 11, 1433-1460.

[93] Y.-Z. Long, M. Yu, B. Sun, C.-Z. Gu, and Z. Fan, "Recent advances in large-scale assembly of semiconducting inorganic nanowires and nanofibers for electronics, sensors and photovoltaics," *Chem. Soc. Rev.*, **2012**, 41, 4560-4580.

[94] X. Wang, "Piezoelectric nanogenerators–harvesting ambient mechanical energy at the nanometer scale," *Nano Energy*, **2011**.

[95] P. Hiralal and H. E. Unalan, "Nanowires for energy generation," *Nanotechnology*, **2012**, 23, 194002-194018.

[96] H. D. Espinosa, R. A. Bernal, and M. Minary‐Jolandan, "A review of mechanical and electromechanical properties of piezoelectric nanowires," *Adv. Mater.*, **2012**, 24, 4656-4675.

[97] X. Wang, J. Song, J. Liu, and Z. L. Wang, "Direct-current nanogenerator driven by ultrasonic waves," *Science*, **2007**, 316, 102-105.

[98] Y. Hu, Y. Zhang, C. Xu, L. Lin, R. L. Snyder, and Z. L. Wang, "Self-powered system with wireless data transmission," *Nano Lett.*, **2011**, 11, 2572-2577.

[99] C. Chang, V. H. Tran, J. Wang, Y.-K. Fuh, and L. Lin, "Direct-write piezoelectric polymeric nanogenerator with high energy conversion efficiency," *Nano Lett.*, **2010**, 10, 726-731.

[100] K.-I. Park, S. Xu, Y. Liu, G.-T. Hwang, S.-J. L. Kang, Z. L. Wang, and K. J. Lee, "Piezoelectric BaTiO3 thin film nanogenerator on plastic substrates," *Nano Lett.*, **2010**, 10, 4939-4943.

[101] X. Chen, S. Xu, N. Yao, and Y. Shi, "1.6 V nanogenerator for mechanical energy harvesting using PZT nanofibers," *Nano Lett.*, **2010**, 10, 2133-2137.

[102] Y. Gao and Z. L. Wang, "Electrostatic potential in a bent piezoelectric nanowire. The fundamental theory of nanogenerator and nanopiezotronics," *Nano Lett.*, **2007**, 7, 2499-2505.

[103] Y. Gao and Z. L. Wang, "Equilibrium potential of free charge carriers in a bent piezoelectric semiconductive nanowire," *Nano Lett.*, **2009**, 9, 1103-1110.

[104] G. Romano, G. Mantini, A. Di Carlo, A. D'Amico, C. Falconi, and Z. L. Wang, "Piezoelectric potential in vertically aligned nanowires for high output nanogenerators," *Nanotechnology*, **2011**, 22, 465401.

[105] R. Araneo, G. Lovat, P. Burghignoli, and C. Falconi, "Piezo‐Semiconductive Quasi‐1D Nanodevices with or without Anti‐Symmetry," *Adv. Mater.*, **2012**, 24, 4719-4724.

[106] X. Wang, J. Song, F. Zhang, C. He, Z. Hu, and Z. Wang, "Electricity Generation based on One‐Dimensional Group‐III Nitride Nanomaterials," *Adv. Mater.*, **2010**, 22, 2155-2158.

[107] C.-T. Huang, J. Song, W.-F. Lee, Y. Ding, Z. Gao, Y. Hao, L.-J. Chen, and Z. L. Wang, "GaN nanowire arrays for high-output nanogenerators," *J. Am. Chem. Soc.*, **2010**, 132, 4766-4771.

[108] C. T. Huang, J. Song, C. M. Tsai, W. F. Lee, D. H. Lien, Z. Gao, Y. Hao, L. J. Chen, and Z. L. Wang, "Single‐InN‐Nanowire Nanogenerator with Upto 1 V Output Voltage," *Adv. Mater.*, **2010**, 22, 4008-4013.

[109] N. J. Ku, C. H. Wang, J. H. Huang, H. C. Fang, P. C. Huang, and C. P. Liu, "Energy Harvesting from the Obliquely Aligned InN Nanowire Array with a Surface Electron‐Accumulation Layer," *Adv. Mater.*, **2013**, 25, 861-866.

[110] B. Kumar and S.-W. Kim, "Recent advances in power generation through piezoelectric nanogenerators," *J. Mater. Chem.*, **2011**, 21, 18946-18958.

[111] Z. L. Wang, "Toward self-powered sensor networks," *Nano Today*, **2010**, 5, 512-514.

[112] Y. Qiu, H. Zhang, L. Hu, D. Yang, L. Wang, B. Wang, J. Ji, G. Liu, X. Liu, and J. Lin, "Flexible piezoelectric nanogenerators based on ZnO nanorods grown on common paper substrates," *Nanoscale*, **2012**, 4, 6568-6573.

[113] T. I. Lee, S. Lee, E. Lee, S. Sohn, Y. Lee, S. Lee, G. Moon, D. Kim, Y. S. Kim, and J. M. Myoung, "High‐Power Density Piezoelectric Energy Harvesting Using Radially Strained Ultrathin Trigonal Tellurium Nanowire Assembly," *Adv. Mater.*, **2013**, 25, 2920-2925.

[114] Z. L. Wang, "Progress in piezotronics and piezo‐phototronics," *Adv. Mater.*, **2012**, 24, 4632-4646.

[115] X. Wang, J. Song, F. Zhang, C. He, Z. Hu, and Z. Wang, "Electricity Generation based on One‐Dimensional Group‐III Nitride Nanomaterials," *Adv. Mater.*, **2010**, 22, 2155-2158.

[116] A. G. Bhuiyan, A. Hashimoto, and A. Yamamoto, "Indium nitride (InN): A review on growth, characterization, and properties," *J. Appl. Phys.*, **2003**, 94, 2779-2808.

[117] T. Matsuoka, H. Okamoto, M. Nakao, H. Harima, and E. Kurimoto, "Optical bandgap energy of wurtzite InN," *Appl. Phys. Lett.*, **2002**, 81, 1246-1248.

[118] J. Wu, W. Walukiewicz, K. Yu, J. Ager Iii, E. Haller, H. Lu, W. J. Schaff, Y. Saito, and Y. Nanishi, "Unusual properties of the fundamental band gap of InN," *Appl. Phys. Lett.*, **2002**, 80, 3967-3969.

[119] J. Wu, W. Walukiewicz, W. Shan, K. Yu, J. Ager III, E. Haller, H. Lu, and W. J. Schaff, "Effects of the narrow band gap on the properties of InN," *Phys. Rev. B*, **2002**, 66, 201403.

[120] Y.-L. Chang, F. Li, A. Fatehi, and Z. Mi, "Molecular beam epitaxial growth and characterization of non-tapered InN nanowires on Si (111)," *Nanotechnology*, **2009**, 20, 345203.

[121] Y. L. Chang, Z. Mi, and F. Li, "Photoluminescence properties of a nearly intrinsic single InN nanowire," *Adv. Funct. Mater.,* **2010**, 20, 4146-4151.

[122] S. Zhao, Q. Wang, Z. Mi, S. Fathololoumi, T. Gonzalez, and M. Andrews, "Observation of phonon sideband emission in intrinsic InN nanowires: a photoluminescence and micro-Raman scattering study," *Nanotechnology,* **2012**, 23, 415706.

[123] S. Zhao, Z. Mi, M. Kibria, Q. Li, and G. Wang, "Understanding the role of Si doping on surface charge and optical properties: Photoluminescence study of intrinsic and Si-doped InN nanowires," *Phys. Rev. B,* **2012**, 85, 245313.

[124] S. Zhao, S. Fathololoumi, K. Bevan, D. Liu, M. Kibria, Q. Li, G. Wang, H. Guo, and Z. Mi, "Tuning the surface charge properties of epitaxial InN nanowires," *Nano Lett.,* **2012**, 12, 2877-2882.

[125] M. Holtz, I. Gherasoiu, V. Kuryatkov, S. Nikishin, A. Bernussi, and M. Holtz, "Influence of phonons on the temperature dependence of photoluminescence in InN with low carrier concentration," *J. Appl. Phys.,* **2009**, 105, 3702.

[126] V. Polyakov, F. Schwierz, F. Fuchs, J. Furthmüller, and F. Bechstedt, "Low-field and high-field electron transport in zinc blende InN," *Appl. Phys. Lett.,* **2009**, 94, 022102.

[127] F. Glas, "Critical dimensions for the plastic relaxation of strained axial heterostructures in free-standing nanowires," *Phys. Rev. B,* **2006**, 74, 121302.

[128] H. Xiang, S.-H. Wei, J. L. Da Silva, and J. Li, "Strain relaxation and band-gap tunability in ternary In x Ga 1− x N nanowires," *Phys. Rev. B,* **2008**, 78, 193301.

[129] M. Knelangen, V. Consonni, A. Trampert, and H. Riechert, "In situ analysis of strain relaxation during catalyst-free nucleation and growth of GaN nanowires," *Nanotechnology,* **2010**, 21, 245705.

[130] S. Zhao, B. Le, D. Liu, X. Liu, M. Kibria, T. Szkopek, H. Guo, and Z. Mi, "p-Type InN nanowires," *Nano Lett.,* **2013**, 13, 5509-5513.

[131] G. Zhu, A. C. Wang, Y. Liu, Y. Zhou, and Z. L. Wang, "Functional electrical stimulation by nanogenerator with 58 V output voltage," *Nano Lett.,* **2012**, 12, 3086-3090.

[132] Z. L. Wang, "Energy Harvesting Using Piezoelectric Nanowires–A Correspondence on “Energy Harvesting Using Nanowires?” by Alexe et al," *Adv. Mater.,* **2009**, 21, 1311-1315.

[133] C. H. Wang, W. S. Liao, N. J. Ku, Y. C. Li, Y. C. Chen, L. W. Tu, and C. P. Liu, "Effects of Free Carriers on Piezoelectric Nanogenerators and Piezotronic Devices Made of GaN Nanowire Arrays," *Small,* **2014**, 10, 4718-4725.

[134] C. H. Wang, W. S. Liao, Z. H. Lin, N. J. Ku, Y. C. Li, Y. C. Chen, Z. L. Wang, and C. P. Liu, "Optimization of the Output Efficiency of GaN Nanowire Piezoelectric Nanogenerators by Tuning the Free Carrier Concentration," *Adv. Energy Mater.,* **2014**, 4.

[135] J. Liu, P. Fei, J. Zhou, R. Tummala, and Z. L. Wang, "Toward high output-power nanogenerator," *Appl. Phys. Lett.,* **2008**, 92, 173105.

[136] B. Simpkins, M. Mastro, C. Eddy Jr, and P. Pehrsson, "Surface depletion effects in semiconducting nanowires," *J. Appl. Phys.,* **2008**, 103, 104313.

[137] S. Lee, R. Hinchet, Y. Lee, Y. Yang, Z. H. Lin, G. Ardila, L. Montès, M. Mouis, and Z. L. Wang, "Ultrathin Nanogenerators as Self‐Powered/Active Skin Sensors for Tracking Eye Ball Motion," *Adv. Funct. Mater.,* **2014**, 24, 1163-1168.

[138] D. K. Schroder, *Semiconductor material and device characterization*: John Wiley & Sons, **2006**.

[139] R. Hinchet, S. Lee, G. Ardila, L. Montès, M. Mouis, and Z. L. Wang, "Performance Optimization of Vertical Nanowire‐based Piezoelectric Nanogenerators," *Adv. Funct. Mater.,* **2014**, 24, 971-977.

[140] L. Lin, Q. Jing, Y. Zhang, Y. Hu, S. Wang, Y. Bando, R. P. Han, and Z. L. Wang, "An elastic-spring-substrated nanogenerator as an active sensor for self-powered balance," *Energy Environ. Sci.,* **2013**, 6, 1164-1169.

[141] G. Liu, E. Abdel-Rahman, and D. Ban, "Performance optimization of p-n homojunction nanowire-based piezoelectric nanogenerators through control of doping concentration," *J. Appl. Phys.,* **2015**, 118, 094307.

[142] N.-J. Ku, J.-H. Huang, C.-H. Wang, H.-C. Fang, and C.-P. Liu, "Crystal face-dependent nanopiezotronics of an obliquely aligned InN nanorod array," *Nano Lett.,* **2012**, 12, 562-568.

[143] E. Halpern, G. Elias, A. Kretinin, H. Shtrikman, and Y. Rosenwaks, "Direct measurement of surface states density and energy distribution in individual InAs nanowires," *Appl. Phys. Lett.,* **2012**, 100, 262105.

[144] S. Xu, Y. Qin, C. Xu, Y. Wei, R. Yang, and Z. L. Wang, "Self-powered nanowire devices," *Nat. Nanotechnol.,* **2010**, 5, 366-373.

[145] Z. L. Wang and J. Song, "Piezoelectric nanogenerators based on zinc oxide nanowire arrays," *Science,* **2006**, 312, 242-246.

[146] Y. Hu, J. Yang, S. Niu, W. Wu, and Z. L. Wang, "Hybridizing Triboelectrification and Electromagnetic Induction Effects for High-Efficient Mechanical Energy Harvesting," *ACS Nano,* **2014**, 8, 7442-7450.

[147] K. C. Pradel, W. Wu, Y. Zhou, X. Wen, Y. Ding, and Z. L. Wang, "Piezotronic effect in solution-grown p-type ZnO nanowires and films," *Nano Lett.*, **2013**, 13, 2647-2653.

[148] H. Kim, S. M. Kim, H. Son, H. Kim, B. Park, J. Ku, J. I. Sohn, K. Im, J. E. Jang, and J.-J. Park, "Enhancement of piezoelectricity via electrostatic effects on a textile platform," *Energy Environ. Sci.*, **2012**, 5, 8932-8936.

[149] S. Y. Chung, S. Kim, J. H. Lee, K. Kim, S. W. Kim, C. Y. Kang, S. J. Yoon, and Y. S. Kim, "All ‐ solution ‐ processed flexible thin film piezoelectric nanogenerator," *Adv. Mater.*, **2012**, 24, 6022-6027.

[150] S.-H. Shin, M. H. Lee, J.-Y. Jung, J. H. Seol, and J. Nah, "Piezoelectric performance enhancement of ZnO flexible nanogenerator by a CuO–ZnO p–n junction formation," *J. Mater. Chem. C*, **2013**, 1, 8103-8107.

[151] G. Wang, S. Chu, N. Zhan, Y. Lin, L. Chernyak, and J. Liu, "ZnO homojunction photodiodes based on Sb-doped p-type nanowire array and n-type film for ultraviolet detection," *Appl. Phys. Lett.*, **2011**, 98, 041107.

[152] Y. H. Leung, Z. He, L. Luo, C. Tsang, N. Wong, W. Zhang, and S. Lee, "ZnO nanowires array pn homojunction and its application as a visible-blind ultraviolet photodetector," *Appl. Phys. Lett.*, **2010**, 96, 053102-053102-3.

[153] Y. Sun, N. A. Fox, G. M. Fuge, and M. N. Ashfold, "Toward a single ZnO nanowire homojunction," *J. Phys. Chem. C*, **2010**, 114, 21338-21341.

[154] M. Chen, M. Lu, Y. Wu, J. Song, C. Lee, M. Lu, Y. Chang, L. Chou, Z. Wang, and L. Chen, "Near UV LEDs made with in situ doped pn homojunction ZnO nanowire arrays," *Nano Lett.*, **2010**, 10, 4387-4393.

[155] X. W. Sun, B. Ling, J. L. Zhao, S. T. Tan, Y. Yang, Y. Shen, Z. L. Dong, and X. Li, "Ultraviolet emission from a ZnO rod homojunction light-emitting diode," *Appl. Phys. Lett.*, **2009**, 95, 133124-133124-3.

[156] T. Chung, L. Luo, Z. He, Y. Leung, I. Shafiq, Z. Yao, and S. Lee, "Selective growth of catalyst-free ZnO nanowire arrays on Al: ZnO for device application," *Appl. Phys. Lett.*, **2007**, 91, 233112.

[157] G. Li, A. Sundararajan, A. Mouti, Y.-J. Chang, A. R. Lupini, S. J. Pennycook, D. R. Strachan, and B. S. Guiton, "Synthesis and characterization of p–n homojunction-containing zinc oxide nanowires," *Nanoscale*, **2013**, 5, 2259-2263.

[158] H. D. Cho, A. S. Zakirov, S. U. Yuldashev, C. W. Ahn, Y. K. Yeo, and T. W. Kang, "Photovoltaic device on a single ZnO nanowire p–n homojunction," *Nanotechnology*, **2012**, 23, 115401.

[159] Y. H. Ko, S. H. Lee, and J. S. Yu, "Performance enhanced piezoelectric ZnO nanogenerators with highly rough Au electrode surfaces on ZnO submicrorod arrays," *Appl. Phys. Lett.*, **2013**, 103, 022911.

[160] R. E. Nowak, M. Vehse, O. Sergeev, T. Voss, M. Seyfried, K. von Maydell, and C. Agert, "ZnO Nanorods with Broadband Antireflective Properties for Improved Light Management in Silicon Thin‐Film Solar Cells," *Adv. Opt. Mater.*, **2014**, 2, 94-99.

[161] C. Xu and D. Gao, "Two-stage hydrothermal growth of long ZnO nanowires for efficient TiO2 nanotube-based dye-sensitized solar cells," *J. Phys. Chem. C*, **2012**, 116, 7236-7241.

[162] A. Djurišić, Y. Leung, K. Tam, Y. Hsu, L. Ding, W. Ge, Y. Zhong, K. Wong, W. Chan, and H. Tam, "Defect emissions in ZnO nanostructures," *Nanotechnology*, **2007**, 18, 095702.

[163] C. Rauch, W. Gehlhoff, M. Wagner, E. Malguth, G. Callsen, R. Kirste, B. Salameh, A. Hoffmann, S. Polarz, and Y. Aksu, "Lithium related deep and shallow acceptors in Li-doped ZnO nanocrystals," *J. Appl. Phys.*, **2010**, 107, 024311.

[164] M. McCluskey and S. Jokela, "Defects in ZnO," *J. Appl. Phys.*, **2009**, 106, 071101.

[165] J. I. Sohn, S. N. Cha, B. G. Song, S. Lee, S. M. Kim, J. Ku, H. J. Kim, Y. J. Park, B. L. Choi, and Z. L. Wang, "Engineering of efficiency limiting free carriers and an interfacial energy barrier for an enhancing piezoelectric generation," *Energy Environ. Sci.*, **2013**, 6, 97-104.

[166] S.-H. Shin, Y.-H. Kim, M. H. Lee, J.-Y. Jung, J. H. Seol, and J. Nah, "Lithium-Doped Zinc Oxide Nanowires–Polymer Composite for High Performance Flexible Piezoelectric Nanogenerator," *ACS Nano*, **2014**, 8, 10844-10850.

[167] M. Wardle, J. Goss, and P. Briddon, "Theory of Li in ZnO: A limitation for Li-based p-type doping," *Phys. Rev. B*, **2005**, 71, 155205.

[168] P.-E. Mazeran, M. Beyaoui, M. Bigerelle, and M. Guigon, "Determination of mechanical properties by nanoindentation in the case of viscous materials," *Int. J. Mater. Res.*, **2012**, 103, 715-722.

[169] F. Wang, J.-H. Seo, D. Bayerl, J. Shi, H. Mi, Z. Ma, D. Zhao, Y. Shuai, W. Zhou, and X. Wang, "An aqueous solution-based doping strategy for large-scale synthesis of Sb-doped ZnO nanowires," *Nanotechnology*, **2011**, 22, 225602.

[170] M. Law, L. E. Greene, J. C. Johnson, R. Saykally, and P. Yang, "Nanowire dye-sensitized solar cells," *Nat. Mater.*, **2005**, 4, 455-459.

[171] J. Jean, S. Chang, P. R. Brown, J. J. Cheng, P. H. Rekemeyer, M. G. Bawendi, S. Gradečak, and V. Bulović, "ZnO nanowire arrays for enhanced photocurrent in PbS quantum dot solar cells," *Adv. Mater.*, **2013**, 25, 2790-2796.

[172] W. U. Huynh, J. J. Dittmer, and A. P. Alivisatos, "Hybrid nanorod-polymer solar cells," *Science*, **2002**, 295, 2425-2427.

[173] L. Li, S. Chen, X. Wang, Y. Bando, and D. Golberg, "Nanostructured solar cells harvesting multi-type energies," *Energy Environ. Sci.*, **2012**, 5, 6040-6046.

[174] S. Xu, B. J. Hansen, and Z. L. Wang, "Piezoelectric-nanowire-enabled power source for driving wireless microelectronics," *Nat. Commun.*, **2010**, 1, 93.

[175] Y. Hu, Y. Zhang, C. Xu, L. Lin, R. L. Snyder, and Z. L. Wang, "Self-powered system with wireless data transmission," *Nano Lett.*, **2011**, 11, 2572-2577.

[176] J. Chen, G. Zhu, J. Yang, Q. Jing, P. Bai, W. Yang, X. Qi, Y. Su, and Z. L. Wang, "Personalized Keystroke Dynamics for Self-Powered Human–Machine Interfacing," *ACS Nano*, **2015**, 9, 105-116.

[177] Z. L. Wang, "Self‐Powered Nanosensors and Nanosystems," *Adv. Mater.*, **2012**, 24, 280-285.

[178] C. Xu, X. Wang, and Z. L. Wang, "Nanowire structured hybrid cell for concurrently scavenging solar and mechanical energies," *J. Am. Chem. Soc.*, **2009**, 131, 5866-5872.

[179] C. Pan, W. Guo, L. Dong, G. Zhu, and Z. L. Wang, "Optical Fiber‐Based Core‐Shell Coaxially Structured Hybrid Cells for Self‐Powered Nanosystems," *Adv. Mater.*, **2012**, 24, 3356-3361.

[180] Y. Zi, L. Lin, J. Wang, S. Wang, J. Chen, X. Fan, P. K. Yang, F. Yi, and Z. L. Wang, "Triboelectric‐Pyroelectric‐Piezoelectric Hybrid Cell for High‐Efficiency Energy‐Harvesting and Self‐Powered Sensing," *Adv. Mater.*, **2015**, 27, 2340-2347.

[181] J. H. Lee, K. Y. Lee, M. K. Gupta, T. Y. Kim, D. Y. Lee, J. Oh, C. Ryu, W. J. Yoo, C. Y. Kang, and S. J. Yoon, "Highly Stretchable Piezoelectric‐Pyroelectric Hybrid Nanogenerator," *Adv. Mater.*, **2014**, 26, 765-769.

[182] L. Zheng, G. Cheng, J. Chen, L. Lin, J. Wang, Y. Liu, H. Li, and Z. L. Wang, "A Hybridized Power Panel to Simultaneously Generate Electricity from Sunlight, Raindrops, and Wind around the Clock," *Adv. Energy Mater.*, **2015**.

[183] Y. Yang, H. Zhang, J. Chen, S. Lee, T.-C. Hou, and Z. L. Wang, "Simultaneously harvesting mechanical and chemical energies by a hybrid cell for self-powered biosensors and personal electronics," *Energy Environ. Sci.*, **2013**, 6, 1744-1749.

[184] Y. Yang, H. Zhang, Y. Liu, Z.-H. Lin, S. Lee, Z. Lin, C. P. Wong, and Z. L. Wang, "Silicon-based hybrid energy cell for self-powered electrodegradation and personal electronics," *ACS Nano*, **2013**, 7, 2808-2813.

[185] Y. Yang, H. Zhang, S. Lee, D. Kim, W. Hwang, and Z. L. Wang, "Hybrid energy cell for degradation of methyl orange by self-powered electrocatalytic oxidation," *Nano Lett.*, **2013**, 13, 803-808.

[186] G. Cheng, Z.-H. Lin, Z.-l. Du, and Z. L. Wang, "Simultaneously harvesting electrostatic and mechanical energies from flowing water by a hybridized triboelectric nanogenerator," *ACS Nano,* **2014**, 8, 1932-1939.

[187] X. Wang, S. Wang, Y. Yang, and Z. L. Wang, "Hybridized Electromagnetic–Triboelectric Nanogenerator for Scavenging Air-Flow Energy to Sustainably Power Temperature Sensors," *ACS Nano,* **2015**, 9, 4553-4562.

[188] Y. Yang, H. Zhang, Z.-H. Lin, Y. Liu, J. Chen, Z. Lin, Y. S. Zhou, C. P. Wong, and Z. L. Wang, "A hybrid energy cell for self-powered water splitting," *Energy Environ. Sci.*, **2013**, 6, 2429-2434.

[189] B. J. Hansen, Y. Liu, R. Yang, and Z. L. Wang, "Hybrid nanogenerator for concurrently harvesting biomechanical and biochemical energy," *ACS Nano,* **2010**, 4, 3647-3652.

[190] R. Yang, Y. Qin, C. Li, G. Zhu, and Z. L. Wang, "Converting biomechanical energy into electricity by a muscle-movement-driven nanogenerator," *Nano Lett.*, **2009**, 9, 1201-1205.

[191] Z. Wang, R. Yu, X. Wen, Y. Liu, C. Pan, W. Wu, and Z. L. Wang, "Optimizing Performance of Silicon-Based p–n Junction Photodetectors by the Piezo-Phototronic Effect," *ACS Nano,* **2014**, 8, 12866-12873.

[192] J. C. Shin, P. K. Mohseni, K. J. Yu, S. Tomasulo, K. H. Montgomery, M. L. Lee, J. A. Rogers, and X. Li, "Heterogeneous integration of InGaAs nanowires on the rear surface of Si solar cells for efficiency enhancement," *ACS Nano,* **2012**, 6, 11074-11079.

[193] L. E. Greene, M. Law, J. Goldberger, F. Kim, J. C. Johnson, Y. Zhang, R. J. Saykally, and P. Yang, "Low‐temperature wafer‐scale production of ZnO nanowire arrays," *Angew. Chem. Int. Ed.*, **2003**, 42, 3031-3034.